



HAL
open science

HTS dipole insert using a twisted stacked cable for a particle accelerator- Twisted Stacked/ Block-type HTS insert -

John Himbele

► **To cite this version:**

John Himbele. HTS dipole insert using a twisted stacked cable for a particle accelerator- Twisted Stacked/ Block-type HTS insert -. Electric power. Université Grenoble Alpes, 2016. English. NNT : 2016GREAT108 . tel-01593471

HAL Id: tel-01593471

<https://theses.hal.science/tel-01593471>

Submitted on 26 Sep 2017

HAL is a multi-disciplinary open access archive for the deposit and dissemination of scientific research documents, whether they are published or not. The documents may come from teaching and research institutions in France or abroad, or from public or private research centers.

L'archive ouverte pluridisciplinaire **HAL**, est destinée au dépôt et à la diffusion de documents scientifiques de niveau recherche, publiés ou non, émanant des établissements d'enseignement et de recherche français ou étrangers, des laboratoires publics ou privés.

THÈSE

Pour obtenir le grade de

DOCTEUR DE LA COMMUNAUTE UNIVERSITE GRENOBLE ALPES

Spécialité : **Génie électrique**

Arrêté ministériel : 7 août 2006

Présentée par

John J. HIMBELE

Thèse dirigée par **Pascal TIXADOR** et
codirigée par **Arnaud BADEL**

préparée au sein du **G2ELab, INP Grenoble**
dans l'**École Doctorale EEATS**

Contribution à l'étude d'un insert dipolaire supraconducteur à haute température critique pour accéléra- teur de particules, utilisant le con- cept de câble multi-rabans torsadé

Thèse soutenue publiquement le **8 décembre 2016**,
devant le jury composé de:

Didier TRICHET

Professeur (Université de Nantes), Président

Jean-Luc DUCHATEAU

Directeur de recherche (CEA), Rapporteur

Pierre VÉDRINE

Directeur de recherche (CEA), Examineur

Carmine SENATORE

Professeur (Université de Genève), Examineur

Luca BOTTURA

Chef de groupe (CERN), Examineur

Gérard MEUNIER

Directeur de recherche (INP Grenoble), Examineur

Arnaud BADEL

Chargé de recherche (CNRS), Examineur

Pascal TIXADOR

Professeur (INP Grenoble), Examineur



Table of contents

| | |
|--|----|
| Preface..... | 4 |
| Chapter 1. Introduction: Superconducting particle accelerator for the quest of the fundamental structure of the universe | |
| 1.1. Particle accelerator | 5 |
| 1.1.1 Purpose and aim..... | 5 |
| 1.1.2 Magnetic system..... | 6 |
| 1.2. Superconductor for accelerator magnet..... | 8 |
| 1.2.1. Superconducting phenomenon..... | 8 |
| 1.2.2. Critical characteristic..... | 9 |
| 1.2.3. Magnetization..... | 10 |
| 1.2.4. Quench..... | 12 |
| 1.2.5. Current densities..... | 13 |
| 1.2.6. Mechanics..... | 14 |
| 1.2.7. Field quality..... | 15 |
| 1.2.8. Cost..... | 15 |
| 1.2.9. Conclusion: Superconducting requirement for accelerator magnet... | 16 |
| 1.3. Superconducting material for accelerator magnet..... | 17 |
| 1.3.1. Low T_c superconductors..... | 18 |
| 1.3.1.1. NbTi..... | 18 |
| 1.3.1.2. Nb ₃ Sn..... | 19 |
| 1.3.2. High T_c superconductors..... | 20 |
| 1.3.2.1. Bi (2212/2223) | 20 |
| 1.3.2.2. ReBCO..... | 21 |
| 1.4. ReBCO cable for accelerator magnet..... | 23 |
| 1.4.1. Roebel cable | 23 |
| 1.4.2. CORC cable | 24 |
| 1.4.3. Stacked cable | 24 |
| 1.5. Conclusion of study: twisted stacked YBCO cable insert..... | 27 |
| Chapter 2. Electromagnetic design of twisted stacked/ block-type HTS insert | |
| 2.1. 2D HTS insert | 28 |
| 2.1.1. Optimization tool | 28 |
| 2.1.2. Dimensional and physical constraints for twisted stacked cable | 36 |

| | | |
|----------|--|----|
| 2.1.3. | Magnet cross-section at straight part | 40 |
| 2.2. | 3D magnet ends..... | 44 |
| 2.2.1. | Structure of twisted stacked cable | 44 |
| 2.2.2. | Winding strategy | 45 |
| 2.2.2.1. | Racetrack flat coil | 45 |
| 2.2.2.2. | Flared-end coil..... | 46 |
| 2.2.2.3. | Layer jump | 49 |
| 2.2.3. | Magnet end architecture | 51 |
| 2.2.3.1. | Racetrack to racetrack double pancake coil (1 st DP) | 53 |
| 2.2.3.2. | Racetrack to flared-end double pancake coil (2 nd DP) | 54 |
| 2.2.3.3. | Flared-end to flared-end double pancake coil (3 rd DP)..... | 56 |
| 2.2.3.4. | Short summary..... | 57 |
| 2.2.4. | Electromagnetic property of magnet ends..... | 58 |
| 2.3. | Operational margins of HTS insert | 61 |
| 2.3.1. | Relative magnet ends position of HTS insert and LTS outsert..... | 61 |
| 2.4. | Conclusions | 62 |

Chapter 3. Current distribution in HTS stacked cable

| | | |
|--------|--|----|
| 3.1. | Numerical analysis of twisted stacked cable..... | 64 |
| 3.1.1. | Electromagnetic behavior of twisted stacked cable | 64 |
| 3.1.2. | Numerical setup..... | 65 |
| 3.1.3. | Non-insulated non-twisted stacked cable | 70 |
| 3.1.4. | Non-insulated twisted stacked cable..... | 72 |
| 3.1.5. | Insulated twisted stacked cable | 76 |
| 3.1.6. | Influence of magnetization on field quality | 80 |
| 3.1.7. | Summary of non-insulated and insulated twisted stacked cable | 81 |
| 3.1.8. | Partially-insulated twisted stacked cable..... | 82 |
| 3.2. | Experiment of current distribution | 90 |
| 3.2.1. | Experimental setup | 90 |
| 3.2.2. | Current distribution at 77 K in self-field..... | 93 |
| 3.3. | Conclusions | 95 |

Chapter 4. Mechanical challenges of the twisted stacked/block-type HTS insert

| | | |
|--------|--|----|
| 4.1. | Baseline for mechanical architecture | 96 |
| 4.1.1. | Mechanical forces under operation..... | 96 |

| | |
|---------------------------------------|-----|
| 4.1.2. Mechanical reinforcement | 97 |
| 4.2. Mechanical analysis | 99 |
| 4.2.1. Straight part | 99 |
| 4.2.2. Magnet ends | 102 |
| 4.3. Conclusions | 104 |
| Conclusions | 105 |

Preface

The main objective of my work has been the study of a high T_C superconducting (HTS) dipole insert using a twisted stacked cable for particle accelerator in the framework of EuCARD2 project in CERN. It is called a Twisted Stacked/ Block-type HTS insert. It is to upgrade the beam of energy in present Large Hadron Collider (LHC) by increasing the magnetic field of dipole magnet from 8.3 T to 16 – 20 T range. This is only possible by using the HTS materials. In EuCARD2 project of Work Package 10 ‘Future Magnets’, it is aimed to design and build a 5 T HTS dipole insert operated inside a 13 T low T_C superconducting (LTS) dipole outsert. In addition, it requires a 10 kA-class HTS cable. The works are mainly classified into:

- 2D/ 3D Electromagnetic design for HTS dipole insert using analytical approach
- Electromagnetic behavior (magnetization and current distribution) of HTS twisted stacked cable using numerical (FLUX) and experimental approaches
- Mechanical architecture of HTS dipole insert using numerical approach

In chapter 1, the cutting-edge technology of a superconductor used in the accelerator magnets is introduced from its fundamental behavior to its application level. In addition, a HTS cable using a ReBCO tape was presented to achieve a 10 kA-class operating current for its reliability.

In chapter 2, we built a dedicated 2D analytical code to design a 5 T twisted stacked/ block-type HTS insert under EuCARD2 dimensional and physical constraints. It is to optimize the electromagnetic behavior taking into account a twist transposition in magnet ends at first design stage. The optimization was based on the assumption that the operating current density in the cable is homogeneous. On the other hand, the 3D magnet end architecture with a twist transposition was built based on the winding topologies of racetrack flat and flared-end coils. However, the magnetic field is likely to penetrate in bad orientation of a ReBCO tape, which can lower the superconducting properties. Therefore, the magnet ends are numerically studied to see the operational margin under LTS outsert.

In chapter 3, the current distribution of a HTS twisted stacked cable is studied using a numerical and experimental approaches. It is to see its influence on the accelerator performance. We used a numerical software called ‘FLUX[®]’ by Cedrat, which provides various environments to solve the problem such as a superconductor. Moreover, it can also represent the twisted stacked cable both in 2D and 3D. However, due to the complexity in 3D meshing, the numerical analyses were done in a simplified straight conductor instead of a coil. In the experimental part, a half U-turn coil using a four-tape twisted stacked cable was tested at 77 K in self-field, which was not possible in a numerical analysis. It is also to see its long-term behavior more than 20 minutes.

In chapter 4, the mechanical architecture of twisted stacked/ block-type HTS insert is introduced both at straight part and in magnet ends of dipole magnet using a numerical approach. The objective is to minimize the mechanical deformation at straight part to keep the high accelerator performance; while it is to study the mechanical behavior particularly the shear stress at twist part in magnet ends.

Chapter 1

Introduction: Superconducting particle accelerator for quest of fundamental structure of the universe

1.1. Particle accelerator

1.1.1 Purpose and aim

Particle physics deals with the understanding of the fundamental laws of the universe. The Standard Model represents the most advanced theory of our understanding; yet many unsolved inconsistencies exist in the Standard Model, and especially at high-energy. These were the conditions just after the Big Bang, when the high-energy particles collided. A particle accelerator helps recreating the same high-energy conditions by progressively increasing the energy of beam particle, with electric fields accelerating the particles, while magnetic fields steer and focus them. Two types of particle accelerator are in use today: linear and circular. In a linear accelerator, beam particles are accelerated in a single pass; while a circular accelerator accelerates repeatedly the beam particle in a circular ring, hence reaching higher energy. Usually, massive particles such as protons and ions, which require more energy to reach the speed of light, are adapted to circular accelerators. On the other hand, light particles like the electrons are adapted to the linear accelerator. This is because the energy loss per turn is $\propto E^4/m_0^4$ at a given radius of curvature, which requires the heavy mass of the particle m_0 to reach a higher beam energy E .

The maximum beam energy E [TeV] of a circular particle accelerator is defined by the radius of its circle R [km] and the strength of the dipole magnetic field B [T] are given:

$$E = 0.3 \cdot R \cdot B \quad (1.1)$$

The Large Hadron Collider (LHC) in CERN has a circumference of 27 km and a dipole magnetic field of 8.33 T, which results in $E = 14$ TeV. It is the world's largest and most powerful circular particle accelerator today. It announced on 4th July 2012 the discovery of Higgs Boson that implies the existence of Higgs field and explains the origin of mass [1, 2]. It was the last undiscovered particle in the Standard Model. Now, the aim of the LHC is to unveil new physics beyond the Standard Model.

Some theories predict that a whole new set of particles, called as supersymmetric particles, only interacting with the field associated with the Higgs Boson will provide more direct clues to mysteries such as the invisible dark matter and energy. Therefore, a more precise measurement of the Higgs Boson is expected to be an interconnection between the Standard Model and new physics theories. So, there is still a need to design and build new accelerators with higher energy, thus calling for higher magnetic flux density

1.1.2 Magnetic system of the LHC

The Large Hadron Collider in CERN involves three main operations [1, 3 - 6]:

- Path guidance and focusing: dipole, quadrupole, sextupole, octupole etc.
- Acceleration: radiofrequency cavities.
- Detection of the particles from the collision is detector: ALICE, ATLAS, CMS and LHCb.

These are the succession of a large variety of superconducting magnets. The LHC has eight octants with a total circumference of 27 km (Figure 1.1). Every octant is made of the arc and long straight sections. Four interaction regions at straight section are reserved for the collision experiments ALICE, ATLAS, CMS and LHCb. The detectors, ATLAS and CMS, investigate a wide range of physics. The ALICE is a heavy-ion detector to study the physics of strongly interacting matter such as the quark-gluon plasma. The LHCb is specialized in investigating the slight differences between matter and antimatter. The remaining straight sections are used for the beam support, as there are accelerations by the radiofrequency cavities. All the arcs have 23 or 24 arc cells made of two identical half-cells. The arc half-cell contains three two-in-one 8.33 T dipoles of 15 m long, one two-in-one quadrupole and various sets of correcting magnets. As a consequence of these subsequent performances, the beam of particles of protons reaches the collision energy.

A beam of particles is pre-energized with several steps before it goes into the LHC. At first, the Linac 2, a linear accelerator, accelerates the beam of particles to energy of 50 MeV. Then, they are injected to the Proton Synchrotron Booster (PSB), the Proton Synchrotron (PS) and the Super Proton Synchrotron (SPS) where they are powered to 450 GeV. The beam of particles is transferred into two beam pipes of the LHC running in opposite direction. They are accelerated to energy up to 7 TeV and collide at the detection point with a total energy up to 14 TeV.

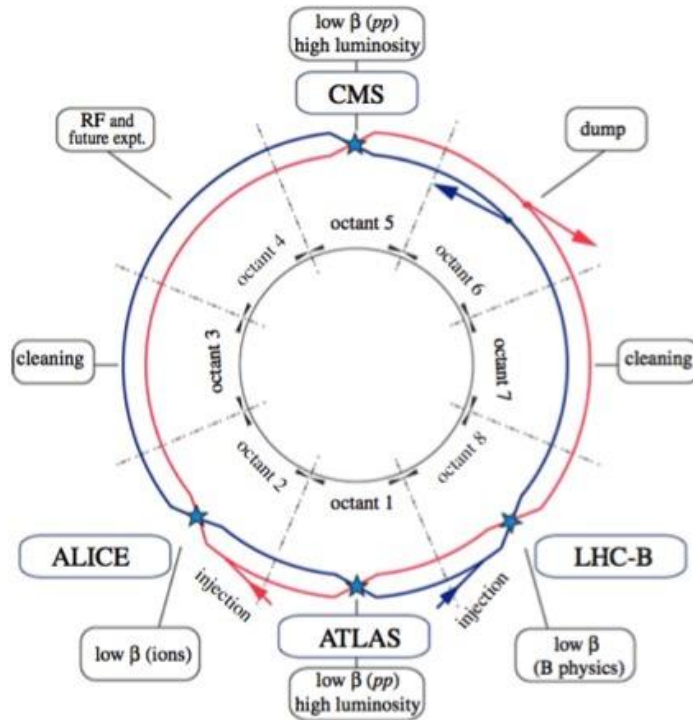


Figure 1.1 Schematic layout of the LHC [3].

In the LHC, 1232 dipoles and 392 quadrupoles are installed to keep the beam of particles in a circular orbit and to focus them, respectively. In addition to these two main magnets, about 4,000 corrector's magnets are installed. Almost all of the LHC superconducting magnets use the two-in-one design due to the space limitations in the narrow LHC tunnel and need to keep costs down [3 - 8]. However, this makes the magnet structure complicated, especially the dipole magnets where the separation of two beam channels is small enough that they are coupled both magnetically and mechanically. Two-in-one superconducting magnets are accommodated into a common cold mass cryostat filled up with the superfluid helium at 1.9 K, which increases the current capacity of superconductor at high fields (Figure 1.2). It has a 16.5 m of overall length with ancillaries, an external diameter of 570 mm and a mass of about 27.5 t. The main 15 m long two-in-one 56 mm aperture dipole magnets generate the opposite direction of 8.33 T magnetic fields to circulate the beam of particles in counter directions. It forms a double layer $\cos\theta$ geometry composing four sectors at inner layer and two sectors at outer layer. The cable is in series in all sectors and carries 11.85 kA at the rated regime. The inner and outer layers are soldered together at the extremity to form the ramp-splice region. The mechanical forces in the dipole magnet are very large pushing the coils outwards. Strong non-magnetic steel collars surrounded by an iron yoke and a stainless-steel cylinder counter these forces by pre-stressing during the magnet is assembled. It avoids the mechanical deformation of the coils in order to keep good field uniformity inside the beam aperture, which is key factor to achieve high accelerator's performances. The superconducting magnets have to be protected from any kinds of faults, otherwise a quench, when a magnet shifts from superconducting state to normal state, may heat and damage the magnet permanently. Therefore, quench heaters are installed to warm the entire coil very rapidly and to avoid any permanent damage.

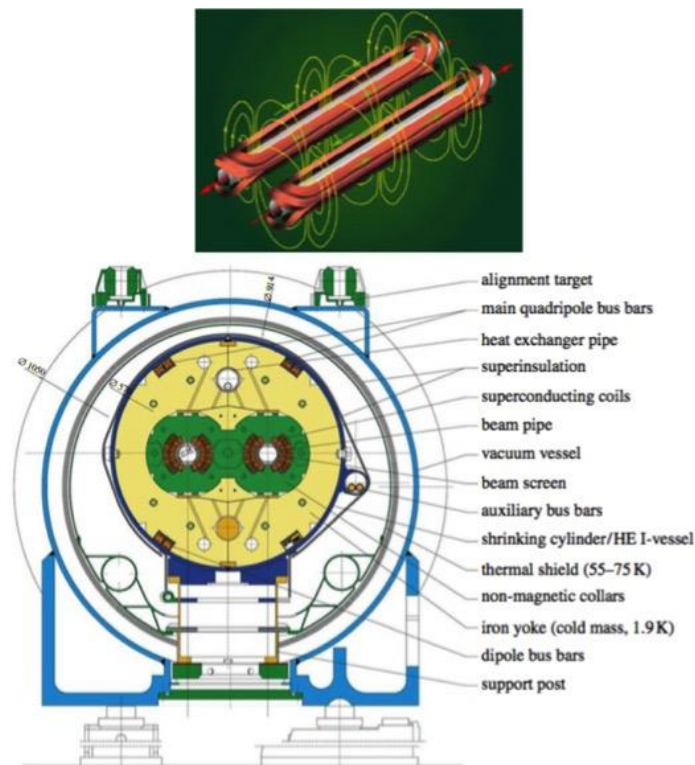


Figure 1.2 Magnetic distributions between two-in-one dipole magnets (top). Cross-section of the two-in-one LHC dipole magnet inserted in a single cryostat (vacuum vessel) due to the space limitations and good cost performance (bottom) [4].

1.2. Superconductor for accelerator magnet

The accelerator magnets rely on the cutting-edge technology of superconductor, which is capable to generate high magnetic fields with large current densities. It enabled the present LHC generating 8.33 T of field. It also meets the expectations of compactness, mechanics and cost performance. In this section, we discuss the feature of superconductor used for the accelerator magnets during normal operation and fault-mode condition.

1.2.1. Superconducting phenomenon

The superconducting phenomenon has discovered in the pure metals for the first time for more than a century ago. The electrical resistivity completely disappears under the direct current below a certain critical temperature T_C . In addition, there are two other parameters to define the superconducting critical surface: critical magnetic field H_C and critical current density J_C (Figure 1.3). These values have been developed towards the needs for the large-scale applications, which require high magnetic fields and large current densities. The superconductors made of metal alloys, compounds or oxide ceramics enable the today's high field accelerator magnets. They are called as a type-II superconductor. From the point of view of operating temperature, the type-II superconductors are classified into a low T_C superconductor (LTS) and a high T_C superconductor (HTS). The NbTi and Nb₃Sn wires are the representative LTS materials, while the Bi-2212 wire, Bi-2223 and ReBCO tapes are the HTS materials.

The accelerator magnets, e.g. NbTi in existing LHC, are in superconducting state during normal operation. It is designed to be in superconducting critical volume. The electromagnetic behaviors during superconducting state such as current and magnetic distribution inside superconductor are based on the Bean's model.

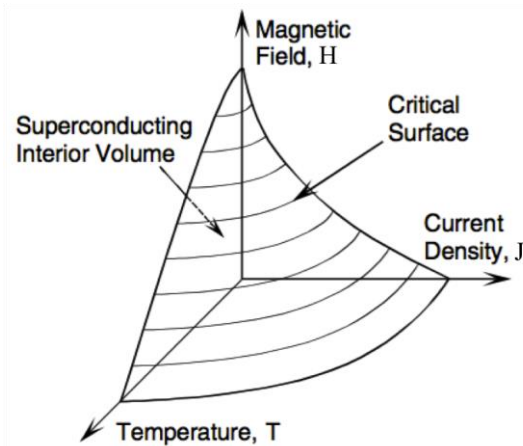


Figure 1.3 Schematic illustration of the superconducting critical surface as a function of temperature T , magnetic field H and current density J [9, 10].

1.2.2. Critical characteristic

The type-II superconductors are well expressed by the E - J power law (Figure 1.4):

$$E = E_c \left(\frac{|J|}{J_c(B, T)} \right)^{n-1} \frac{J}{J_c(B, T)} \quad (1.2)$$

Where E is the electric field, E_c is the critical electric field (10^{-4} V/m), J is the current density passing in a superconductor, $J_c(B, T)$ is the critical current density depending on the magnetic flux density and temperature and n is the steepness of the transition called as n -value. When the n -value becomes infinite, the Bean's critical state model can be deduced [9 - 11]:

$$J = \begin{cases} 0 \\ \pm J_c(B, T) \end{cases} \quad (1.3)$$

The current density in the superconductors is always either zero or the constant magnitude J_c . This is the critical state model. C. Bean assumes that J_c does not depend on the magnetic field. This model simplifies the mathematical treatment of the current distribution in a slab supplied by transport current. This is widely used for applied superconductivity.

Based on the Bean's theory, when a transport current I_t flows into a slab of width $2a$ in the x -direction and the infinite length in y - and z -directions, the current density of magnitude J_c fills up from each surface to the interior of the slab. The integration of the $J(x)$ across the slab width gives the net current equal to I_t .

$$I_t = \int_{-a}^a J(x) dx = -J_c(-a - c) + J_c(a - c) = 2J_c a \quad (1.4)$$

From the current distribution, it is possible to plot the magnetic field within the slab (Figure 1.5). The slope of the $H(x)$ is equal to J_c .

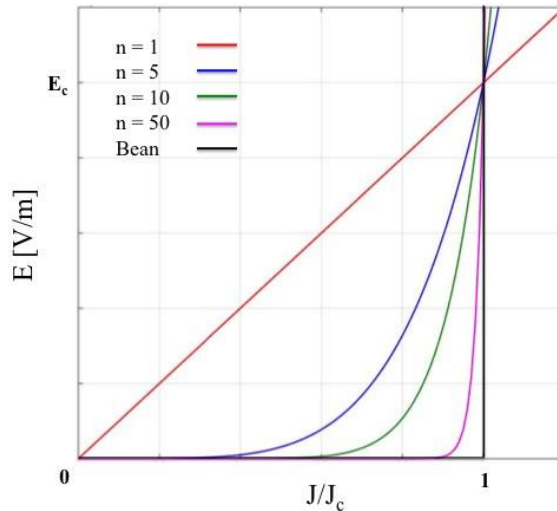


Figure 1.4 E-J power laws with various n -values.

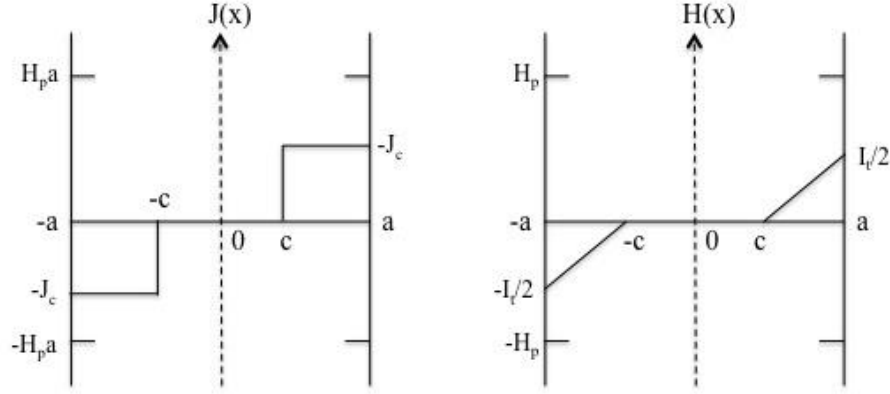


Figure 1.5 Current density $J(x)$ and magnetic field $H(x)$ across the width with transport current I_t in a slab [9, 10].

1.2.3. Magnetization

When a superconductor is subjected to a time-varying external magnetic field or transport current, the screening currents are induced [9 - 12]. They lead to a magnetization. Bean's model enables some analytical calculation.

We first consider a slab (width $2a$) submitted to an external magnetic field H_e (Figure 1.6). The external magnetic field penetrates in the slab from the outside. The penetration depth is given by the critical current density, which creates a magnetic field in opposite direction to the external one.

$$w_p = \frac{H_e}{J_c} \quad (1.5)$$

This penetration depth is limited by the half width of the slab: the external field is then called the penetration field H_p .

$$H_p = J_c a \quad (1.6)$$

The current density of magnitude J_c flows inside the slab where the field is penetrated. For external field lower than the penetration field $H_e \leq H_p$:

$$\begin{aligned} H(x) &= 0 & (-c \leq x \leq c) \\ H(x) &= H_e - J_c(x + a) & (-a \leq x \leq -c) \\ H(x) &= H_e - J_c(x - a) & (c \leq x \leq a) \end{aligned} \quad (1.7)$$

It continues until the whole conductor is carrying J_c , at which point of the field has fully penetrated in dashed line. For $H_e > H_p$, the magnetic field distribution $H(x)$ shifts up in dotted line.

If the external field decreases from H_{e1} to H_{e2} , currents are reduced from the outside to trap it (Lenz's law). When it vanishes ($H_e = 0$), currents are still flowing within the slab, which gives a remanent magnetization.

$$M_{slab} = J_c a \quad (1.8)$$

It is defined as the magnetic moment per unit volume.

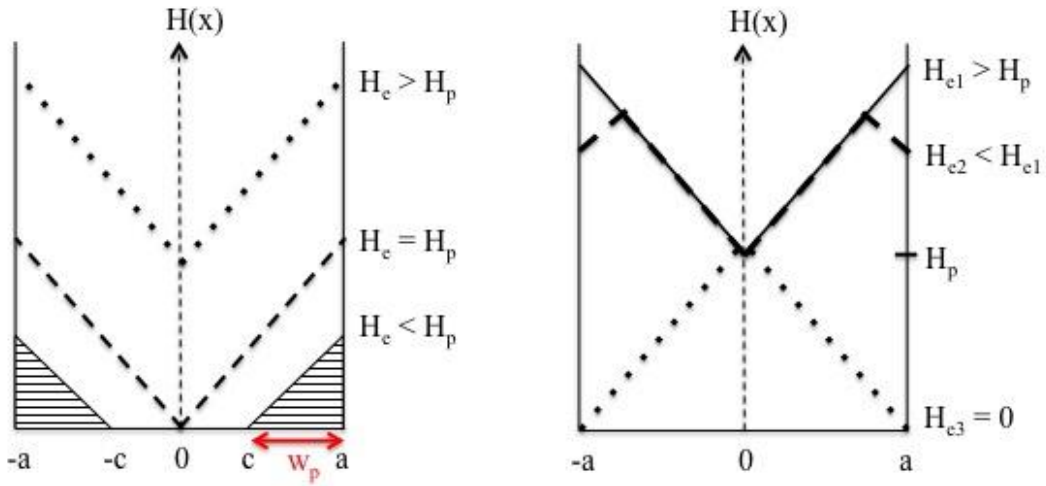


Figure 1.6 Magnetic field $H(x)$ in a slab exposed to external field (left) and during external fields are reduced $H_{e1} \rightarrow H_{e2} \rightarrow H_{e3}$ [9, 10].

In a filament, the phenomena are the same but the currents flow in the form of shell with outer radius r (Figure 1.7) [9]. The remanent magnetization is then:

$$M_{filament} = \frac{4}{3\pi} J_c r \quad (1.9)$$

When superconductor is in form of a tape, one has to pay attention for the orientation of the external field to tape's surface. The ReBCO tape of HTS material has rather thin thickness a than its width b ($a \ll b$). It is obvious that the magnetization becomes low in parallel field and high in transverse field (Figure 1.8).

The main properties of superconductors during normal operation have been presented including the well-used Bean's model. Now, we will study the protection of a superconducting magnet when it quenches that means when it loses its superconducting state.

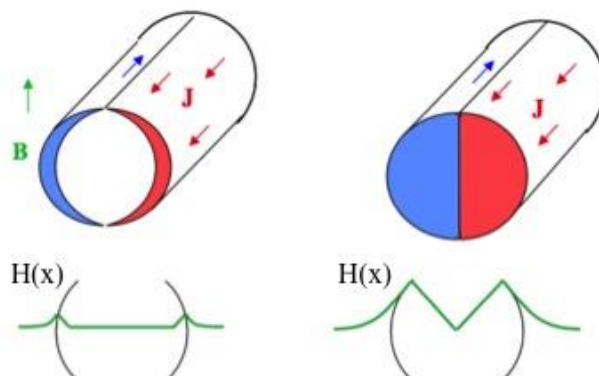


Figure 1.7 Screening current flowing in a filament with partial penetration (left) and full penetration (right) [9].

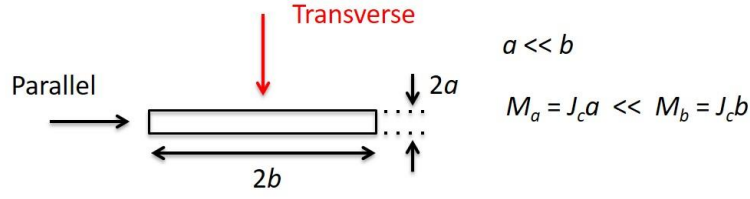


Figure 1.8 Field penetrations to a tape (thickness: a and width: b) in parallel and in transverse directions.

1.2.4. Quench

A superconducting magnet is designed not to quench (loss of the superconducting state), but this is an always-possible event when it exceeds the minimum quench energy (MQE). It must be designed not to damage after a quench, in other words, it must be protected. This first quenched zone is usually much localized where J_c of superconductor is lower. It generates joule heating at the quenched part and thus the temperature of magnet locally increases called hot spot. Then, it propagates with normal propagation velocity ($NZPV$). The hot spot temperature is overestimated in adiabatic conditions [13 - 16]:

$$\rho(T)j(t)^2 = C_p(T) \frac{dT}{dt} \Rightarrow j(t)^2 dt = \frac{C_p(T)}{\rho(T)} dT \quad (1.10)$$

Where ρ is the average electrical resistivity, j is the current density in the conductor and C_p is the average specific heat. The integration of this equation gives the hot spot temperature T_{max} .

$$F(T_{max}) = \int_0^{\infty} j(t)^2 dt = \int_{T_{op}}^{T_{max}} \frac{C_p(T)}{\rho(T)} dT \quad (1.11)$$

The first action of the quench protection system is to detect the quench as soon as possible. The most common quench detection technique is based on the detection of voltage rise. When the quench is detected after the real quench t_{det} , the classical technique is to disconnect the magnet from its power supply and to discharge its energy into an external dump resistor R_{dump} (Figure 1.9). The magnet resistance after quench R_{quench} is neglected compared to the dump resistance. The time evolutions of current and current density are given by:

$$I(t) = I_0 \exp\left(-\frac{t}{\tau_{dump}}\right) \quad (1.12a)$$

$$j(t) = j_0 \exp\left(-\frac{t}{\tau_{dump}}\right) \quad (1.12b)$$

Where τ_{dump} is the time constant of the dump resistor.

$$\tau_{dump} = \frac{L}{R_{dump}} = \frac{2E_m}{V_{max}I_{op}} \quad (1.13)$$

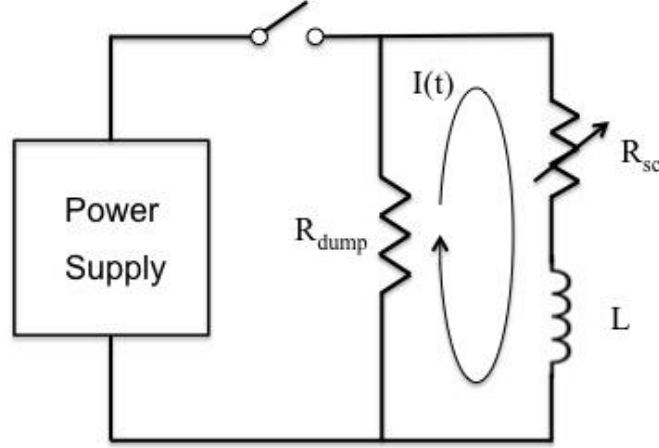


Figure 1.9 Quench protection circuit with an external dump resistance [13, 14].

It can be rewritten using the magnetic energy $E_m (= LI_{op}^2/2)$ and the peak discharge voltage $V_{max} (= R_{dump}I_{op})$. The time integration of the square of the current density in Eq. (1.11) then can be rewritten introducing the relevant quantities.

$$F(T_{max}) = \int_0^{\infty} j(t)^2 dt = j_{op}^2 \left(t_{det} + \frac{\tau_{dump}}{2} \right) \quad (1.14a)$$

$$= j_{op}^2 \left[t_{det} + \frac{E_m}{V_{max}} \times \frac{1}{I_{op}} \right] \quad (1.14b)$$

Where j_{op} is the operating current density of the cable. This equation gives the parameters to protect a magnet. One can assume that the hot spot temperature can be reduced by:

- Large heat capacity $C_p(T)$ and small resistivity $\rho(T)$ of superconductor
- Small magnetic energy E_m and operating current density j_{op}
- Quick detection (small t_{det})
- High possible terminal voltage V_{max}
- Large operating current I_{op}

First one is based on the right side of Eq. (1.11). It deals with the material properties of the superconductor. On the other hand, the others are basically about the magnet design. Generally, once the magnet design with the given magnetic energy and operating current density is determined, the only way to limit the hot spot temperature is by increasing the operating current and the terminal voltage. For the LHC dipole magnets, the maximum terminal voltage is set as 1 kV, ± 500 V to ground by means of the grounding circuits.

In conclusion, the firm protection can be achieved with large operating current of a superconducting magnet and low possible resistivity of conductor in normal state.

1.2.5. Current densities

High field accelerator magnets rely on large current densities in superconductor. In addition, the requirement to reduce the conductor cross-section is also translated in

a practical demand of large current densities. It is indicated as the overall current density per total conductor cross-section $J_{overall}$. Assuming the accelerator dipole magnet in shape of $\cos\theta$, the center field B_1 depends on the thickness w and the central arc angle of the sector θ (Figure 1.10) [3, 6, 7]:

$$B_1 = \frac{2\mu_0}{\pi} w J_{overall} \sin \theta \quad (1.15)$$

For 60°-sector coil in the LHC ($B_1 = 8.33$ T and $w = 30$ mm), it requires at least $J_{overall}^{min} = 400$ MA/m². The $J_{overall}$ will anyway be higher than 400 MA/m² for higher center field requirements. Moreover, there are other materials such as insulation and voids in sector coil, which reduces the effective cross-area of superconductor. One has to know the higher current density induces higher temperature at the quench hot spot and higher mechanical stress. These may degrade the J_C of superconductor.

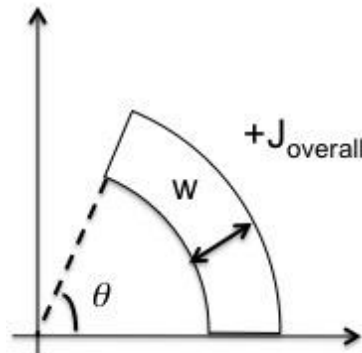


Figure 1.10 $\cos\theta$ dipole magnets with a single layer of sector coil.

1.2.6. Mechanics

The superconducting magnets experience thermal contraction during cool-down and Lorentz forces during normal operation. Besides, winding stresses can be applied during fabrication. The dipole magnets have to support these forces in order to [3, 9]:

- Prevent any sudden movement leading to quenching
- Limit the deformation of conductor to maintain the original position
- Keep initial high current carrying capacity of superconductor

In $\cos\theta$ layout in LHC, Lorentz forces tend to push the coil towards the midplane in vertical/ azimuthal direction and outwards in the radial-horizontal direction [3 - 5]. It results in tensile stresses in the coil. It is difficult to protect the superconductor and other materials such as insulation by the coil itself. Therefore, these forces must be counteracted by an external support structure. Usually, the external structure also applies a radial inward pre-compression during cool-down. It is then transformed into an azimuthal compression inside the coil under Lorentz loads. The simplest structure is a cylindrical shell to provide the external pre-compression. In conclusion, an adequate mechanical reinforcement supports the coil from the mechanical forces. It also helps to minimize the deformation to keep the designed field quality inside the beam aperture.

1.2.7. Field quality

An almost unique characteristic of accelerator magnets is the necessity of high field quality in small beam aperture [3 – 7, 17]. In dipole magnets, it produces bending fields to keep the beam of particle in circular orbit. The field harmonics of the superconducting accelerator magnet are generally divided into two categories: geometric and magnetization/ screening current.

The geometric field quality is attributed to the homogenous current distribution in the superconductor. Figure 1.11 shows the ideal dipole magnet represented with two intersecting circles carrying uniform current density J . In reality, the magnets are consists of sector coil or block. They are usually designed to represent the ideal geometry with subdivided conductors. However, it generates field errors due to the disagreement to the ideal cross-section.

One has to take into account harmful impact of magnetization and screening current, which are one of the features of superconductor. The field penetration into superconductor induces the screening current in coil. It generates supplementary field harmonics. As we have seen, the magnetization depends on the shape of conductor. In addition, for the tape, the field penetration in parallel orientation brings less magnetization impact on field quality than in transverse orientation.

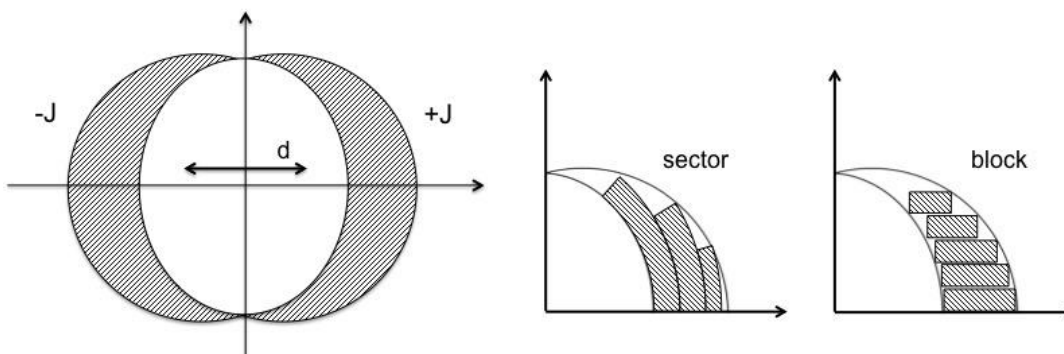


Figure 1.11 Ideal dipole magnet (left) and practical approximation using sector coil (middle) and block (right) [6].

1.2.8. Cost

Typically, the superconducting magnet has a higher initial cost, but a lower operating cost than conventional magnet [6, 7, 17]. The requirement for cooling with liquid helium is only cost-competitive with conventional systems in large scale. The cost for the machine alone in LHC is about 5,000 MCHF including materials and personnel. In the LHC main dipole magnets, the superconductor (NbTi) accounts for approximately one third of total cost per magnet that is 300 kCHF out of 1 MCHF, while 300 kCHF of component, 300 kCHF of assembly and 100 kCHF of cryostat and testing. This results in about 1,200 MCHF (360 MCHF of superconductor) in total for all dipole magnets in LHC. One can assume that if the cost of superconductor increases by 100 or even 2 times, there is an economical issue.

1.2.9. Conclusion: Superconducting requirement for accelerator magnet

The main highlights for high accelerator dipole magnet performance in LHC are:

- Good field quality in beam aperture
- High fields with large operating current densities $> 400 \text{ MA/m}^2$
- 10 kA-class operating current for fast detection
- Strong mechanical structure to keep its designed position

These requirements are achieved from a point of view of magnet design and superconducting material. For magnet design, the operating current density J_{op} influences on protection, mechanics and cost performance. The larger J_{op} contributes to reduce total conductor cross-section A_{cond} , i.e. total price of superconductor. However, the protection and mechanical architecture gets more difficult. The operating current I_{op} is simply derived from J_{op} , A_{cond} and the number of turn, in other words, the number of subdivided conductor.

$$J_{overall} = I_{op}N_{turn}/A_{cond} \quad (1.16)$$

The material properties of superconductor apart from magnet design play an important role in operational margin. Of course, the critical values are preferred to be as high as possible. Besides, the superconductor with stabilizer and strong mechanical materials can improve the protection and mechanics.

1.3. Superconducting material for accelerator magnet

Figure 1.12 shows the dependency of the engineering current density J_e to the magnetic fields at 4.2 K except for NbTi at 1.9 K [18]. Moreover, the required $J_{overall} = 400 \text{ MA/m}^2$ is added as red dashed line [3, 6]. Taking into account the operational margins to required $J_{overall}$, one can see that there is a field limit for NbTi at 8 T and Nb₃Sn at 15 T. On the other hand, the HTS materials, BSCCO and ReBCO conductors, still maintain high current carrying capacities at more than 20 T. From an economical point of view, NbTi, whose manufacturing techniques are well established, is the most reasonable material that is 200 \$/kg. Thus, it is used in the existing LHC (See §1.2.8). Nb₃Sn and HTS materials are five and fifteen times expensive than NbTi, which are 1000 \$/kg and 3000 \$/kg respectively [6, 7, 19].

In future LHC, they aim to upgrade the beam of energy by increasing the magnetic field from 8 T to 20 T ranges [6, 20, 21]. It is inevitable to use Nb₃Sn and HTS materials. The first hybrid magnet, which is composed of 5 T HTS insert and 15 T LTS outsert, is proposed in the framework of EuCARD project (Figure 1.13). The proportion of the magnets takes into account for the cost and the best use of material. In this section, we discuss the superconducting materials related to the practical and designed accelerator dipole magnets.

- NbTi: present LHC dipole
- Nb₃Sn: FRESCA2 dipole outsert in EuCARD project
- HTS material: 5 T insert in EuCARD project

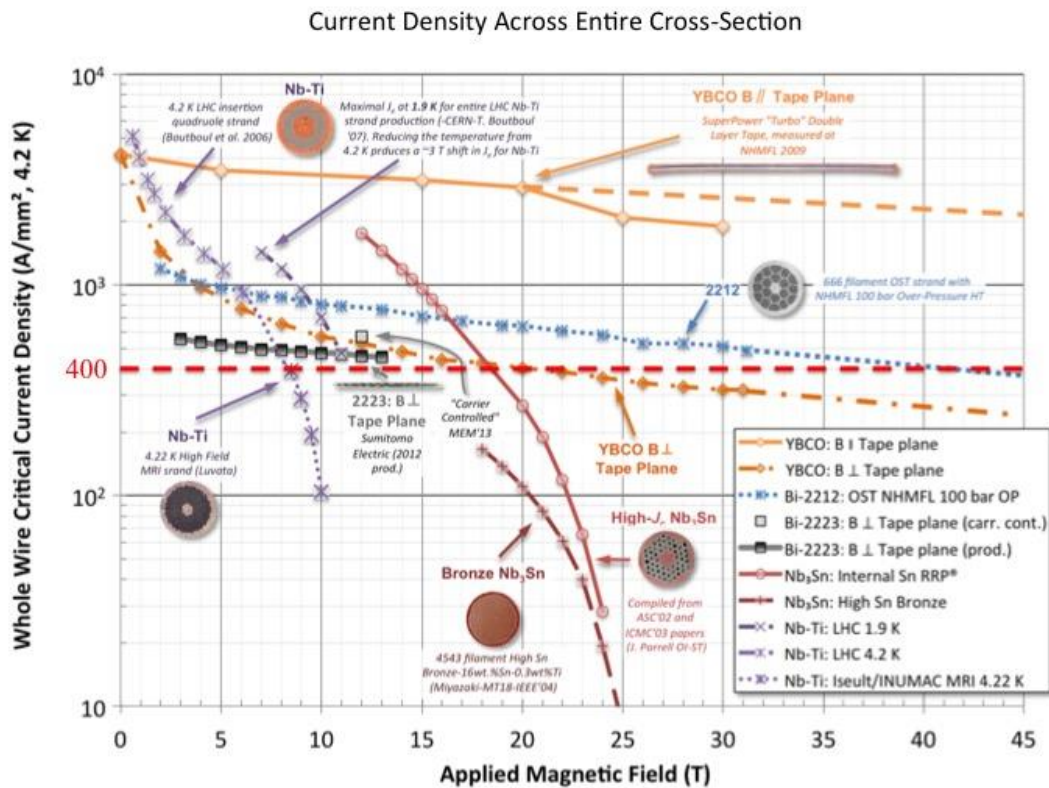


Figure 1.12 Comparison of engineering current densities J_e at 4.2 K for various LTS and HTS materials [18].

Table 1.1
Specification of 1st possible hybrid magnet in HE-LHC project [6, 20]

| Material | No turns | Proportion | Peak field | J _{overall} (A/mm ²) |
|----------------------------------|----------|------------|------------|---|
| NbTi | 41 | 27% | 8 | 380 |
| Nb ₃ Sn (high J_C) | 55 | 37% | 13 | 380 |
| Nb ₃ Sn (low J_C) | 30 | 20% | 15 | 190 |
| HTS | 24 | 16% | 20.5 | 380 |

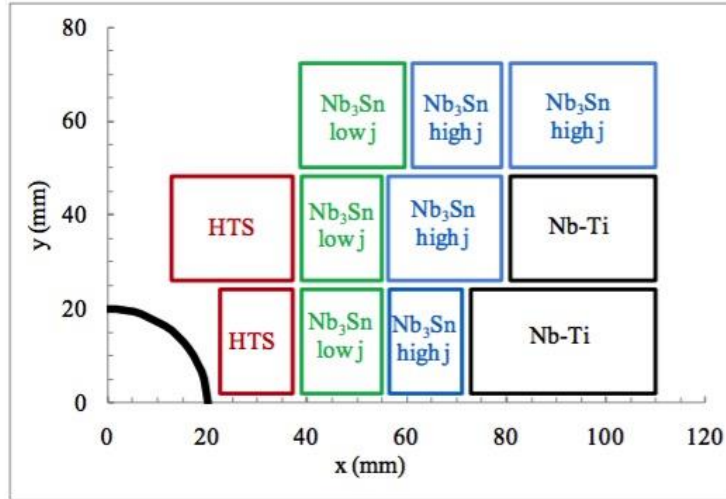


Figure 1.13 First hybrid HTS insert/ LTS outsert design using NbTi, Nb₃Sn and HTS in HE-LHC project [6, 20].

1.3.1. Low T_c superconductors

LTS materials used in high field magnets have contributed for the particle accelerator physics so far [22 - 24]. NbTi and Nb₃Sn in form of a wire enabled the 10 kA-class superconducting cable, which meets the expectations for accelerator magnet.

1.3.1.1. NbTi

The 8.33 T operated field in the LHC is the upper limit of NbTi material at 1.9 K of superfluid helium. A ductile NbTi wire is made of many fine filaments of superconductor embedded in a matrix of ordinary metal that is often the copper (Figure 1.14) [25, 26]. In the LHC, multi NbTi wires form a classical Rutherford-type cable to answer the 10 kA-class operating current [24, 27]. The Rutherford-type cable has been developed over the years to suppress some of the stability disturbances that are the wire motion, flux jump and AC losses. Therefore, it has the twisted multifilament-strand structure to transpose all positions of NbTi wires and thus to equalize the magnetic condition (See §1.4 for transposed cable). From a structural point of view, the ductility of NbTi can adapt the cable into the trapezoidal shape in order to be wound the 56 mm aperture $\cos\theta$ layout [8].

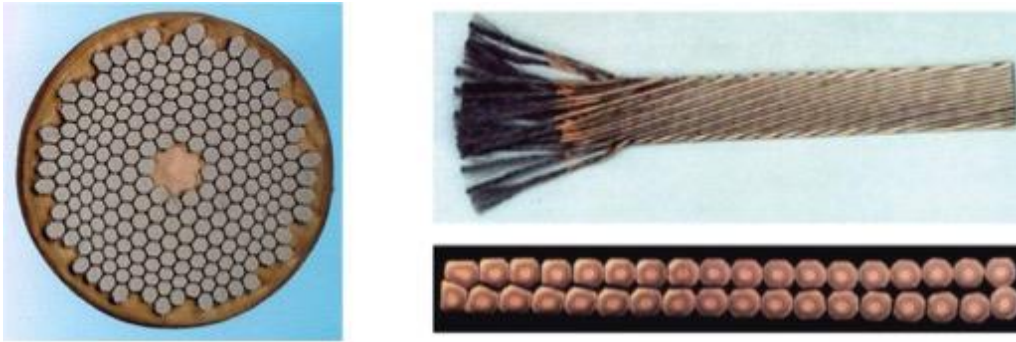


Figure 1.14 NbTi composite wire (left) and the Rutherford-type cable with multifilament structure used in the LHC (right) [4, 5].

1.3.1.2. Nb_3Sn

Nb_3Sn wire is the next prime technology to upgrade the magnetic field over 15 T [28]. It has the same composite structure as NbTi wire, which is able to form into the Rutherford-type cable. However, it is very brittle and much more difficult to process than NbTi. Their critical values depend on applied stress and strain. The tensile strains of only a few tenths of a percent during the heat treatment and cabling are sufficient to degrade the J_e [29 - 31]. Therefore, it requires special manufacturing techniques, which results in slow production speed.

The Nb_3Sn high-field accelerator magnets are now at preparatory step for the test [32 - 35]. In the framework of EuCARD project [32], Nb_3Sn magnet called as FRESCA2 LTS outsert has been designed (Figure 1.15) [37, 38]. It has 100 mm aperture and generates a 13 T field. The magnet is wound with a Rutherford-type cable composed of 40 strands with a diameter of 1mm. Since the fields get higher, larger stored energy and Lorentz forces are foreseen in the magnet. Therefore, one has to take more consideration for protection and mechanical architecture [39 - 41].



Figure 1.15 Design of FRESCA2 LTS outsert using Nb_3Sn in 2D at straight part (left) and in 3D magnet ends (right) [37].

1.3.2. High T_c superconductors

The potential of HTS materials can achieve 20 T range high field accelerator magnets [42]. The HTS inserts are expected to be compact (smaller size) under higher magnetic fields with larger operating current densities than LTS magnets, which makes viable in the marketplace. Thus, these severe operating conditions including stability and mechanics ask for high quality HTS materials.

The production in long length (in the range of several hundreds of meters) is still challenging technology [43 - 48]. There is inhomogeneity in critical current along the conductor length, which creates the weak zone. This may initialize the quench. However, one has to know the HTS insert has distinctly different quench behavior due to high operational margin in temperature that is $T_C = 90 - 100$ K range to $T_{op} = 4.2$ K. For this reason, it has very slow normal zone propagation of velocity, which makes difficult to protect [49, 50].

1.3.2.1. Bi (2212/2223)

BSCCO is the first high-temperature superconductor to be used for making superconducting wires. It has two types: Bi-2212 round wire [43] and Bi-2223 tape [44]. Both of them can be made via the power-in-tube process with Ag or Ag alloy tubes (Figure 1.16).

The J_e of Bi-2212 wire is between that of Nb_3Sn wire and ReBCO tape. It can adapt the conventional cabling methods such as Rutherford-type cable [51, 52]. Moreover, it has the isotropic dependency to the field angle. However, due to the complexity of its heat treatment and relative lack of mechanical strength and stiffness of Ag and Ag-alloy, Bi-2212 conductors are highly strain sensitive [53 - 55]. Furthermore, the options for insulation are limited because the oxygen is required during its processing. Bi-2212 HTS insert design is part of the U.S. program supported by US-BSCCO collaboration based on the Canted Cosine-Theta (CCT) geometry [56 - 58].

Bi-2223 tape has the anisotropic dependency to the field angle [59]. The J_e becomes lowest in transverse orientation, which is below than Bi-2212 and ReBCO. In addition, the critical stress limits are in 90 - 270 MPa range [60]. Hence, Bi-2223 tape is commonly used in low magnetic fields, e.g. in HTS power cables [61] and it is thus not adequate for high field magnets.



Figure 1.16 Cross-section of Bi-2212 wire with power-in-tube process [43] and Bi-2223 tape [44].

1.3.2.2. ReBCO

ReBCO coated conductor is Rare-earth (Yttrium etc.) barium copper oxide, which is a crystalline chemical compound [42]. A problem limiting the use of this material is the difficulty in making it into wires. The most popular method developed to utilize this material involves the deposition of thin layer of YBCO on flexible substrate coated with one or more buffering metal oxides encased in copper that is known as coated conductor (Figure 1.17). There are now two commonly used processes, Rolling Assisted Biaxially Textured Substrates (RABITs) process and the Ion-Beam-Assisted Deposition (IBAD) process. For mechanical reason, IBAD method is widely selected by tape's supplier, e.g. SuperPower [45], Bruker [47] and Theva [62] etc.

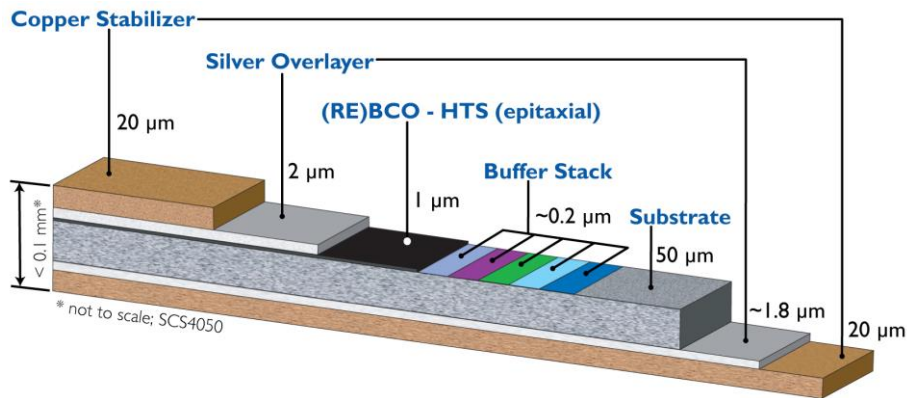


Figure 1.17 Configuration of ReBCO coated conductors by Superpower [45]

Table 1.2
Electromagnetic properties of BSCCO and ReBCO

| Parameter | OST [43] | Sumitomo [44] | Superpower [45] | AMSC [46] | Bruker [47] |
|---|-------------|------------------|----------------------|--------------|----------------------|
| Material | Bi2212 | Bi2223 | YBCO | YBCO | YBCO |
| Shape | Wire | Tape | Tape | Tape | Tape |
| Fabrication | - | - | IBAD | RABITs | IBAD |
| Product name | - | Type HT | SCS4050 | Type 8051 | |
| Stabilizer/ Substrate | Ag alloy | Ni Alloy | Copper/ Hastelloy | Cu alloy | Copper/ Hastelloy |
| Width/ Thickness [mm] | - | 4.5/ 0.31 | 4/ 0.1 | 4.8/ 0.2 | 4/ 0.2 |
| Diameter [mm] | 0.7 – 1.5 | - | - | - | - |
| I _c at 77 K in self-field | - | 200 A | 100 A | 100 A | 135 A |
| Critical tensile at 77 K | 110 MPa | 400 MPa | 550 MPa | 150 MPa | 650 MPa |
| Min. Bending radius [mm] | - | 40 | 11 | 30 | 6 |
| Producibile length | 1000 m | 500 m | 300 m | - | 300 m |

Electromagnetic property

The ReBCO coated conductor enables very high J_C in the superconducting layer and strong mechanical strength in axial tension in the substrate. Besides, the silver and copper layers are the stabilizer in case the quench occurs. However, it has strong anisotropic dependency to the magnetic field angle due to its grain alignment in superconducting layer (Figure 1.18) [63, 45 – 47, 62]. It is observable that 15° of field angle already lower the I_C for 50% while with further increase in the angle the decrease is less dramatic up to the lowest I_C at 90°.

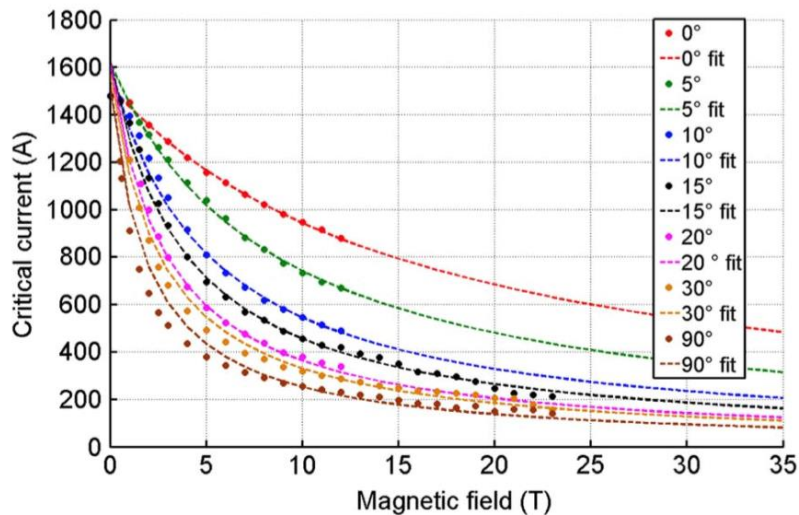


Figure 1.18 Anisotropic dependency of 4 mm wide SuperOX ReBCO tape [63]

Mechanical property

The orientation of applied stresses has an impact on the degradation of J_e . When mechanical stresses are applied on wide flat surface of the ReBCO tape (compressive pressure), the ReBCO tape can withstand up to 250 - 700 MPa [64, 65]. On the other hands, the 20 – 30 MPa of transverse stresses on thin layer can easily cause the delamination in superconducting layer. For this reason, the bending radius in wide face called as easyway bending (≈ 10 mm), can be much smaller than that of in thin face called hardway bending (an order of a few meter). One also has to consider the interfacial shear stress that is about 50 MPa at maximum.

ReBCO conductors for HTS insert

ReBCO magnets are still under the research stage and a few insert designs are reported [66, 67]. Compared to the Bi-2212 magnet, the ReBCO conductor has higher J_e and stronger mechanical strength. It also has design flexibility in the selection of stabilizer, which may be possible to optimize the mechanical and thermal behaviors for mechanical strength and quench protection. However, the wide tape structure limits the cabling methods to avoid the magnetically disturbances such as magnetization. In addition, the interfacial shear stress and delamination of the superconducting layer may become important considerations. One also has to consider a lack of manufacturability in long length with low cost.

1.4. ReBCO cable for accelerator magnet

The ReBCO conductor offers a lot of opportunities for high field accelerator magnets as an insert. However, a large current cable still remains a big issue in the cabling technology due to in the tape geometry. In this section, we discuss three possible ReBCO cables [68].

1.4.1. Roebel cable

Roebel cable is invented in the early 20th century to reduce the AC losses for the alternators. And then the ReBCO Roebel cable has been proposed by KIT in 2005 [69]. It is bundled with the meander shaped strands. The strands are continuously and fully transposed by changing the locations of every strand with every other strand along the length. It homogenizes the electrical and mechanical conditions of the tapes and avoids the forces in the cable to couple together [70 - 72]. The meander shaped is achieved by mechanical punching. It can achieve a precision less than 50 μm for the strand width and provides typically 50 m of meander shape tape per hour [73]. Usually half of the ReBCO tape is wasted. The copper stabilizer in ReBCO tape is partly smeared over the punched edge. It improves the mechanical contact to the copper layer. The 3 % degradation in J_e occurs at best. Figure 1.19 shows the meander-like tape of the original width W , the transposition length L , the strand width W_R , the strand-edge clearance W_C , the crossover width W_X , the inter-strand gap L_{ISG} , the crossover angle ϕ and the cut-off fillet radius R [74]. The strands are fit into a cable by sliding their positions of crossover part. Hence, the transposition length is important for the number of applicable strands in Roebel cable. A larger clearance width between two sides of the strand and smaller number of strands per cable length unit make easier to assemble into a cable. A sharp outer edge of the crossover section and an increase of the inner radius lead to a reduction of the Von Mises stresses under tensile loads [69, 75, 76]. Furthermore, the crossover width and the angle can be adjusted for best current performances.

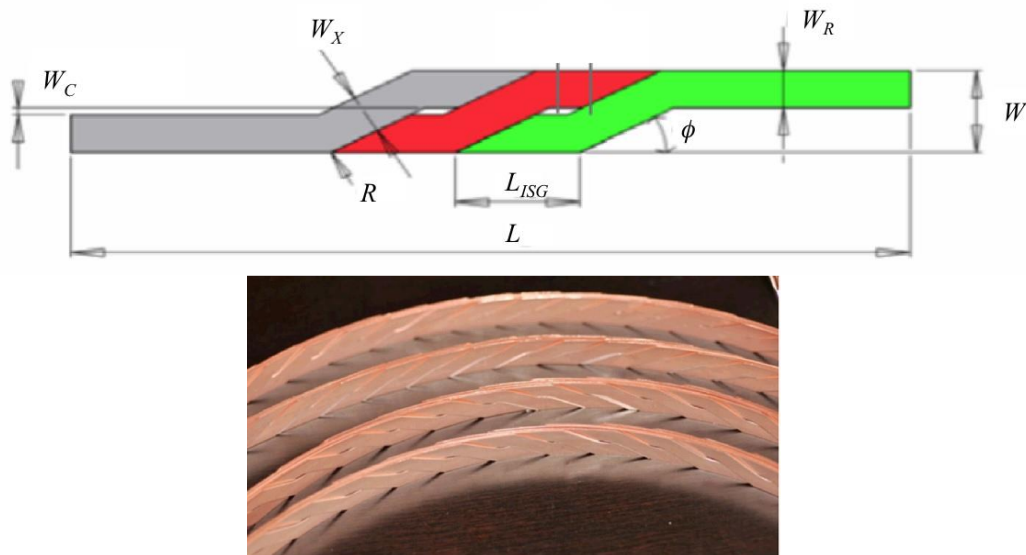


Figure 1.19 Roebel meander like strand with the key parameter [74] (top) and Roebel cable with multi dummy strands (bottom) [69].

1.4.2. CORC cable

Conductor on Round Core (CORC) cable is proposed by D. Van der Laan in 2009 [77]. It consists of ReBCO tapes, which are tightly wound around a round former in several layers using a winding angle of 45° (Figure 1.20). The winding directions between each layer are reversed. The former using a copper usually has around 5 mm diameters. It provides electrical and mechanical stabilization. The transposition of the ReBCO tapes in the CORC cable is partial. This is because the tapes of the inner layer always remain near the center, while the tapes of the outer layer stay on the cable surface. Owing to the CORC cable structure in a winding angle of the 45° , the Lorentz forces are directed to the wide surface of the ReBCO tape. It is less sensitive to mechanical loads than single tape. In high field magnets, the CORC cable can easily make 10 kA-class operating current by adding more layers of ReBCO tapes [78, 79]. However, its overall engineering current density $J_{overall}$ becomes relatively smaller than those of other HTS cable concepts due to the copper rod in center. Therefore, it is still not appropriate for high-field magnets.

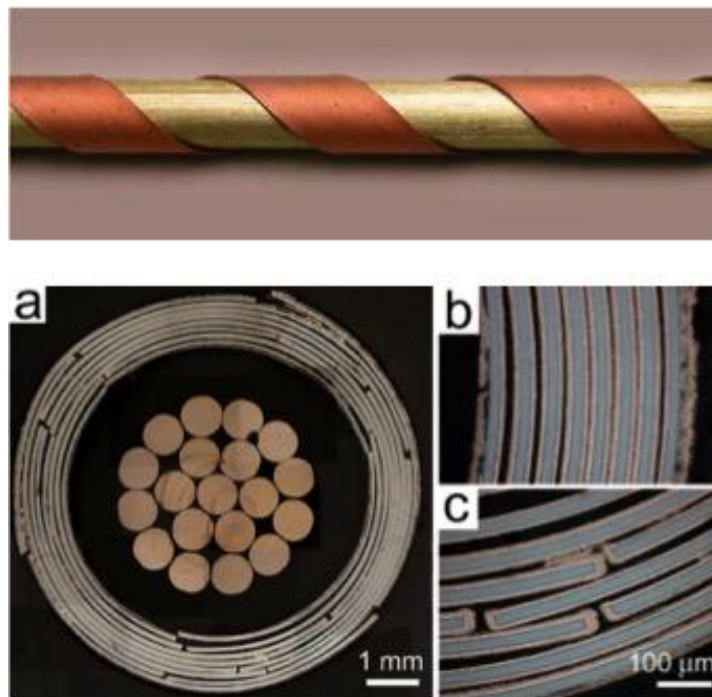


Figure 1.20 CORC cable with one ReBCO tape wound around the former (top) and the cross-section with several layers (bottom) [77].

1.4.3. Stacked cable

The simplest way to obtain the superconducting tapes into a high-current capacity and compact cable is to stack the tapes on top of the others [80]. A twist of the stacked cable called as a twisted stacked cable enables the partial transposition, which is proposed by M. Takayasu in MIT (Figure 1.21) [81 - 84]. It is typically required to reduce the screening current losses by equalizing the electromagnetic condition of the tapes in the cable, although a lack of full transposition will not decouple under self-

field. It does not waste any conductor like Roebel cable and can still bring high $J_{overall}$. A practical winding machine of a twisted stacked cable is developed in CERN, and some of winding topologies are proposed [83]. The MIT proposes the new winding of U-turn coil such as flared-end coil for the dipole magnet. Like in common electrical machine, the stack is transposed in the coil ends. A sharp winding heads consisting of the twist and the easyway bending facilitates the U-turn flared-end coil.

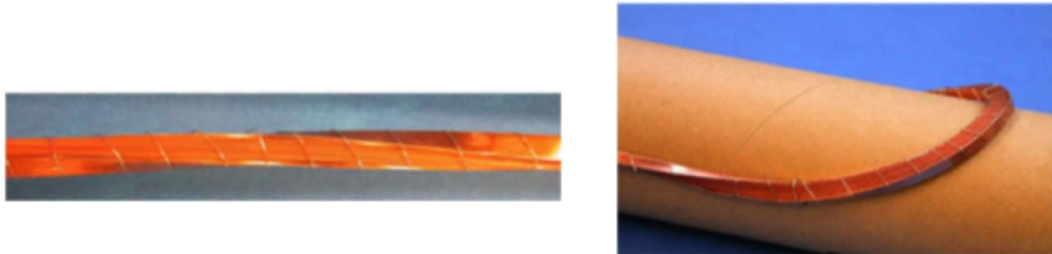


Figure 1.21 Twisted stacked cable composing 32 YBCO tape (left) and the flared-end coil with a sharp bending (right) [83].

A twist in the cable induces mechanical strain, which may degrade J_e . Therefore, a twist transposition T_P is limited [85, 86].

$$T_P = \frac{L_P}{360^\circ} < T_{P,C} \quad (1.17)$$

Where L_P is the twist pitch length for 360° twist and $T_{P,C}$ is the critical transposition pitch, which causes 2% degradation in critical current. Figure 1.22 shows the schematic view of single thin rectangular tape, whose width and thickness are $2w$ and $2t$, twisted for $\phi = 90^\circ$ along length L . The longitudinal length AB_1 parallel to the z axis at the distance x ($y = 0$) from the z axis elongates to AB_2 .

$$\overline{AB_2} = \sqrt{L^2 + (x\phi)^2} \approx L \left\{ 1 + \frac{1}{2} \left(\frac{x\phi}{L} \right)^2 \right\} \quad (1.18)$$

The tensile axial longitudinal strain ε_t of the chord AB_2 due to the torsional twist is obtained as:

$$\varepsilon_t = \frac{\overline{AB_2} - \overline{AB_1}}{\overline{AB_1}} = \frac{x^2\theta^2}{2} \quad (1.19)$$

Where θ is the twist angle per unit length ($\theta = \phi/L$). The compressive strain ε_0 is established in the central longitudinal line of the tape because that the integrated longitudinal force over tape cross-section is to be zero.

$$\varepsilon_0 = -\frac{\theta^2 w^2}{6} \quad (1.20)$$

Now the actual longitudinal strain ε_x of the summation of the tensile strain and the compressive strain is given as a function of the distance x .

$$\varepsilon_x = \frac{\theta^2}{2} \left(x^2 - \frac{w^2}{3} \right) \quad (1.21)$$

The twisted stacked cable also experiences the exact same longitudinal strain distribution as that of single tape except its thickness is thicker.

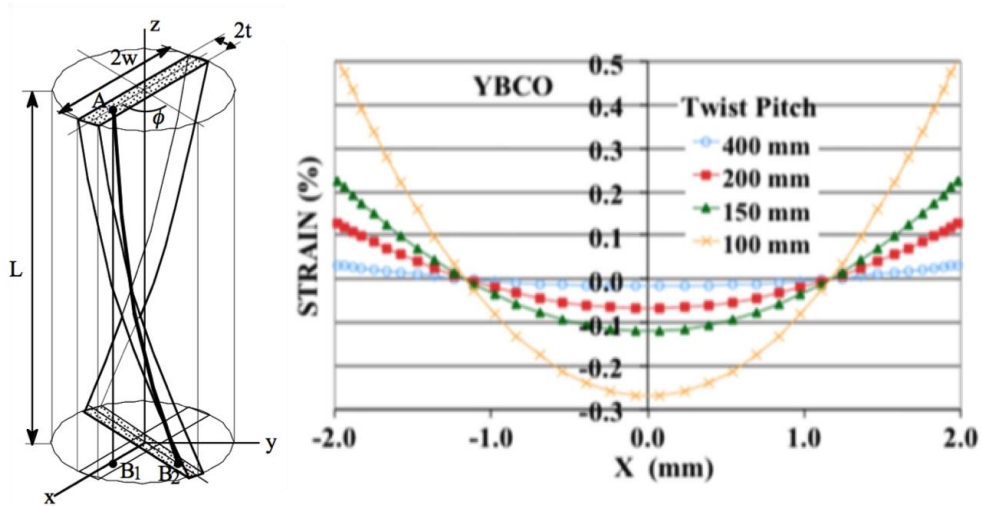


Figure 1.22 Torsional strains along the tape width [82]

Figure 1.23 shows the critical current of a twisted ReBCO tape at 77 K in self-field as a function of twist pitch length L_P [87]. It has been evaluated for various tape width $2w$ between 2 mm and 12 mm. As seen in the figure, the critical twist pitch length $L_{P,C}$ causing a 2% degradation of the critical current is approximately proportional to the tape width $2w$.

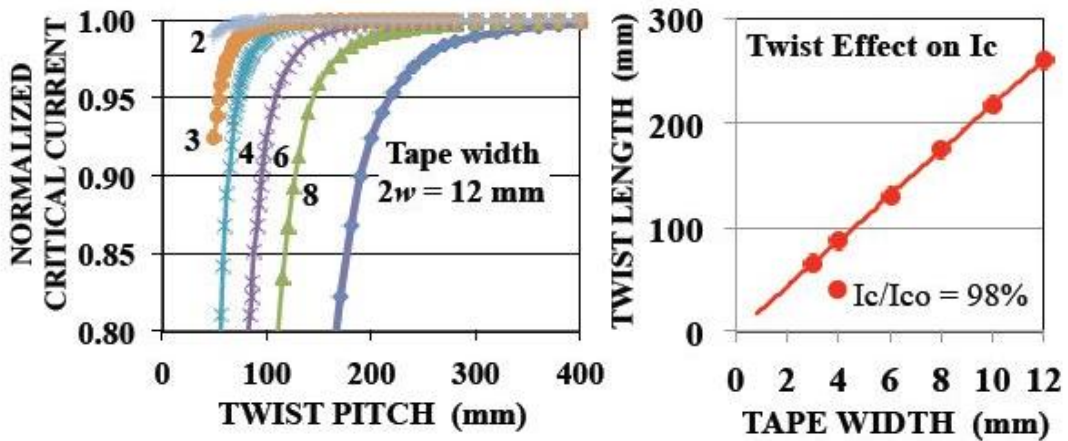


Figure 1.23 Normalized critical currents as a function of twist pitch length for various widths (left) and twist pitch corresponding to a 2% degradation of critical current as a function of tape width (right) [87].

1.5. Conclusion of study: twisted stacked YBCO cable insert

A first HTS insert focused on a block layout and using a twisted stacked cable is proposed in our work as one of three ReBCO HTS inserts in the framework of EuCARD-2 project of WP.10 ‘Future Magnets’ [88 - 92]. It is called as a ‘Twisted Stacked/ Block-type HTS insert’. This design takes advantages of simple cabling and coil assembling structures. In addition to this, it is more cost effective than Roebel design. However, several matters must be settled to use this concept for a dipole magnet as HTS insert, which is characterized in high magnetic fields and large current densities.

- Twist at straight part of dipole magnet
- Partially transposed cable
- Mechanics at twisted part

At first, the dipole magnet is essential to provide high field uniformity at straight part of dipole magnet, which has a perfect symmetric design generating only odd numbers of normal field harmonics B_3 , B_5 and B_7 . A twist at straight part may not be appropriate since the non-symmetric twisted cable structure along longitudinal axis makes difficult to achieve a good field quality. Moreover, from an operation margin point of view, it can lower or degrade its electromagnetic properties due to high transverse fields and large Lorentz forces at straight part. These are sufficient reason to locate the twist only in the magnet ends. Therefore, the cross-section of dipole magnet at straight part is designed to be a general block layout in Figure 1.13. One has to know that all physical and manufacturing complications of the twisted stacked/ block-type HTS insert exist in the magnet ends. The twisted stacked cable has to deal not only with a partial transposition but also with an absence of a continuous transposition. This will affect the magnetization and the current distribution in the stacked cable.

In this work, the overview of the twisted stacked/ block-type HTS insert is discussed in regard to the way of the design and manufacturability at straight part and in magnet ends (Chapter 2). The investigation in various structures of the twisted stacked cable leads to the appropriate magnetization and current distribution solving the deficiency of long twist transposition pitch (Chapter 3). The mechanical design at straight part and magnet ends where the twist occurs are analyzed (Chapter 4).

Chapter 2

Electromagnetic design of twisted stacked/ block type HTS insert

In the framework of the EuCARD2 project of Work Package 10.3, first HTS insert using a twisted stacked cable called as ‘Twisted Stacked/ Block-type HTS insert’ is introduced first in 2D and then in 3D. At the straight part of dipole magnet, it is required to provide a magnetic field of 5 T with high quality inside a 13 - 15 T range LTS insert. On the other hand, the twist is applied in magnet ends to achieve the partial transposition.

2.1. 2D HTS insert

2.1.1. Optimization tool

Objective

The dipole magnets in a circular particle accelerator are to keep the beam of particles in the circular orbit. It is obtained by achieving a highly homogeneous field in the 2D magnet cross-section. As we have seen, any practical configurations, such as the block design foreseen in our HTS insert, results in field errors due to the disagreement to the ideal $\cos\theta$ geometry. In addition, a twisted stacked cable brings several design constraints that must be taken into account at first design stage of straight part. Therefore, special optimization tool for a twisted stacked/ block-type design is established to fulfill all dimensional and physical requirements and to be as simple as possible to manufacturing reproducibly.

The objective of optimization is to obtain a good field quality of HTS insert with outer yoke using an analytical approach instead of a numerical approach, which requires multi-software implementation. However, the analytical approach is difficult to solve complicated magnet configuration. Therefore, we only consider the HTS insert in our optimization tool. The outer yoke is included after its optimization, which in any case has small difference in field quality. The optimization is developed in the Matlab[®] environment using ‘Find the minimum of constrained nonlinear multivariable function’. It delivers a minimum objective value based on the initial points of the variables under the constraints. We define the field quality as well as the operating current density J_{op} as the objective output as a function of HTS insert cross-section (variable) under dimensional and physical constraints of EuCARD2 project.

Electromagnetic equation for block design

The electromagnetic equation for a block layout is simply derived with an extension from a line current (Figure 2.1) [93]. The magnetic flux density B at point P whose distance R from the block at point Q with the current density $J \cdot dadb$ is derived from the Ampere’s Law:

$$\delta B = \mu_0 \frac{J dadb}{2\pi R} \quad (2.1a)$$

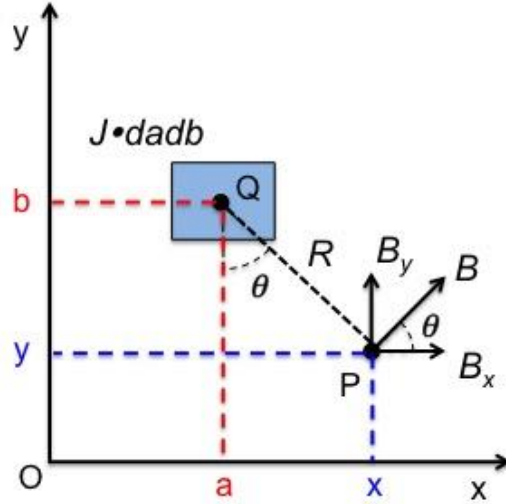


Figure 2.1 Field analysis at point P generated by a block at point Q with the current density $J \cdot da db$ in Cartesian coordinate.

$$R = \sqrt{(x - a)^2 + (y - b)^2} \quad (2.1b)$$

Where μ_0 is the relative permeability. In Cartesian coordinate, the flux density is classified into x and y components.

$$\delta B_x = \delta B \cos \theta = \delta B \frac{b - y}{R} = \mu_0 \frac{J da db}{2\pi} \frac{b - y}{R^2} \quad (2.2a)$$

$$\delta B_y = \delta B \sin \theta = \delta B \frac{x - a}{R} = \mu_0 \frac{J da db}{2\pi} \frac{x - a}{R^2} \quad (2.2b)$$

By integrating the cross-area of block along the width ($a_1 \rightarrow a_2$) and thickness ($b_1 \rightarrow b_2$), the above equations become:

$$B_x = \frac{\mu_0 J}{2\pi} \int_{a_1}^{a_2} \int_{b_1}^{b_2} \frac{b - y}{(x - a)^2 + (y - b)^2} da db \quad (2.3a)$$

$$B_y = \frac{\mu_0 J}{2\pi} \int_{a_1}^{a_2} \int_{b_1}^{b_2} \frac{x - a}{(x - a)^2 + (y - b)^2} da db \quad (2.3b)$$

The quality of magnetic field in the beam aperture can be expressed as the coefficient of the Fourier-series expansion of the cylindrical field component at a given reference radius r_0 as a function of the angular position φ .

$$B_r(r, \varphi) = \sum_{n=1}^{\infty} \left(\frac{r}{r_0}\right)^{n-1} (B_n(r_0) \sin(n\varphi) + A_n(r_0) \cos(n\varphi)) \quad (2.4a)$$

$$B_\varphi(r, \varphi) = \sum_{n=1}^{\infty} \left(\frac{r}{r_0}\right)^{n-1} (B_n(r_0) \cos(n\varphi) - A_n(r_0) \sin(n\varphi)) \quad (2.4b)$$

The B_n is called the normal and the A_n the skew components of the field given in Tesla. The field component can also be expressed from a line current I (Figure 2.2).

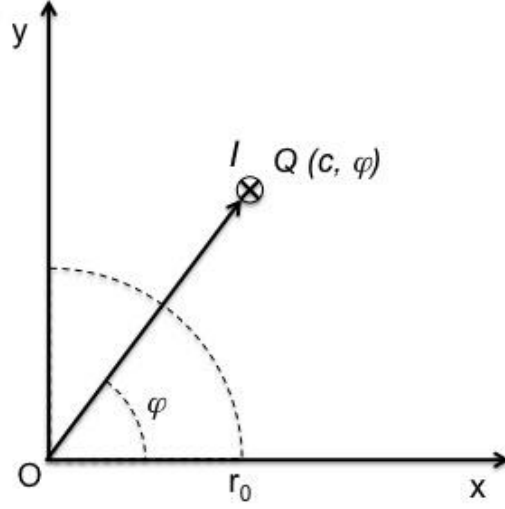


Figure 2.2 Field analysis at point P generated by a line current I at point Q .

$$B_r(r_0) = \frac{\mu_0 I}{2\pi c} \sum_{n=1}^{\infty} \left(\frac{r}{c}\right)^{n-1} \sin(n\varphi) \quad (2.5a)$$

$$B_\varphi(r_0) = \frac{\mu_0 I}{2\pi c} \sum_{n=1}^{\infty} \left(\frac{r}{c}\right)^{n-1} \cos(n\varphi) \quad (2.5b)$$

Where c is the radial position coordinate of the current.

By comparing the Eq. (2.4) and (2.5), the B_n and A_n are derived for the line current.

$$B_n(r_0) = \frac{\mu_0 I}{2\pi c} \left(\frac{r_0}{c}\right)^{n-1} \cos(n\varphi) \quad (2.6a)$$

$$A_n(r_0) = \frac{\mu_0 I}{2\pi c} \left(\frac{r_0}{c}\right)^{n-1} \sin(n\varphi) \quad (2.6b)$$

The typical field quality of accelerator magnet is that the deviation from the main field component B_N .

$$b_n = \frac{10^4 B_n(r_0)}{B_N} \quad (2.7a)$$

$$a_n = \frac{10^4 A_n(r_0)}{B_N} \quad (2.7b)$$

Where b_n and a_n are reduced component in $10^4 B_N$ units. We get $N = 1$ for dipole, $N = 2$ for quadrupole etc. When the dipole magnet has perfect symmetric design, the allowed field harmonics are only the odd number of normal component B_{2n+1} , while the other component becomes zero. The collapse in symmetric design generates other field components.

Description of optimization tool

A homemade optimization follows the prescribed dimensional and physical steps:

1. Fixed value: center field $B_l = 5$ T
2. Constraints of EuCARD2 and twisted stacked cable
3. Objective values (the field quality and operating current density J_{op}) derived from the variables (the position of block x_b and y_b)

The main objective is to obtain a 5 T standalone field with maximum field quality and minimum J_{op} as possible (Figure 2.3). All blocks N_b must have the same block size (width: w_b and thickness: t_b) based on the assumption that they are connected in series by turn-to-turn transition. The total center magnetic field is simply the sum of all contributed block with uniform J_{op} . The blocks are placed inside the 100-mm aperture FRESCA2 LTS outsert. It has to provide the geometric field quality smaller than $5 \cdot 10^{-4} B_l$ at two-third of the 40 mm beam aperture. The field quality of block is obtained by shifting the Eq. (2.6) into the Cartesian coordinate.

$$B_n(r_0) = \sum_{i=1}^{N_b} \frac{\mu_0 r_0^{n-1} J_{op}}{2\pi} \iint (x(i)^2 + y(i)^2)^{-\frac{n-1}{2}} \cdot \cos \left\{ n \cdot \tan^{-1} \left(\frac{y(i)}{x(i)} \right) \right\} dx dy \quad (2.8)$$

Where n takes the odd numbers ($n = 3, 5, 7$ etc.) in symmetrical design.

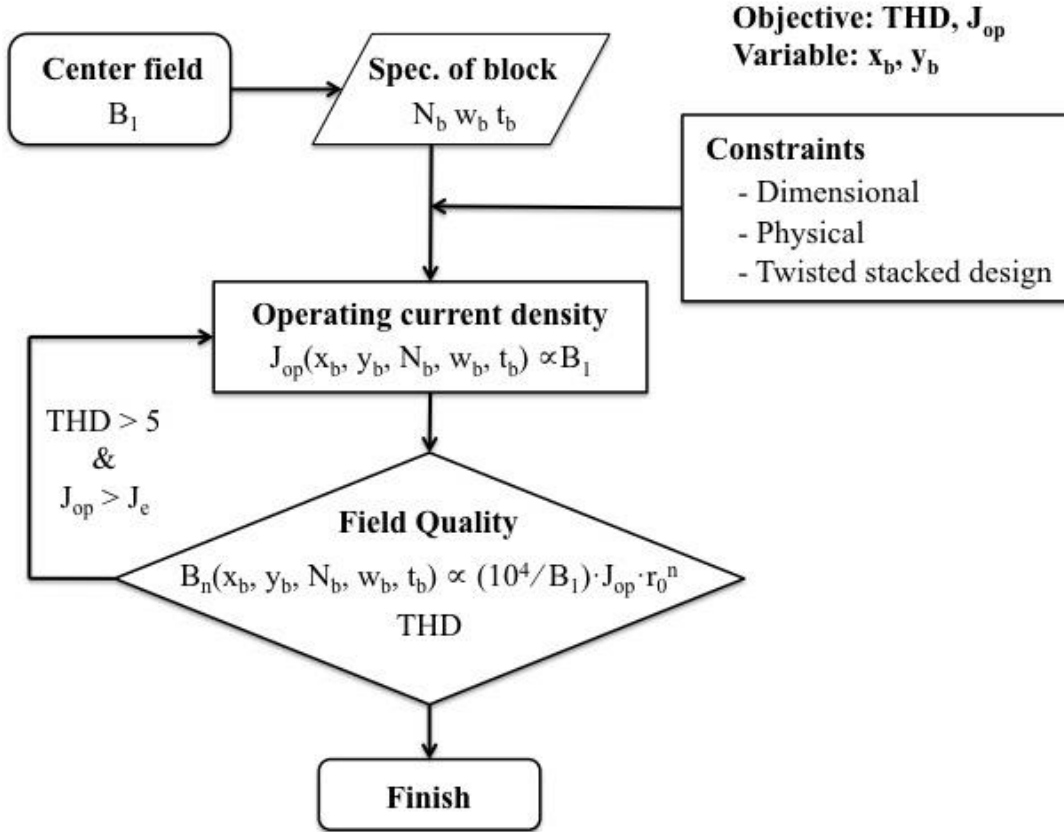


Figure 2.3 Flowchart of optimization tool of twisted stacked/block-type HTS insert. The Matlab[®] 'fmincon' provides the minimum objective value (THD and J_{op}) as a function of the variables that are the position of block.

To understand how the position of block influences the B_1 and the corresponding field harmonics B_3 , B_5 and B_7 , we put constant current density $J_{op} = 1 \text{ MA/m}^2$ into Eq. (2.3 b) and (2.8) for every possible location of HTS insert (Figure 2.4). For example, 5x5mm block in dashed line in every Figure 2.4 generates $B_1 = 0.7 \text{ mT}$, $B_3 = -6.5 \times 10^{-4}$ unit, $B_5 = 3 \times 10^{-3}$ unit and $B_7 = 8.9 \times 10^{-4}$ unit, which are the sum of each value inside the cross-area of block. These values are in proportion to J_{op} , which gets significant in case of $J_{op} > 400 \text{ MA/m}^2$. The B_1/J_{op} is called as a transfer function (TF), which becomes higher near at the perimeter of beam aperture in the midplane. Each harmonics component has different distribution pattern showing positive and negative part in turn. This means a single block placed just in-between of positive and negative parts of B_3 ($= 0$ unit) can still generate high negative component of B_5 . Therefore, plural blocks are needed to cancel all harmonics. The other harmonics more than B_9 are not necessity to consider since its amplitude from the deviation of $10^{-4}B_1$ decreases when n gets bigger. Thus, n can run to a finite number. In the optimization, it tool compares the sum of all harmonics ‘total harmonics distortion (THD)’ with required field quality instead of each individual field harmonics.

$$THD = \frac{10^4}{B_1} \sqrt{\sum_{n=1}^{n_{max}=9} B_{2n+1}^2} \quad (2.9)$$

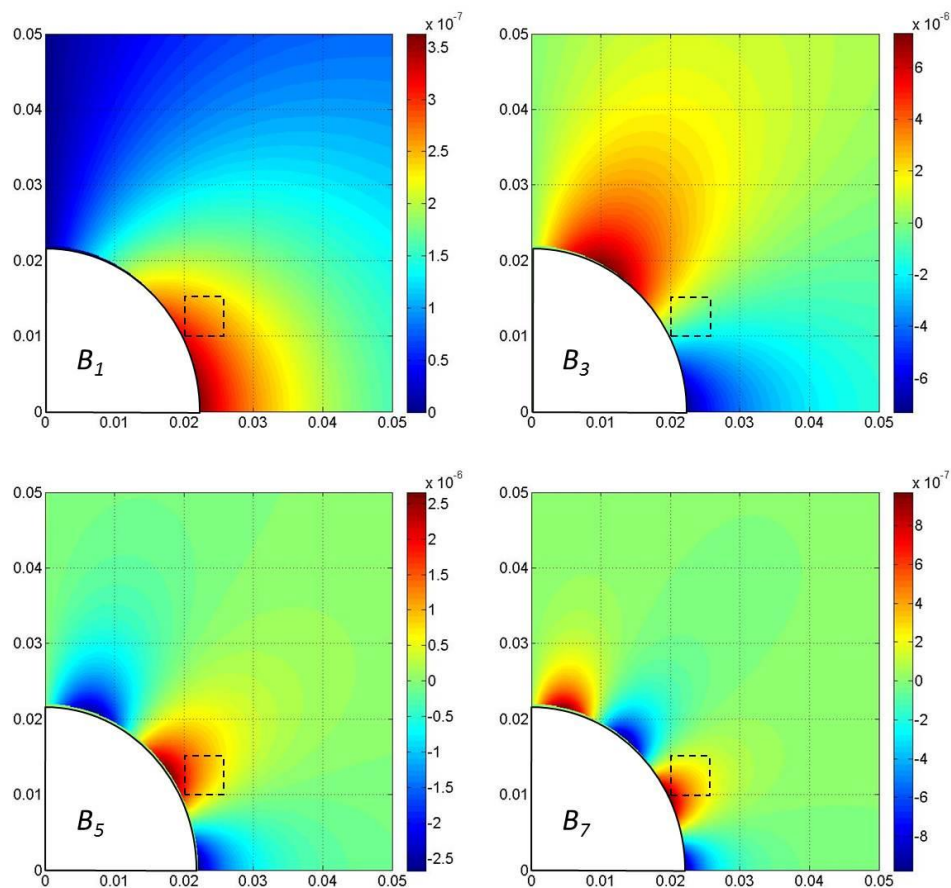


Figure 2.4 Influence of position of conductor with 1 MA/m^2 of current density on the distribution of B_1 (top-left) and the field harmonics of B_3 (top-right), B_5 (bottom-left) and B_7 (bottom-right).

General block-type HTS insert

As a preliminary step, it is important to study the general influence of the number, size and position of the blocks on both the J_{op} and field quality at the reference radius (2/3 of 40 mm). Therefore, only the EuCARD2 dimensional constraints, whose inner and outer apertures for the HTS insert region are 40 and 100mm respectively, are considered. We analyzed two extreme cases for a 5 T standalone HTS insert whose block is composed of either 4 or 12 mm wide commercially available ReBCO tape. The block is distributed so as its thickness, which is the wider surface of the ReBCO tape, is aligned vertically. This is because high vertical background field of LTS outsert is exposed to HTS insert.

Figure 2.5 shows the possible minimum THD with different block size at fixed $B_l = 5T$. It also shows the J_{op} and operating current $I_{op} (= J_{op} * w_b * t_b)$ of HTS insert design, which has possible minimum THD . For 4 mm thick block, the THD is sufficiently smaller than the required value. On the other hand, some of 12 mm thick blocks exceed the requirement. The J_{op} is almost in inverse square proportion to the conductive area $S_c (= N_b * w_b * t_b)$. The I_{op} is only dependent on the number of blocks, in other words, the number of turns. It needs more than a few dozens of turns to obtain 10 kA-class I_{op} . However, the number of turns, i.e. total conductive area, has strong impact on the cost. One has to know both J_{op} and I_{op} can be reduced by outer yoke of FRESCA 2, which is about 15%.

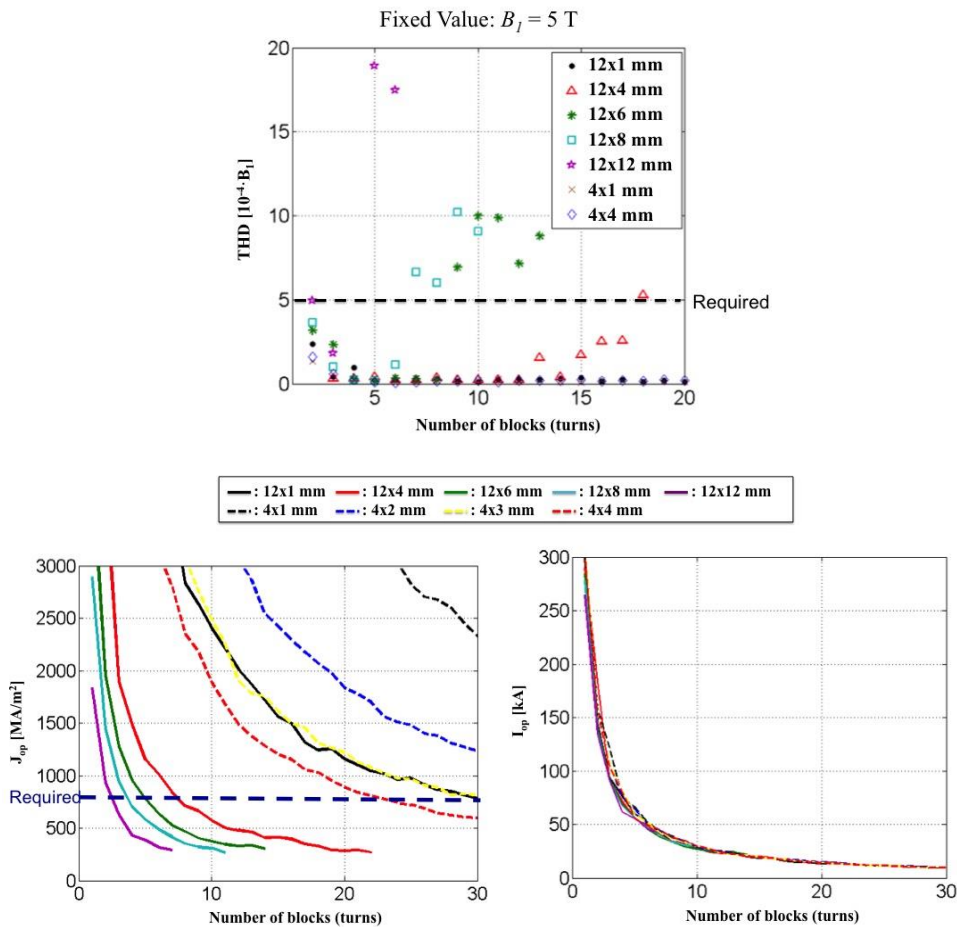


Figure 2.5 Block-type HTS insert: Influence of the number and size (width and thickness) of block composing a 4 or 12 mm wide ReBCO tape on THD , J_{op} and I_{op} under the EuCARD2 dimensional constraints.

Figure 2.6 shows one of the optimized HTS insert designs using 15-turn of 4x4 mm block. This design gives $THD = 0.2$ units, $J_{op} = 1203 \text{ MA/m}^2$ and $I_{op} = 19 \text{ kA}$. Though all blocks are distributed randomly, they are aiming to represent the ideal $\cos\theta$ geometry. However, it is not feasible from a manufacturing point of view. Therefore, the blocks are needed to reposition to examine more feasible cross-section. In principle, the optimized insert design can rearrange its cross-section towards feasible manufacturability, whose THD is still below the required value.

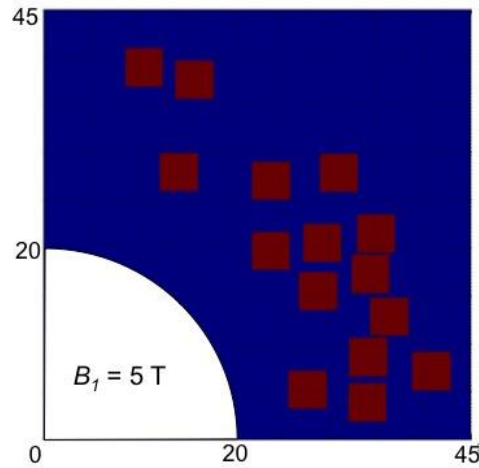


Figure 2.6 Optimized 5 T HTS insert design using 15-turn of 4x4 mm block.

The mechanical design is one important aspect for high accelerator performance that should be taken into account at first design stage. The HTS insert will experience the thermal stress and large Lorentz forces during normal operation. The displacement of conductor has to be avoided and the mechanical deformation must be minimized to keep the designed field quality. Since Lorentz forces are directed outwards where the external mechanical tubes are reinforced, one can estimate its overall stress.

$$\text{Total Lorentz force: } F = N_b \times I_{op} \times B_{av} \times l \quad [N] \quad (2.10a)$$

$$\text{Overall stress: } \sigma_{\theta} = \frac{F}{2\pi t_{tube} l} = \frac{N_b \times I_{op} \times B_{av}}{2\pi t_{tube}} \quad [Pa] \quad (2.10b)$$

Where B_{av} is the average magnetic field of all HTS insert regions, l is the magnet length and t_{tube} is the thickness of the external mechanical tube. The objective is to keep the overall stress below the allowable stress of external tube. In principle, t_{tube} is the only factor that can reduce the overall stress.

Here, we assume that the HTS insert exposed into high background field is reinforced by an external tube, which are $B_{av} = 18 \text{ T}$, $l = 15 \text{ m}$ and $t_{tube} = 5 \text{ mm}$. In most cases, the optimized insert designs using 4 and 12 mm thick blocks in Figure 2.5 shows the overall stress within the range of 600 – 700 MPa. These values can be reduced by the outer yoke.

As a consequence of the evaluation for the block-type HTS insert, the best design is to use a dozen of 12x2 mm or 12x4 mm blocks. This is because it can achieve the required field quality with high B_1/J_{op} . Figure 2.7 shows one of the best-optimized designs that are a 16-turn HTS insert using 12x4 mm blocks. Every two or three turns are aligned horizontally and they are assembled into six layers. This facilitates the winding and the mechanical structure. The HTS insert generates well uniform magnetic field of 5 T with 707 A/mm² in a standalone mode and of 17.1 T with 620A/mm² in the background field. The outer yoke contributes the field enhancement for 14%. Owing to the vertical background field, all Lorentz forces are directed towards the external mechanical tube.

Table 2.1
Block-type HTS insert specification

| Parameter | Value (Standalone/ magnetic shield) |
|-------------------------------------|-------------------------------------|
| Number of turns | 16-turn |
| Size of block | 12x4 mm ² |
| Conductive area | 1536 mm ² |
| Minimum bending radius | 9.6 mm |
| Center field | 5/ 17.1 T |
| Operating current density | 707/ 620 MA/m ² |
| Operating current | 34/ 29 kA |
| Field quality THD in $10^{-4}B_1$ | 2.66/ 7.88 unit |
| Total inductance per unit length | 0.048 mH |

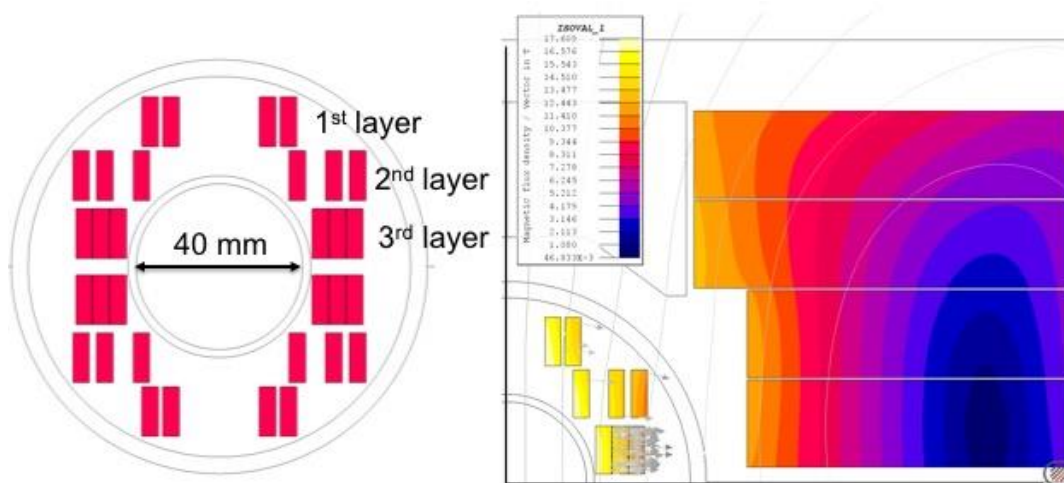


Figure 2.7 16-turn HTS insert using a 12x4 mm block (left). A 17 T of background field is exposed to HTS insert and the Lorentz forces are directed towards the external mechanical tube (right).

2.1.2. Dimensional and physical constraints for twisted stacked cable

General EuCARD2 physical constraints

As we have mentioned, a 5 T HTS insert operates inside the 100 mm aperture of the FRESCA2 LTS outsert with outer iron yoke. Both magnets aim to provide 17 - 20 T range of field inside the 40 mm beam aperture with good geometric field quality $< 5 \cdot 10^{-4} B_I$ at the reference radius ($r_0 = 13.3$ mm). The superconducting accelerator magnets also have to take into account for field harmonics due to the magnetization/screening current. Thus, the field quality including magnetization-induced harmonics is set to be smaller than $50 \cdot 10^{-4} B_I$. The magnets must have high reliability under normal operation and should be protected in fault mode. One of the key parameters is the contribution ratio for center field B_I / J_{op} and the operating current I_{op} . The B_I / J_{op} is required to be as high as possible, which means it can produce $B_I = 5$ T with smallest J_{op} . In addition, a small J_{op} assists the safe operation gaining more operational margin to the engineering current density J_e . The final targets of the J_e at 4.2 K and under transverse magnetic field are 600 A/mm² at 20 T, 675 A/mm² at 15 T and 750 A/mm² at 12 T, although the present performance of the commercially available ReBCO tape at 4.2 K reaches 2000 A/mm² in parallel and 450 A/mm² in transverse under 20 T, at best. The large I_{op} in the range of 5 - 10 kA is also to ensure the safe operation in case of the fault such as a hot spot. It prevents the magnet to permanent damage.

The HTS insert must minimize the mechanical deformation caused by the thermal stress during cool-down and the Lorentz forces during normal operation; otherwise it may initiate the quench and collapse the designed geometric field quality. An internal and external mechanical tube, therefore, are employed to counteract these forces. They are placed in the HTS insert region and must not break into either the beam aperture or LTS outsert. Therefore, one must put some space between external tube and LTS outsert that is about 0.5 mm. A field alignment of the ReBCO stacked tape makes the best use of its superconducting properties in the J_e and mechanics. It also brings other interests that are the magnetization (Chapter 3) and the AC losses.

Table 2.2
HTS insert constraints in EuCARD2 project

| Parameter | Symbol | Value |
|--|--------------|--------------------------|
| Dimensional constraints | | |
| Beam aperture | ϕ_b | 40 mm |
| Magnet outer aperture | ϕ_{ext} | < 99 mm |
| Electromagnetic constraints | | |
| Center field in standalone | B_I | 5 T |
| Center field with LTS outsert | – | 17 – 20 T |
| Operating current | I_{op} | 5 – 10 kA |
| Field quality at 2/3 ϕ_b (Geometric) | B_n | $< 5 \cdot 10^{-4} B_I$ |
| Field quality at 2/3 ϕ_b (including magnetization and persistent current) | B_n | $< 50 \cdot 10^{-4} B_I$ |

Table 2.3
Target of ReBCO tape in EuCARD2 project

| Parameter | Symbol | Value |
|--|--------------------|-----------------------|
| Target of engineering current density at 4.2 K and transverse magnetic field | $J_e(12\text{ T})$ | 750 MA/m ² |
| | $J_e(15\text{ T})$ | 675 MA/m ² |
| | $J_e(20\text{ T})$ | 600 MA/m ² |

Twisted stacked/ block-type constraints

A twisted stacked/ block-type HTS insert has the twist to equalize the electromagnetic conditions of the tapes in the stacked cable, which is expected to meet cable's requirements: low magnetization and uniform current distribution. However, the magnetic field is likely to penetrate into the bad orientation of the ReBCO tape where the engineering current density gets lower (Figure 2.8). For example, the ReBCO tape aligned to the background field at straight part rotates its cross-section during the twist, which causes the penetration of transverse field at 90° angled cross-section. To obtain large J_e as possible, the twist is only applied in magnet ends where the field amplitude of LTS outsert gets smaller. The continuous twist transposition is thus not appropriate for the twisted stacked/ block-type HTS insert. Now, to achieve the transposed magnet, a half twist is at least required in magnet ends; even though the transposed magnets are usually composed of many transpositions to answer the cable's requirements. Therefore, we need to know the electromagnetic behavior with such a long twist transposition pitch. The magnet ends will not anyhow have good field quality, so it must be as short as possible. Besides, it is preferred to avoid the hardway bending, which results in far too long magnet ends compared to the easyway bending. The twist in the magnet ends enables a very sharp winding head of the flared-end coil [83]. This can shorten the magnet ends.

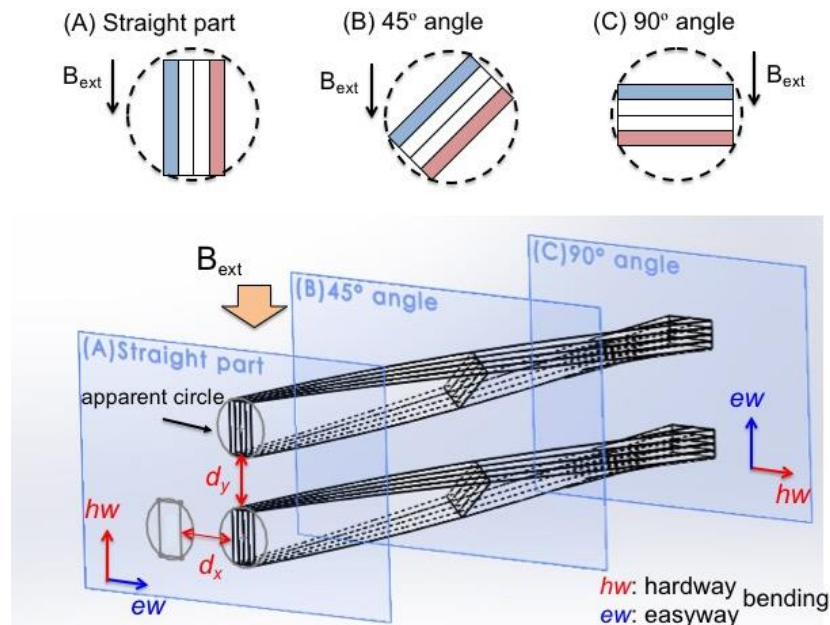


Figure 2.8 Schematic view of the HTS twisted stacked cable with an apparent circle from straight part to 90° angles.

While twisting the stacked cable, its cross-section rotates along its longitudinal direction. This reveals an apparent circle from an x - y view orientation in Figure 2.8. This will risk the stacked cables overlapping each other when they are located too close before the twist. Hence, the space between the stacked cables in horizontal d_x and in vertical d_y at straight part must be carefully taken into account already at first design stage; otherwise the stacked cable is needed to reposition before the twist in magnet ends (Figure 2.9).

- $d_x \geq 2r_T - w_b$, $d_y \geq 2r_T - t_b$: No reposition before twist in magnet ends.
- $d_x < 2r_T - w_b$: Reposition in easyway bending.
- $d_y < 2r_T - t_b$: Reposition in hardway bending.

Where $2r_T - w_b$ and $2r_T - t_b$ are the distance between stacked cables when two apparent circles are touching each other. When all stacked cables have sufficient space, they can be twisted at the same time without any reposition, which brings shortest magnet ends. On the contrary, insufficient space in vertical ($d_y < 2r_T - t_b$) can result in complicated and long magnet ends because the cables are needed to reposition in hardway bending. Therefore, one must at least keep sufficient vertical space.

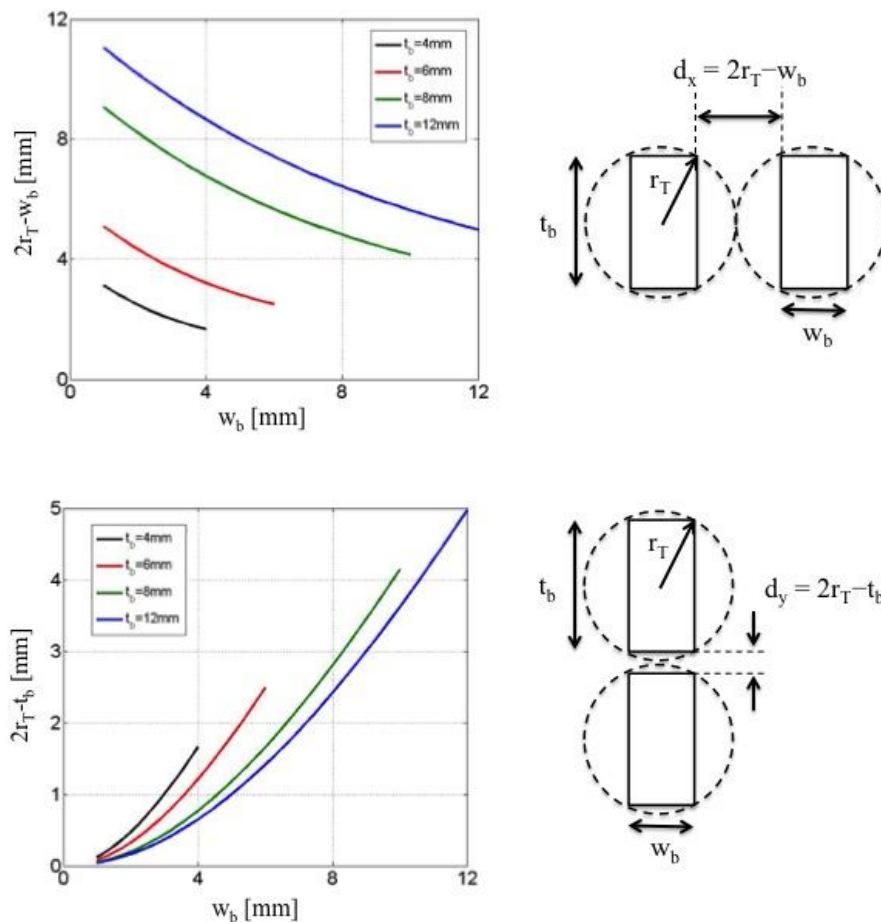


Figure 2.9 Minimum required space between the stacked cables during the twist in magnet ends in horizontal (top) and in vertical (bottom).

The overall engineering current density over the occupied cross-area of the twisted stacked cable $J_{e,T}$ is:

$$J_{e,T} = \frac{w_b t_b}{\pi r_T^2} J_e \quad (2.11)$$

The $J_{e,T}/J_e$ becomes the maximum in case of a square block ($w_b = t_b$) (Figure 2.10). In conclusion, the twisted stacked/ block-type design has to deal with:

- Design compatibility for the field quality at straight part and the architecture in magnet end
- High overall engineering current density $J_{e,T}/J_e$

For this reason, the square block composed of 4 or 6 mm width ReBCO tape becomes the best solution.

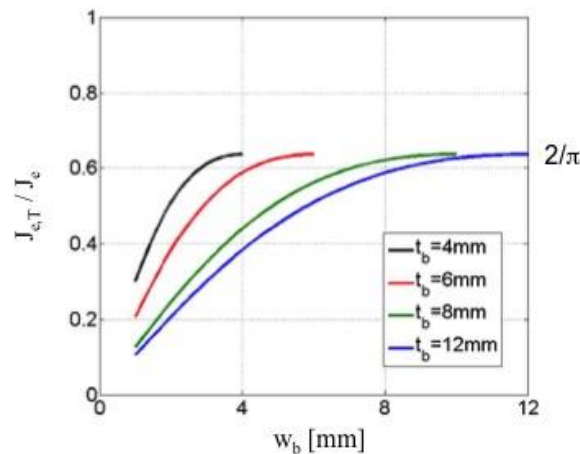


Figure 2.10 Overall engineering current density over the cross-area of the twist.

Manufacturing constraints

The large circumference of the LHC and the large number of the superconducting magnets make vitally important to simplify the 2D cross-section of magnet from a manufacturing point of view. In most of the dipole magnets, they are wound into several turns of single or double pancake coil (Figure 2.11). In case of the block layout magnet, several stacked cables are aligned in horizontal as shown in Figure 2.7. They are connected in series by turn-to-turn transition from inner to outer turn. From a structural point of view, the single pancake coil has an electrical inlet and outlet at the innermost and outermost turns; whereas those of double pancake coil only appear at the outermost turns of each pancake coil at top and bottom. Concerning the single pancake coil, the inlet at the innermost turn has to pass over the winding head to reach the electrical joint at the dipole extremity. Two single pancake coils belonging to the same double pancake coil are connected with a layer jump transition (green color). The layer jump of the dipole magnet is preferably located in magnet ends in order not to disturb the field quality at straight part.

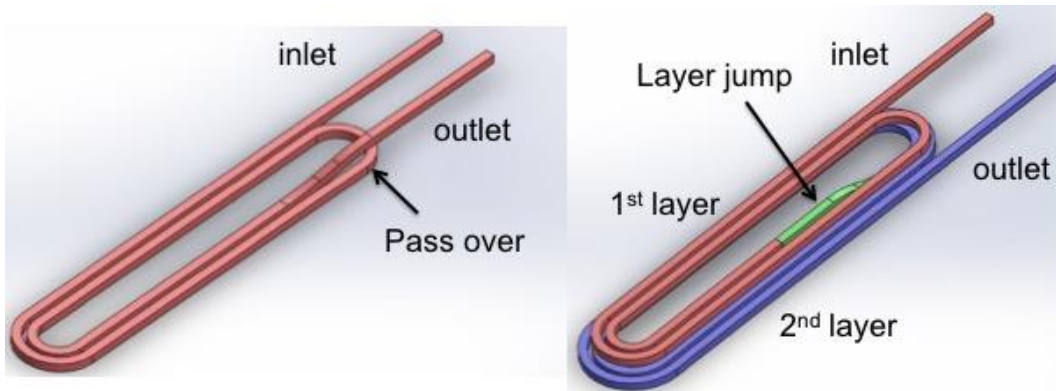


Figure 2.11 Single pancake coil (left) and double pancake coil connected with the layer jump transition (right).

2.1.3. Magnet cross-section at straight part

According to the unique constraints for the twisted stacked/ block-type HTS insert, we study the influence of the number, size and position of the block based on the general block-type HTS insert. The best block-type HTS insert design using a 12x4mm block satisfies enough operation margins and easy manufacturing. However, it is not adequate in case for twisted stacked/ block-type design in regard to the magnet end architecture and overall engineering current density $J_{e,T}/J_e (= 0.38)$. The twisted apparent circles are overlapped at straight part, which requires the repositions in easyway bending (Figure 2.12). However, due to the space limitation, it is not possible to reposition all the cables. Thus, it causes the complicated and long magnet ends. We thus only consider a square block composed of a 4 mm wide ReBCO tape.

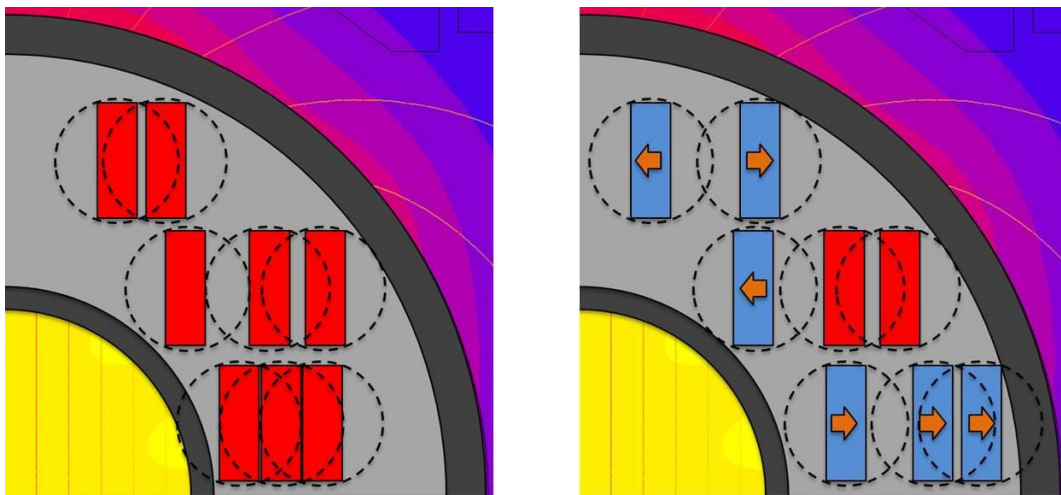


Figure 2.12 16-turn HTS insert using a 12x4 mm block with an apparent circle (left) and after the reposition in easyway bending (right). Both cases show the circles are overlapped, which is not possible to twist at same time.

The study of a general block-type HTS insert indicates that more than 1350 mm² of conductive area with 15 blocks reaches the requirements of the EuCARD2 that are 700 MA/m² of operating current density and 10 kA-class operating current. Applying this to a 4x4 mm square block design, we obtained one candidate (Figure 2.13). A 46-turn HTS insert generates a 5 T of uniform magnetic fields with 710 A/mm² of operating current density in a standalone mode without external magnetic shield. Then, it provides a 17.2 T central field in case with the Fresca2 LTS outsert and the outer yoke. This generates the field errors $B_3 = 8$ units and $B_5 = 0.27$ units and decreases the J_{op} up to 650 MA/m². The field quality is slightly higher than the required value ($< 5 \cdot 10^{-4} B_I$) due to the yoke saturation. It is possible to reduce by optimizing the yoke configuration. Three or four blocks, which are assembled and aligned horizontally, facilitates the design of the mechanical structure and the winding. They are connected in series from inner to outer turn by turn-to-turn transitions. It gives twelve pancake coils in total. Every pancake coil has enough vertical spaces larger than 1.4 mm. It is to save the space for the mechanical reinforcement at straight part and for the apparent circle during the twist in magnet ends. Most of the blocks are almost aligned to the background magnetic field. It is to make best use of the J_e of ReBCO tapes. Moreover, it helps to direct the Lorentz forces onto the flat surface of the tape. However, the outer turns of three top pancake coils have small field angle about 14° with a 13 T, which can drastically lower the J_e (§1.3.2.2, Figure 1.18). For this reason, the blocks will be tilted later to align perfectly. It also helps to bring about the same J_e to all tapes in the stacked cable because of the small variation in field amplitude between the tapes in the stacked cable. The maximum magnetic field B_{max} occurs at two top innermost turns where the field is enhanced with the iron pole of FRESKA2. The B_{max} is 17.6 T in parallel to the wide surface of the tape. The Lorentz forces are directed towards the LTS outsert. In addition, thermal contraction will push towards the beam tube. Therefore, 2 mm thick internal and 4 mm thick external mechanical tubes are employed to withstand the forces.

Table 2.4
Twisted stacked/ Block-type HTS insert specifications

| Parameter | Value (Standalone/ magnetic shield) |
|--------------------------------------|-------------------------------------|
| Number of turns | 46-turn |
| Size of block | 4x4 mm ² |
| Conductive area | 1472 mm ² |
| Minimum bending radius | 9.75 mm |
| Center field | 5/ 17.1 T |
| Operating current density | 710/ 650 MA/m ² |
| Operating current | 11.36/ 10.4 kA |
| Field quality THD in $10^{-4} B_I$ | 2.09/ 8.01 unit |
| Total inductance per unit length | 0.42 mH |

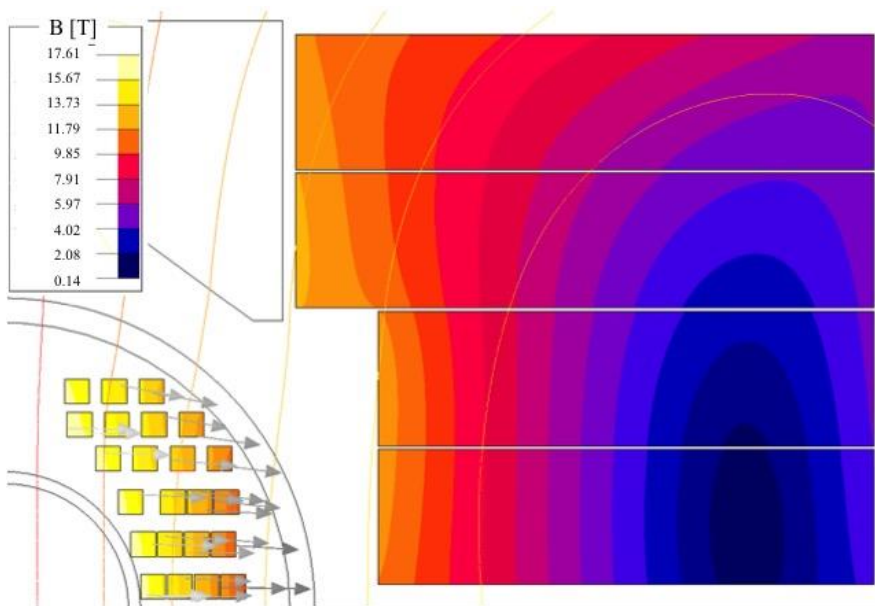
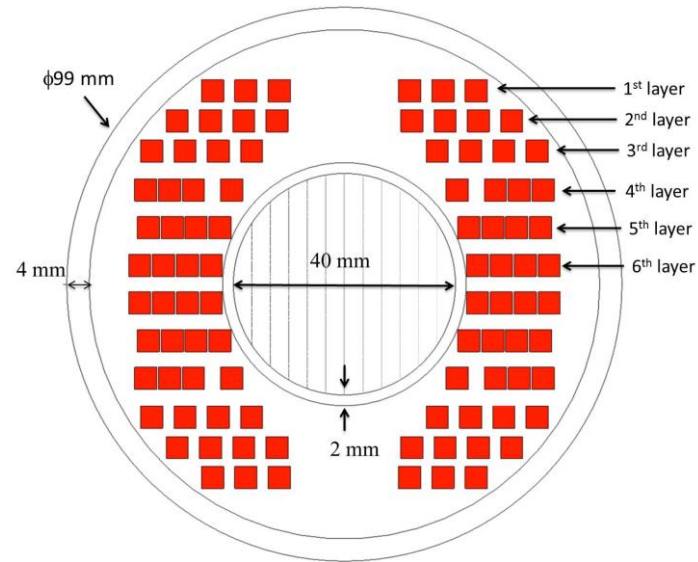


Figure 2.13 46-turn HTS insert using a 4x4 mm square block (top). A 17 T of background field is exposed to HTS insert and the Lorentz forces are directed towards the external mechanical tube (bottom).

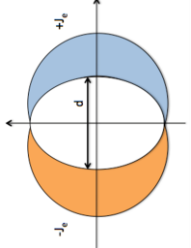
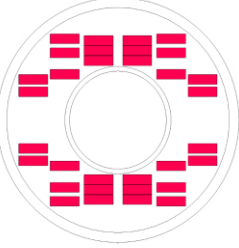
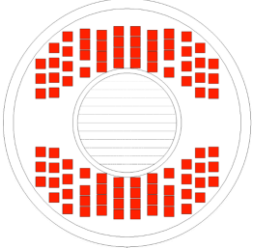
| Parameter name | Ideal Dipole | 16-turn block-type insert | 46-turn twisted stacked/block-type insert |
|---------------------------------------|---|--|---|
| Coil Layout | | | |
| |  |  |  |
| General | | | |
| Beam aperture | 40 mm | 40 mm + 2 mm spacing | 40 mm + 2 mm spacing |
| Block size | - | 12x4 mm | 4x4 mm |
| Minimum bending radius | - | 9.6 mm | 9.75 mm |
| Conductive area | - | 1536 mm ² | 1472 mm ² |
| Manufacturability | - | Complicated and long twisted magnet ends | Simple twisted magnet ends |
| Standalone | | | |
| Center field B_1 | 5 T | 5 T | 5 T |
| Current density J_{op} | 298 MA/m ² | 707 MA/m ² | 710 MA/m ² |
| Operating current I_{op} | - | 34 kA | 11.36 kA |
| Total inductance of 15 m long | - | 0.048 mH | 0.42 mH |
| Field quality THD ($10^{-4} B_1$) | - | 2.66 units | 2.09 units |
| Hexapole B_3 | - | -2.63 units | -0.93 units |
| Decapole B_5 | - | -0.18 units | 0.86 units |
| Tetradecapole B_7 | - | -0.37 units | -1.3 units |
| In background field | | | |
| Center field | - | 17.1 T | 17.2 T |
| Current density | - | 620 MA/m ² | 650 MA/m ² |
| Operating current I_{op} | - | 29 kA | 10.4 kA |
| Maximum field angle | - | 15°/13.2 T | 14°/13 T |
| Field quality THD ($10^{-4} B_1$) | - | 7.88 units | 8.01 units |
| Hexapole B_3 | - | 7.76 units | 8 units |
| Decapole B_5 | - | -0.54 units | -0.27 units |
| Tetradecapole B_7 | - | -0.09 units | -0.42 units |

Figure 2.14 Comparison of the ideal dipole, block-type and twisted stacked block-type HTS insert.

2.2. 3D magnet ends

2.2.1. Structure of twisted stacked cable

In the 46-turn HTS insert, the 4x4 mm block is stacked with more than twenty ReBCO tapes carrying a total operating current of 10.4 kA. All tapes are insulated each other. It is expected to cancel the defects of a very long transposition pitch, which can cause high magnetization and inhomogeneous current distribution (see Chapter 3).

A winding of dipole magnet using the twisted stacked cable consists of the easyway and hardway bending and the twist. From a structural point of view, the practical minimum bending radius and twist pitch of the stacked cable will be different from that of a single tape, although the mechanical strains are kept below the critical threshold. We test these structural limits with a dummy copper beryllium stacked cable, which has almost the same mechanical flexibility and hardness as actual ReBCO tape for the EuCARD2 HTS insert (Figure 2.15). Thirty-two of 4 mm wide and 0.13 mm thick CuBe tapes are bundled on top of one another without any additional material in-between. All tapes are free to slide each other so as to avoid one of the tapes to ripple during the winding. Therefore, the solid cabling techniques such as an impregnation would be preferred after the magnet is assembled. The evaluations of the structural limits are carried out by practice. The bending becomes difficult as the number of stacked tapes increases, whereas the twist is principally the same as the single tape owing to the ability to slide. Moreover, the ripple can easily vanish. As a consequence, the easyway r_{ew} and hardway r_{hw} bending radius and twist pitch length L_P are 9 mm, 2m and 200 mm for 360° twist ($T_P = 1.8$ °/mm), without any mechanical deformation. They are indeed below the critical strain of the ReBCO tape.

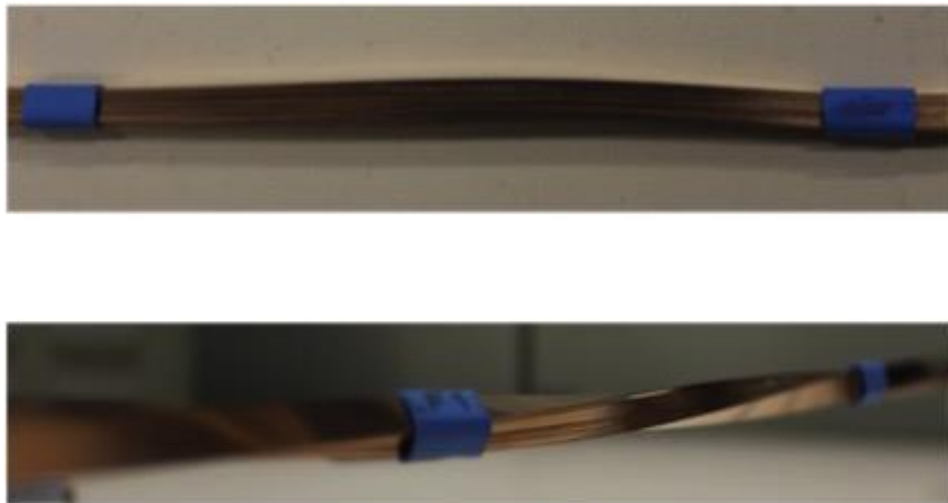


Figure 2.15 Thirty-two of 4 mm wide dummy CuBe stacked cable (top) and is twisted continuously with 1.8°/mm of twist pitch length L_P (bottom).

2.2.2. Winding strategy

A dipole magnet is a long magnet containing a long straight part and two magnet ends. It is wound in a shape of either a racetrack flat or a flared-end coil depending on the vertical position between the stacked cable and the beam aperture. The magnet ends especially the flared-end coil using the ReBCO stacked cable definitely become complicated due to the hardway bending. Therefore, we applied a sharp winding head to find the shortest transposed magnet ends.

2.2.2.1. Racetrack flat coil

A racetrack flat coil, whose vertical position is higher than the beam aperture, has very simple winding structure. It brings the shortest and the simplest dipole magnets ends. In a multi-turn coil, the magnet ends can be divided into the transposition and turn-to-turn transition sides with straight part in-between (Figure 2.16). At the transposition side, the continuous 180° twist per turn is applied on one side. It partially transposes every turn between right and left sides. At the turn-to-turn transition side, when the stacked cable shifts from one (inner) to another (outer) turn, the transposition is not required (see Chapter 3). Thus, there is only a winding head. A total length of racetrack flat coil L_{coil} is the sum of straight part L_s , transposition side L_{trans} and turn-to-turn transition side L_{t-t} :

$$L_{coil} = L_s + L_{trans} + L_{t-t} \quad (2.12a)$$

$$= L_s + L_p/2 + r_{wind,1} + r_{wind,2} \quad (2.12b)$$

Where $r_{wind,1}$ and $r_{wind,2}$ are the mean radius of winding head at transposition and turn-to-turn transition sides, respectively. It is important to know a total length of the stacked cable per turn L_{cable} to wind the coil.

$$L_{cable} = 2L_s + L_p/2 + \pi(r_{wind,1} + r_{wind,2}) \quad (2.13)$$

By multiplying with the number of the tapes N_{tape} in the stacked cable, it derives the total needs of the ReBCO tape L_{tape} .

$$L_{tape} = N_{tape}L_{cable} \quad (2.14)$$

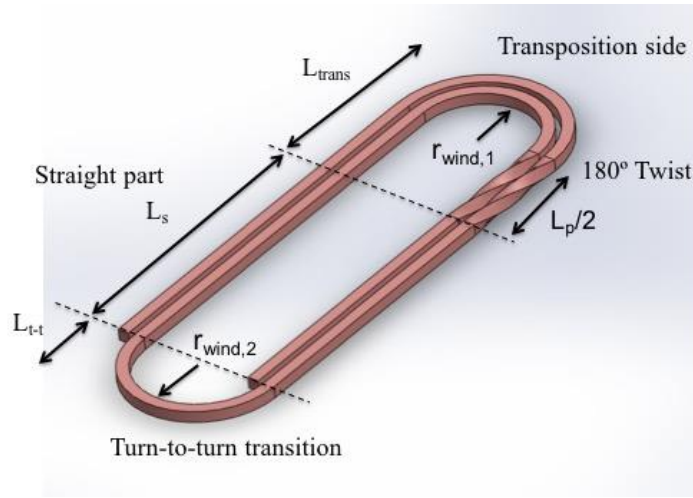


Figure 2.16 Multi-turn racetrack flat coil composed of 180° twist per turn at transposition side and turn-to-turn transition.

2.2.2.2. Flared-end coil

A flared-end coil, whose vertical position is lower than the beam aperture, has to lift its vertical position above the beam aperture toward the winding head. In addition, the twist has to be applied at the same time. In general, the stacked cable in block-type HTS insert is bended in hardway bending to raise its position. This results in long magnet ends. A sharp winding head using 180° twist is expected to be the appropriate winding method to avoid long magnet ends (Figure 2.17). The sharp winding head consists of the 180° twist, which can be divided into two 90° twists with the easyway bending in-between. The first 90° twist rotates the cross-section into the easyway bending to raise the conductor above the beam tube. It facilitates to tilt and lift the stacked cable with the following easyway bending towards the winding head. Then, the second 90° twist is applied during the lifting before it reaches above the beam aperture in the winding head. It is important to avoid the bending and the twist at the same time in order not to put too much mechanical stress.

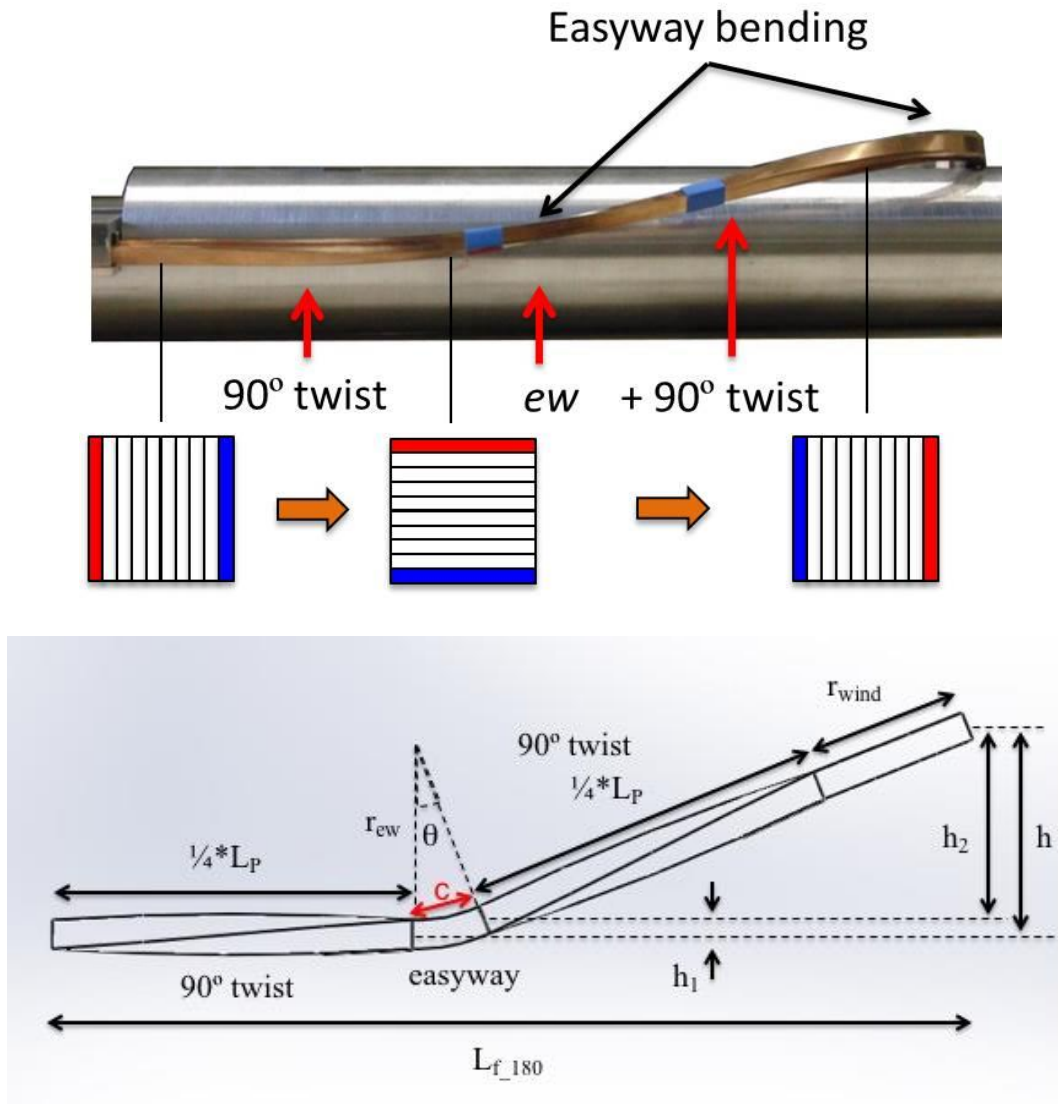


Figure 2.17 Sharp winding head using two 90° twists and easyway bending in-between (top). And its schematic view with key parameters (bottom).

A total length of winding head in flared-end coil using 180° twist L_{f_180} is:

$$h_1 = \frac{r_{ew}}{c + r_{wind} + L_P/4} h \quad (2.15a)$$

$$h_2 = \frac{r_{wind} + L_P/4}{c + r_{wind} + L_P/4} h \quad (2.15b)$$

$$L_{f_180} = L_P/4 + \sqrt{r_{ew}^2 - (r_{ew} - h_1)^2} + \sqrt{\left(L_P/4 + r_{wind}\right)^2 - h_2^2} \quad (2.15c)$$

Where h is the total lifted height, which is the summation of h_1 while the easyway bending and h_2 while the second 90° twist plus the winding head. The θ and c are the tilted angle and the length of intercept at the easyway bending. Besides, c can be derived from θ .

$$c(\theta) = r_{ew} \sin \theta(h) \quad (2.16)$$

In principle, when the vertical position of the winding head h is determined, all the other parameters can be derived.

At opposite side of 180° twisted winding head, two different winding options are proposed: 1) 360° twisted winding head and 2) conventional winding head using hardway bending (Figure 2.18). In former case, it basically has the same structure as that of 180° twist except it has 270° twist instead of first 90° twist. This is to achieve the partially transposed magnet. Thus, a total length L_{f_360} :

$$L_{f_360} = \frac{3}{4}L_P + \sqrt{r_{ew}^2 - (r_{ew} - h_1)^2} + \sqrt{\left(L_P/4 + r_{wind}\right)^2 - h_2^2} \quad (2.17)$$

Since 180° + 360° twisted winding heads forms the half U-turn coil in magnet ends, their total lengths need to be the same although it is $L_{f_180} < L_{f_360}$. Hence, one has to add another $L_P/2$ of straight part or apply bigger transposition pitch $T_P' = 3T_P$ ($= 5.4$ °/mm) at first 90° twist in 180° twist side, which brings $L_{f_180} = L_{f_360}$. On the other hand, the hardway bending side is simply to raise the stacked cable from straight part to winding point.

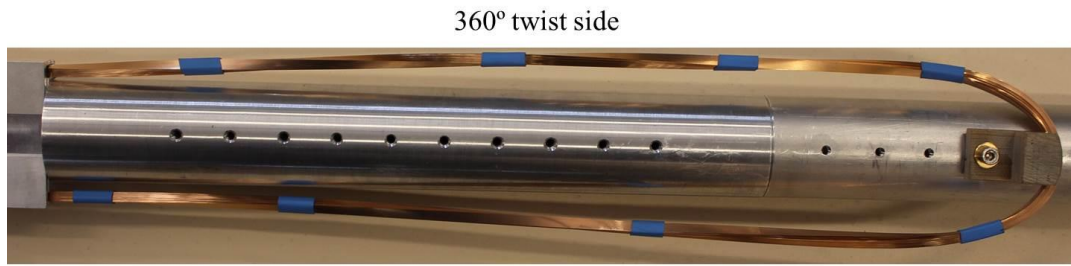
$$L_{hw} = \sqrt{r_{hw}^2 - (r_{hw} - h)^2} \quad (2.18)$$

The total cable unit length used in a half U-turn flared-end coil for 180° + 360° twisted winding heads L_{c_f360} and 180° twist + hardway bending winding heads L_{c_hw} are:

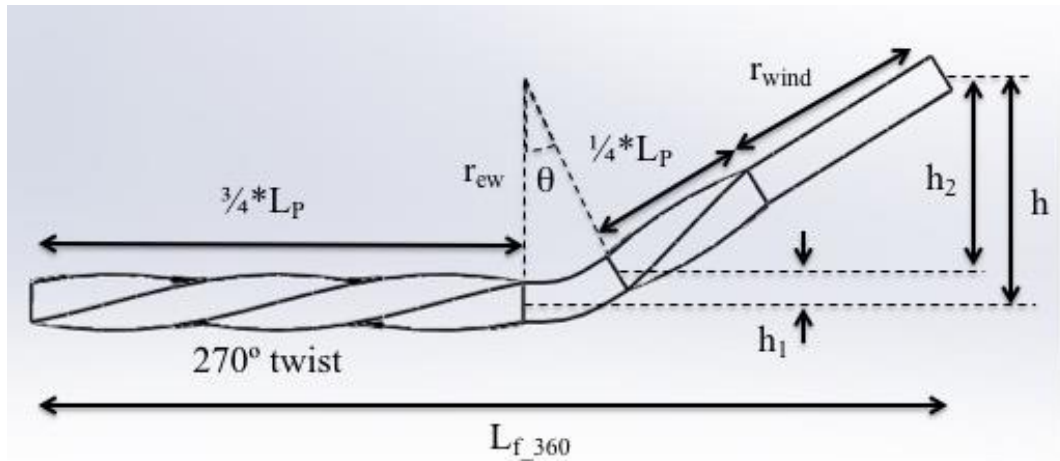
$$L_{c_f360} = 2 \left(L_P + \frac{\pi}{2} r_{wind} + r_{ew} \theta \right) \quad (2.19a)$$

$$L_{c_hw} = 2 \left(\frac{\pi}{2} r_{wind} + r_{hw} \theta_{hw} \right) \quad (2.19b)$$

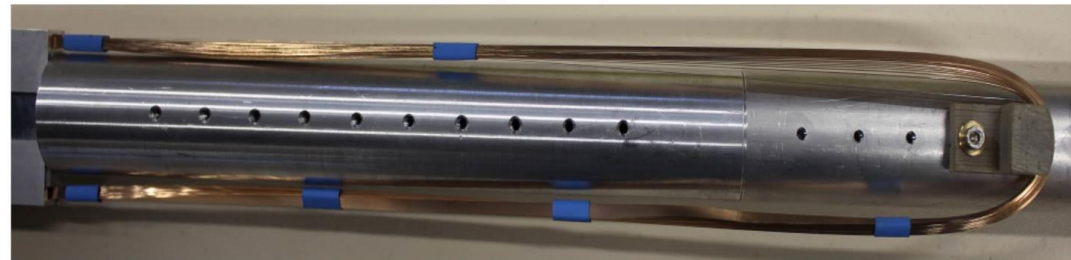
The total needs of the tape are then simply multiplied these equations by N_{tape} .



180° twist side



Hardway bending side



180° twist side

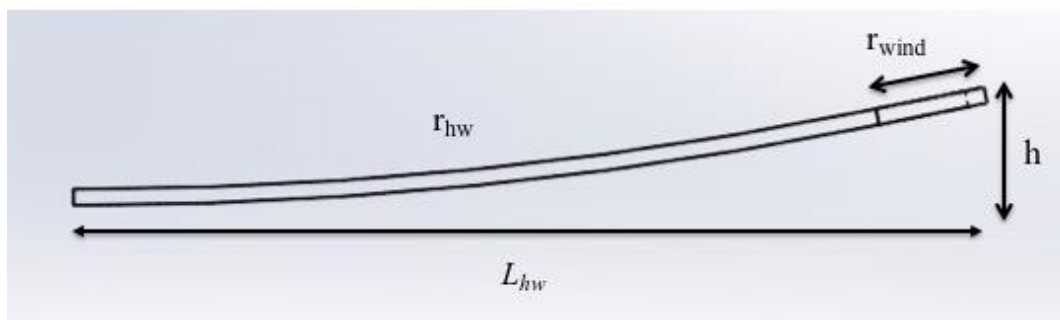


Figure 2.18 A half U-turn coil in magnet ends composed of 180° + 360° twist sides (top) and 180° twist + hardway bending sides (bottom).

Now, when easyway bending $r_{ew} = 9$ mm, hardway bending $r_{hw} = 2$ m and transposition pitch length $L_P = 200$ mm for 360° ($T_P = 1.8$ °/mm), we can compare $L_{f_{360}}$ and L_{hw} as a function of lifted height h (Figure 2.19). One can see $L_{f_{360}}$ is almost constant while L_{hw} increases in proportion to h . Furthermore, when h is higher than 12 mm, the $180^\circ + 360^\circ$ twisted winding heads bring shorter magnet ends.

In Figure 2.18, both magnet ends are 400 mm long at $h = r_{wind} = 20$ mm. From a structural point of view, the $180^\circ + 360^\circ$ twisted winding heads still have enough flexibility (less mechanical tension on the stacked cable). It can shorten the magnet ends up to 220 mm. In the meanwhile, there is already high mechanical tension on the hardway bending side, although it can shorten up to 280 mm and be a feasible option.

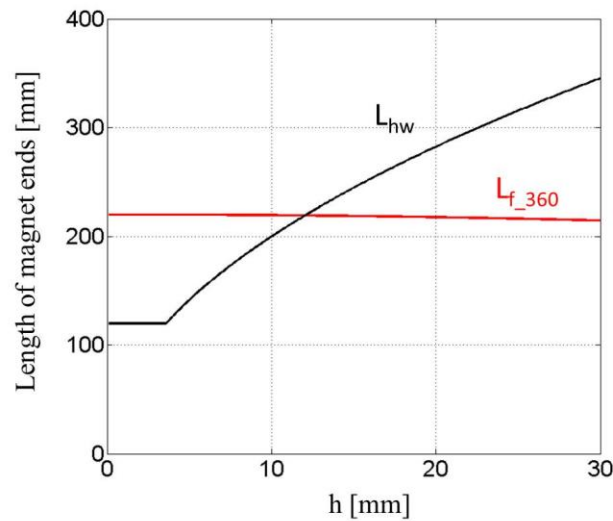


Figure 2.19 Length of a half U-turn coil in magnet ends forming (1) $180^\circ + 360^\circ$ twist sides and (2) 180° twist + hardway bending sides.

2.2.2.3. Layer jump

In a double pancake coil, two single pancakes are connected with a layer jump at innermost turns. For the general block-type HTS insert using the ReBCO stacked cable, the layer jump is done with the hardway bending in a gentle slope, which results in long length.

A twist at the layer jump may shorten the length of the jump. The combination of two 90° twists and the easyway bending in-between, which is used for the sharp winding head in the flared-end coil, transits sharply and quickly from one to another. Figure 2.20 shows the comparison of the layer jump using the hardway bending and using two 90° twists plus easyway bending in-between. The total length of the layer jump with the hardway bending L_{hw} and with two 90° twists and easyway bending in-between L_{twist} are:

$$L_{hw} = 2 \sqrt{r_{hw}^2 - \left(r_{hw} - \frac{h}{2}\right)^2} \quad (2.20a)$$

$$L_{twist} = L_P/4 + 2\sqrt{r_{ew}^2 - \left(r_{ew} - \frac{h}{2}\right)^2} \quad (2.20b)$$

When the gap between two single pancake coils becomes more than 2 mm, the twisted layer jump has shorter total length (Figure 2.21). In addition, the vertical position of the cable is already at bottom pancake coil after the easyway bending. The red dot block in Figure 2.20 shows where the outer turns of top coil is able to start the winding head. It is obvious the outer turns winding in case of the twisted layer jump is available just after the easyway bending, while that of hardway bending jump is at the end of the layer jump. Thus, the twisted layer jump contributes to all subsequent outer turns. However, one always has to take into account the additional space of twisted apparent circle during the twist.

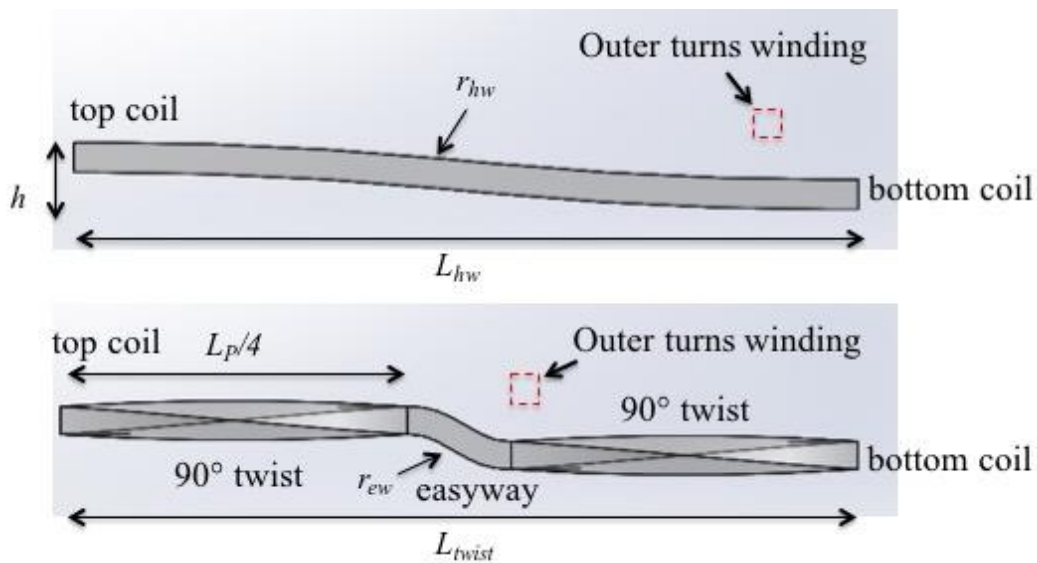


Figure 2.20 Schematic view of the layer jump using a hardway bending (top) and two twists plus easyway bending in-between (bottom).

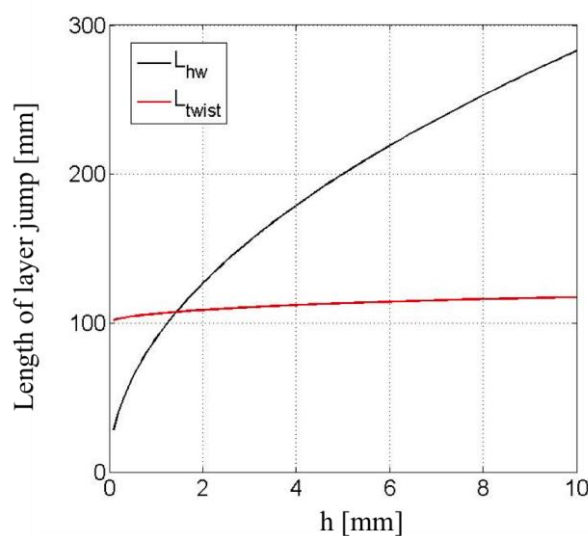


Figure 2.21 Total length of the layer jump with two 90° twists and easyway bending L_{twist} and with hardway bending L_{hw} .

2.2.3. Magnet end architecture

The objective of the magnet end architecture is to obtain the shortest and simplest magnet ends. Therefore, all twists are ideally applied at the same time. However, the 46-turn HTS insert is different from the ideal magnet ends due to the spatial problem. Now we design the magnet ends divided into two sides: transposition and turn-to-turn transition. The transposition side is composed of a twist, while the turn-to-turn transition side is composed of a layer-jump. Figure 2.22 shows the winding strategy of 46-turn HTS insert. The 46-turn HTS insert is formed of three top racetrack flat coils and three bottom flared-end coils. This makes twelve pancake coils in total for entire HTS insert, which has symmetrical design at top-bottom and right-left. Every two pancake coils from the top form a double pancake coil connected with the layer jump. They are classified into three types of double pancake coil 1) racetrack to racetrack coil, 2) racetrack to flared-end coil and 3) flared-end to flared-end coil.

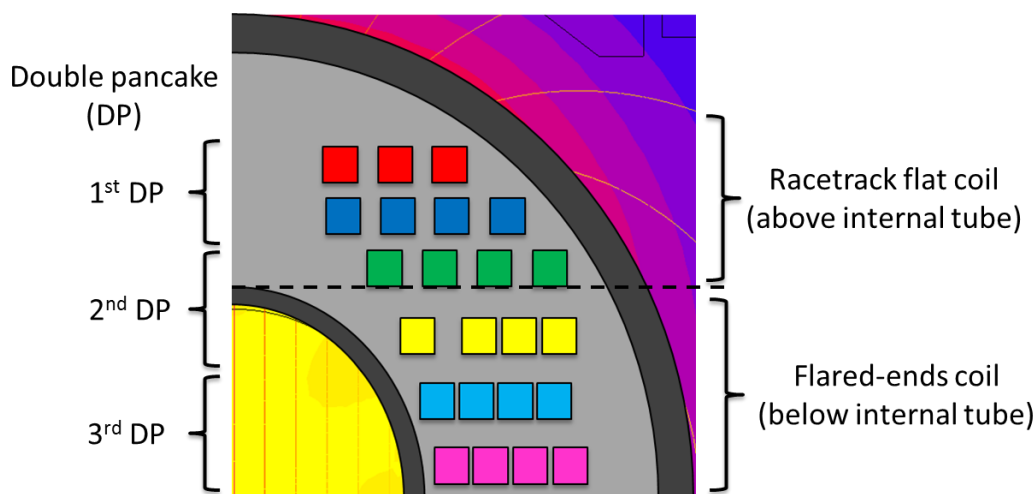


Figure 2.22 Winding strategy in magnet ends of 46-turn HTS insert.

Transposition side

Following the winding topologies of racetrack flat and flared-end coils, we can superimpose the twisted apparent circles on top of the 4x4 mm blocks at transposition side (Figure 2.23). For three top racetrack flat coils, the twist is only applied one of the sides, whereas there are twists at both the sides in a half U-turn $180^\circ + 360^\circ$ twisted winding heads in the flared-end coil (see § 2.2.2). In addition, 180° twist side of flared-end coil is shown in the figure. To keep enough space for the mechanical reinforcement during the twist, the twists at three top racetrack flat coils are separated into 1st and 3rd racetrack flat coil at the same side and the 2nd one at another side. On the other hand, the flared-end coils need the reposition of the block before the twist in magnet ends. The repositions are done with the combination of easyway and hardway bending. Moreover, the flared-end coils are needed to tilt inwards in order to avoid their winding heads overstepping into external mechanical tube. From an assembling point of view, it is suitable to lay the winding head of 4th flared-end coil on top of those of 5th and 6th.

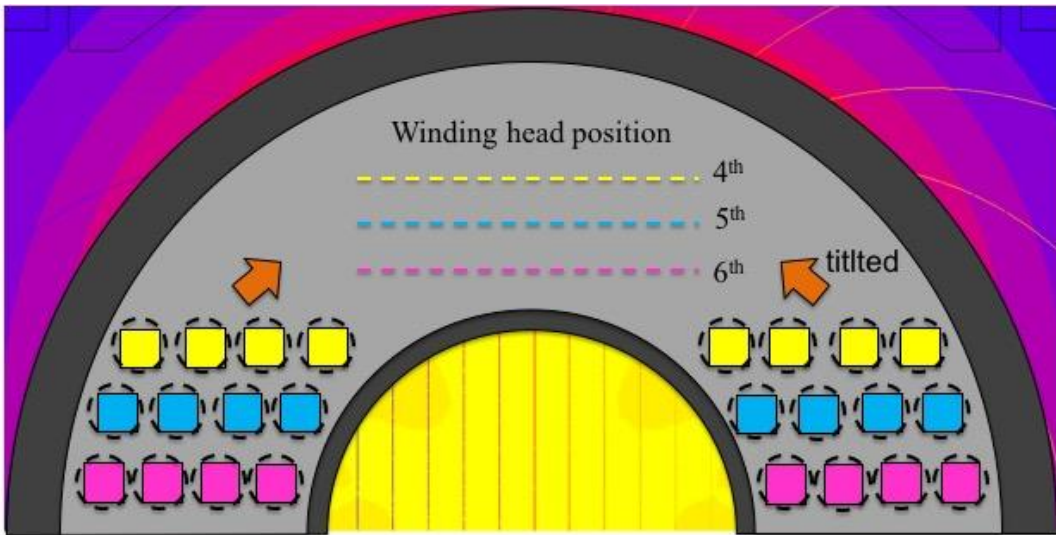
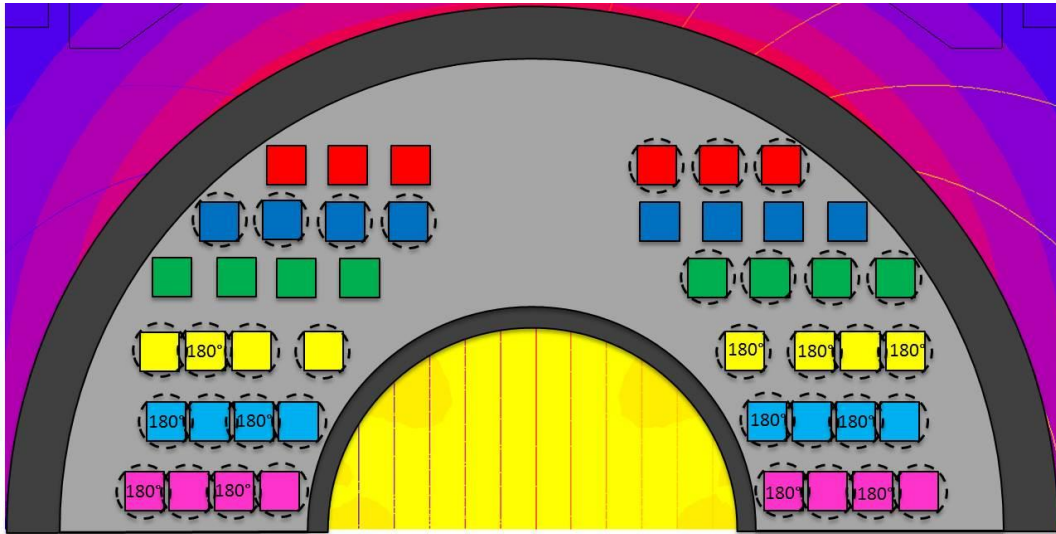


Figure 2.23 Winding strategies at transition side. Twisted apparent circles are superimposed on top of blocks (top). All blocks of flared-end coils have to be repositioned not to overlap each other while twisting and be tilted inwards not to overstep into external tube (bottom).

Turn-to-turn transition side

The turn-to-turn transition side has the inlet and outlet at outermost turns and the layer jump at innermost turns between two single pancake coils (Figure 2.24). The blocks in the same layer are connected from one to next turn across the winding head. We applied the twisted layer jump to two top double pancake coils. On the contrary, we use conventional hardway bending jump for flared-end to flared-end double pancake coil. This is because the winding head of flared-end coil is wound after that of racetrack flat coil resulting anyhow long magnet ends. Moreover, it does not have to take into account for twisted apparent circle.

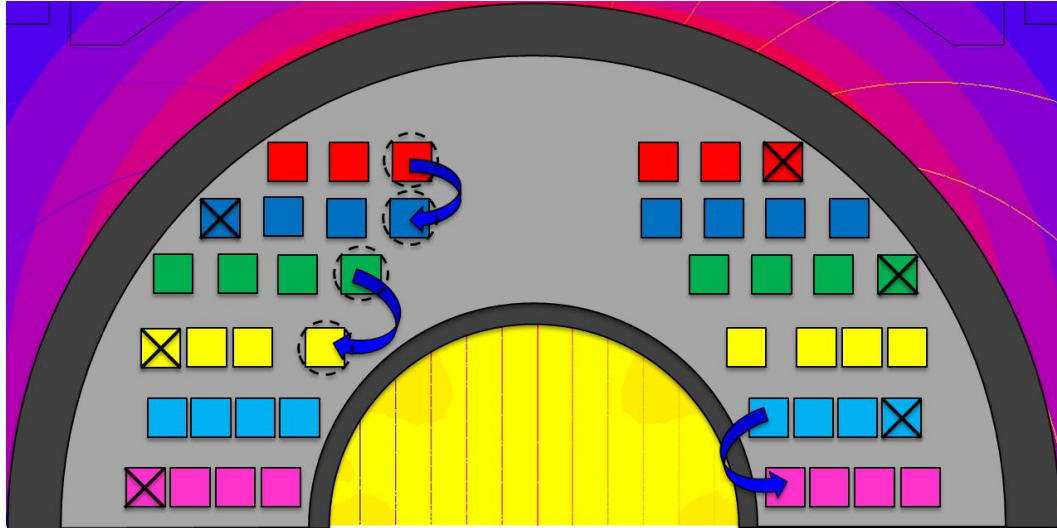


Figure 2.24 Winding strategies at turn-to-turn transition side. It is composed of inlet and outlet at outermost turns (black cross) and layer jump at innermost turns (blue arrow).

2.2.3.1. Racetrack to racetrack double pancake coil (1st DP)

A racetrack-to-racetrack double pancake coil has the simplest and shortest magnet ends. Figure 2.25 shows the magnet end architecture without straight part. At the transposition side, all turns are slightly repositioned inwards before a 100 mm long half twist. It is to ensure enough space for the mechanical reinforcement particularly for outermost turns. The transitions from one to next turn are done at the coil head at turn-to-turn transition side. The 2nd racetrack coil (325 mm) has longer magnet ends compared to the 1st one (278 mm). This is because the coil heads of outer turns are wound on top of the innermost turn where the layer jump is applied. The cable unit length (1st: 1.63 m and 2nd: 1.91 m) is derived from Eq. (2.13). The total length of the ReBCO tape is given by the multiplication between the number of stacked tape and the cable unit length.

Table 2.5
Specifications for 1st double pancake coil of racetrack-to-racetrack coil

| Parameter | 1 st layer | 2 nd layer |
|---|-------------------------|-----------------------|
| Type of layer jump | Twist + easyway bending | |
| Number of turn | 3 | 4 |
| Vertical position at straight part | 32.9 mm | 27.5 mm |
| Vertical position at winding head at transposition/ transition side | 32.9 mm | 27.5 mm |
| Min./ Max. winding radius | 9/ 25 mm | 9/ 31 mm |
| Total length of magnet ends | 278 mm | 325 mm |
| Length at transposition/ turn-to-turn transition side | 146/ 132 mm | 152/ 173 mm |
| Cable unit length in magnet ends | 1.63 m | 1.91 m |

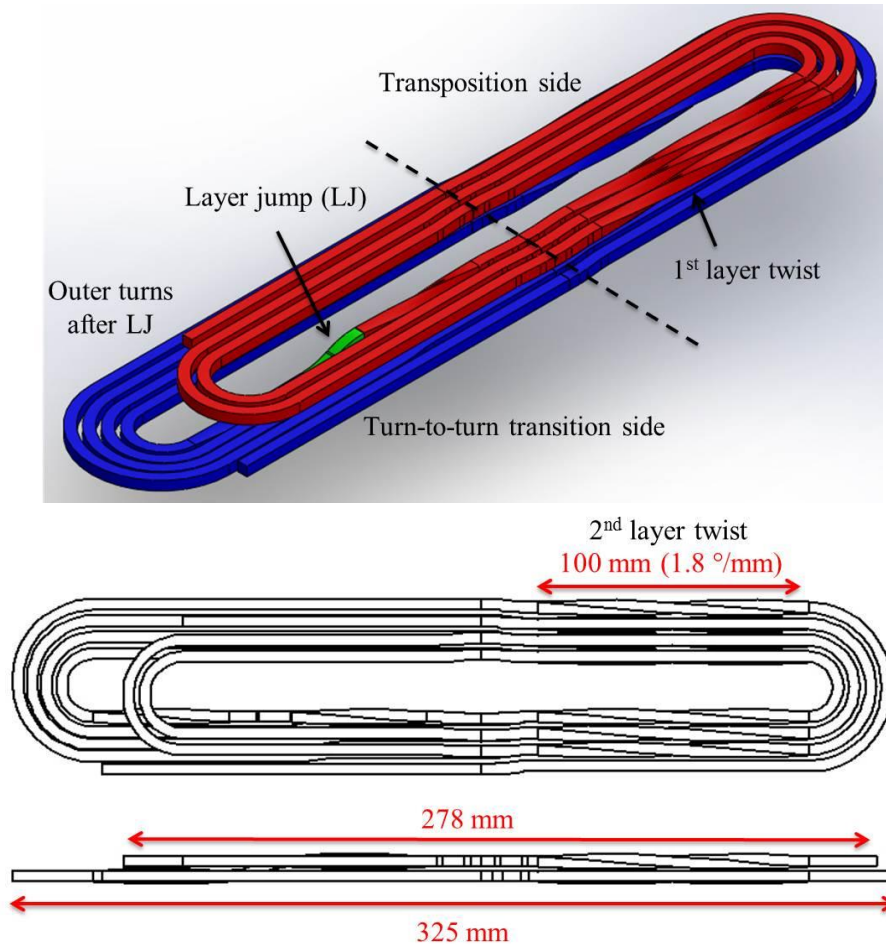


Figure 2.25 1st racetrack-to-racetrack double pancake coil in whole view (top) top view (middle) and side view (bottom).

2.2.3.2. Racetrack to flared-end double pancake coil (2nd DP)

The double pancake coil made of flared-end coil has more complicated magnet ends. The 3rd racetrack flat coil is wound using the same winding method as 1st and 2nd (Figure 2.26). On the other hands, the 4th flared-end coil forming $180^\circ + 360^\circ$ twisted winding heads induces two times longer magnet ends than 3rd one. Additionally, its length at transposition side (394 mm) is much longer than expected length (220mm) shown in Figure 2.19. This is because 3rd coil prevents 4th coil to lift. As we have mentioned, the cables of 4th coil are tilted inwards in order not to overstep into external tube while lifting. However, also due to the space limitation at inwards, they are not possible to reposition all together at the same time. Thus, the winding head of outermost turn of 4th coil is apart from the others, although it is still laid on top of 5th and 6th coils (see §2.2.3.4).

Most of the turns at turn-to-turn transition side follow the conventional winding. For example, the flared-end coils are wound only using hardway bending. The vertical position of winding head at turn-to-turn transition side is lower than that at transposition side. This is to keep the space for the inlet and outlet, which have to pass over the winding heads of flared-end coil.

Table 2.6
Specifications for 2nd double pancake coil of racetrack to flared-end coil

| Parameter | 3 rd layer | 4 th layer |
|---|-------------------------|-----------------------|
| Type of layer jump | Twist + easyway bending | |
| Number of turn | 4 | 4 |
| Vertical position at straight part | 22 mm | 15 mm |
| Vertical position at winding head at transposition/ transition side | 22 mm | 34/ 31.9mm |
| Min./ Max. winding radius | 10/ 33.7 mm | 14.8/ 34 mm |
| Total length of magnet ends | 327 mm | 737 mm |
| Length at transposition/ turn-to-turn transition side | 153/ 174 mm | 394/ 343 mm |
| Cable unit length in magnet ends | 2.43 m | 5.2 m |

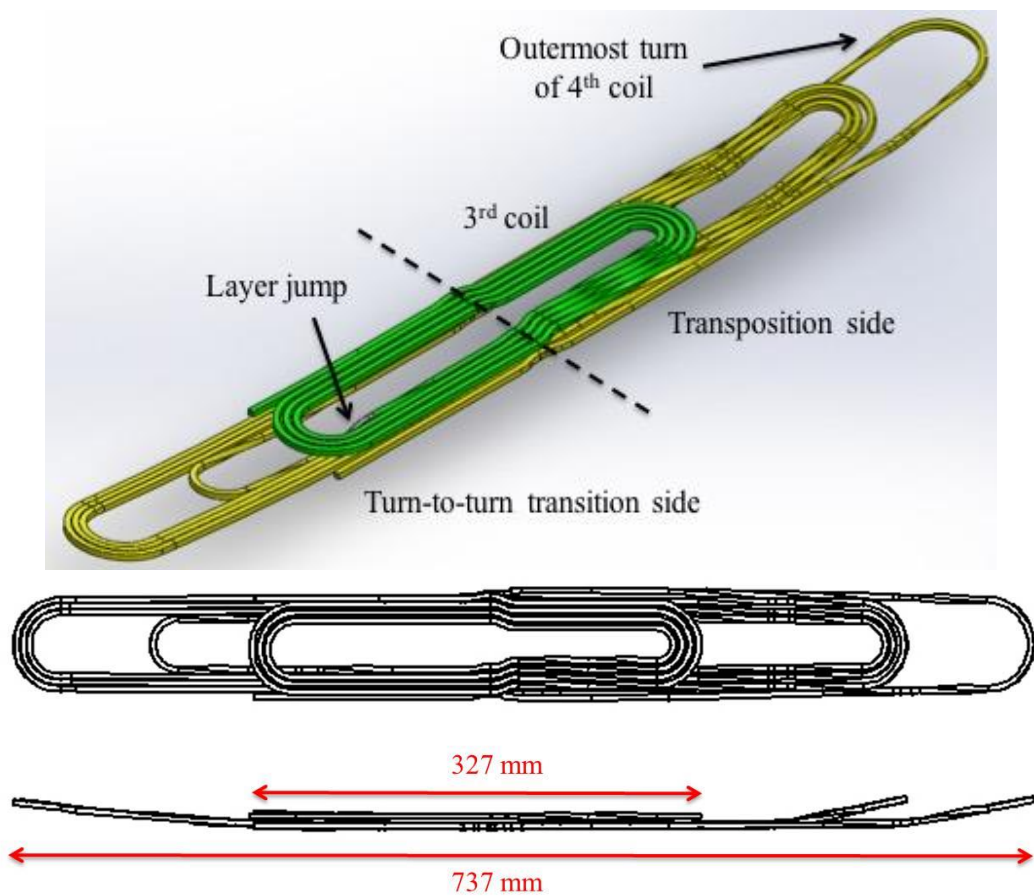


Figure 2.26 2nd racetrack to flared-end double pancake coil in whole view (top) top view (middle) and side view (bottom).

In Figure 2.26, the layer jump is done with two 90° twists and easyway bending in-between. However, the horizontal positions of innermost turn for 3rd and 4th coil are not aligned. Moreover, the stacked cable has to be lifted up to winding head of 4th coil after the layer jump. Hence, we apply a dual role on the layer jump (Figure 2.27). The first 90° twist starts from the original horizontal position at innermost turn of 3rd coil ($x = 10$ mm). Then, it jumps from 3rd to 4th coil across the easyway

bending. At the end of the easyway bending, the cable is slightly tilted upwards in order to facilitate to lift up to the winding head of 4th coil. The second 90° twist thus plays a dual role in its layer jump and sharp winding head. At the winding head of 4th coil, the horizontal position goes from 3rd ($x = 10 \text{ mm}$) to 4th ($x = -14.8 \text{ mm}$) coil.

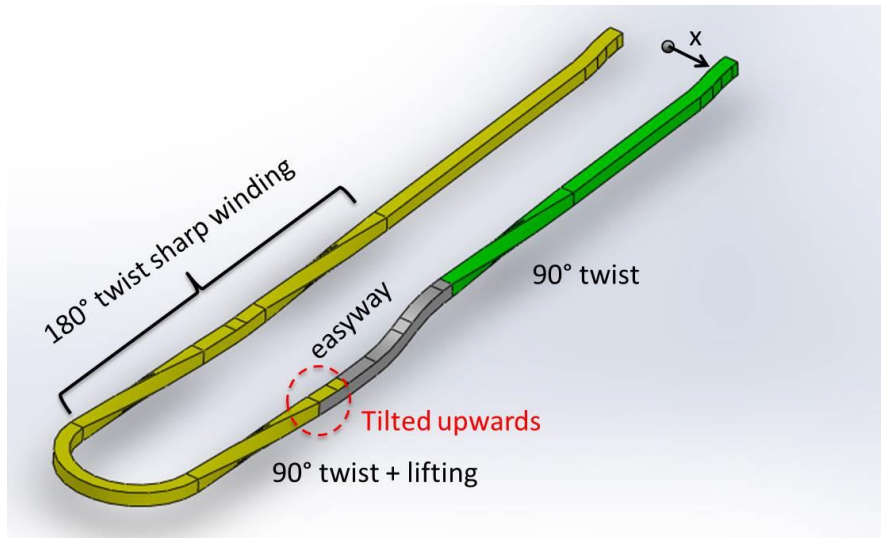


Figure 2.27 Layer jump of 2nd double pancake coil between 3rd and 4th coils.

2.2.3.3. Flared-end to flared-end double pancake coil (3rd DP)

A flared-end to flared-end double pancake coil brings the longest magnet ends among three double pancake coils. It is designed under consideration of two previous double pancake coils. For this reason, the positions of the winding head at transposition side are divided into two parts, which are the same structure as 4th flared-end coil (Figure 2.28). Moreover, the turn-to-turn transition side has also the same structure using hardway bending. The layer jump at the innermost turn uses conventional hardway bending. It is located between the winding head of 5th coil and the straight part of 6th coil.

Table 2.7
Specifications for 3rd double pancake coil of flared-end to flared-end coil

| Parameter | 5 th layer | 6 th layer |
|--|-----------------------|-----------------------|
| Type of layer jump | Hardway bending | |
| Number of turn | 4 | 4 |
| Vertical position at straight part | 8.2 mm | 1.4 mm |
| Vertical position at winding head at transposition/ transition jump side | 29/ 28.3 mm | 25/ 23.6 mm |
| Min./ Max. winding radius | 20.6/ 38.7 mm | 24.1/ 41.7 mm |
| Total length of magnet ends | 767 mm | 799 mm |
| Length at transposition/ turn-to-turn transition jump side | 399/ 368 mm | 402/ 397 mm |
| Cable unit length in magnet ends | 5.9 m | 5.53 m |

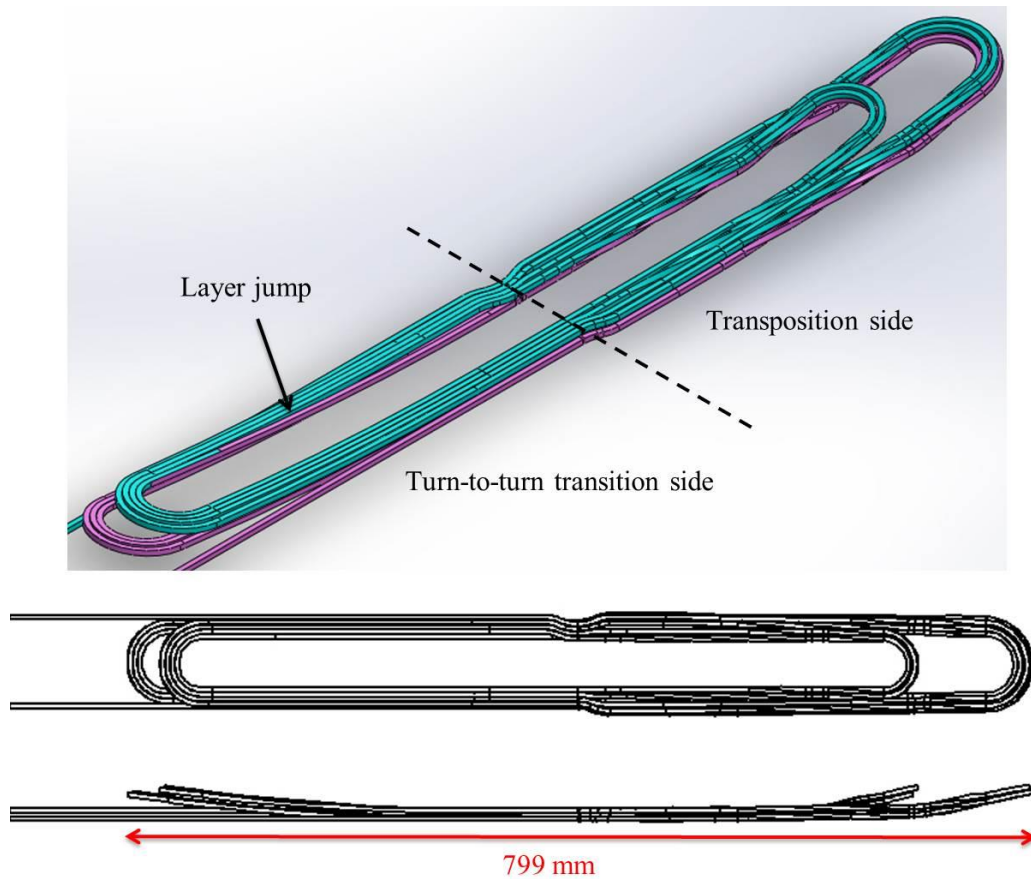


Figure 2.28 3rd flared-end to flared-end double pancake coil in whole view (top) top view (middle) and side view (bottom).

2.2.3.4. Short summary

Figure 2.29 shows the assembly of three double pancake coils of 46-turn HTS insert. It is composed of the magnet ends at 402 mm transposition and 397 mm turn-to-turn transition sides without straight part in-between. Each inlet and outlet of the double pancake coils continues to the joint termination at the extremity of the dipole magnet. Those of the racetrack coils must pass over the winding heads of the flared-end coils. In order to do so, the twist and easyway bending is used. In consequence, the entire magnet ends are 799mm in total using 22.6 m of stacked cable.

Table 2.8
Specifications for magnet ends of 46-turn HTS insert

| Parameter | Value |
|--|-------------|
| No. of single/ double pancake coil | 12/ 6 |
| Total length of magnet ends | 799 mm |
| Length at transposition/ turn-to-turn transition side | 402/ 397 mm |
| Cable unit length in magnet ends | 22.6 m |

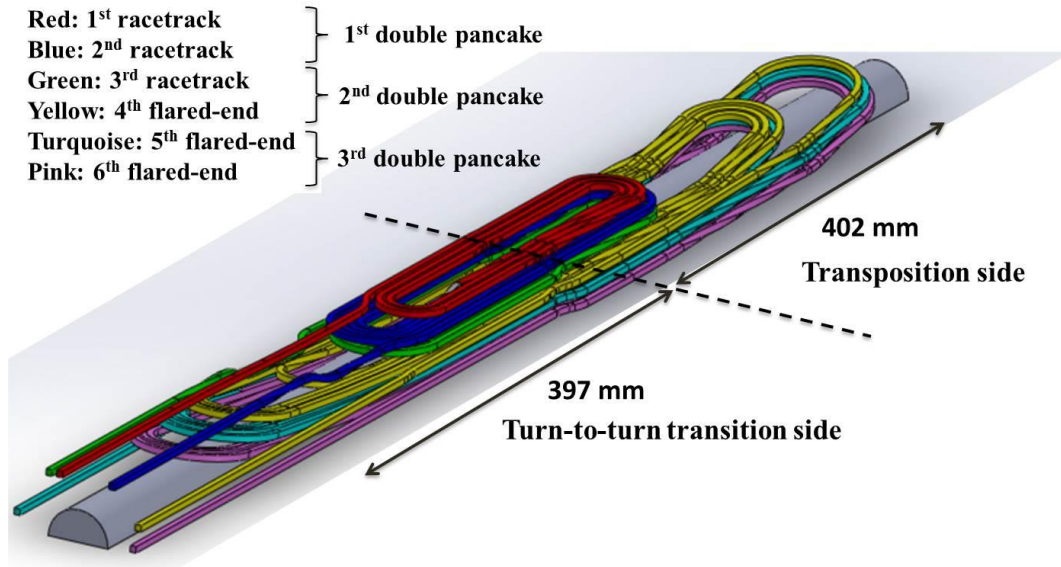


Figure 2.29 Magnet-ends of 46-turn HTS insert with three racetrack coils and three flared-end coils forming three double pancake coils.

2.2.4. Electromagnetic property of magnet ends

As we already mentioned, a twist of the stacked cable in magnet ends may expose a high magnetic field in the wide face of the ReBCO tape where the engineering current density is lower. It is important to know the field distribution of magnet ends in 46-turn HTS insert to determine where the weakest zone is located. We thus study the magnet ends of 46-turn HTS insert in a standalone mode using 3D numerical analysis in static mode. The analyses are separated into two parts: transposition and turn-to-turn transition side. We put a 710 MA/m^2 of homogeneous operating current density into all 46 turns. The J_e is then calculated from the amplitude and angle of magnetic field.

Transposition side

Figure 2.30 shows the 3D distribution of field amplitude in a standalone mode at transposition side. The high field zone in the range of 5 to 6 T, which is mostly vertical component, is situated at the innermost turns of three top racetrack flat coils. Moreover, the highest point is at the winding head of innermost turn at 2nd layer. The field weakens as it goes to outer turns and to farther from the straight part of dipole magnet. The lowest J_e in magnet ends appears when the innermost turn of 2nd layer is twisted for 90° angles, which experiences a 5 T of transverse field. Figure 2.31 shows the field distribution of vertical component at the 2D cut-planes where the lowest J_e occurs. It is 70 mm far from the straight part. Besides, the stacked cables of three top racetrack flat coils are twisted for 90° angles. The highest field zone is very localized at inner parts of innermost turn at 2nd layer. Moreover, the variation of field amplitude in the innermost turn is 3.3 – 5 T. Therefore, its outer tapes will have higher J_e . Thus, its current distribution can be inhomogeneous. In the same manner, all turns in magnet ends will have an inhomogeneous distribution J_e .

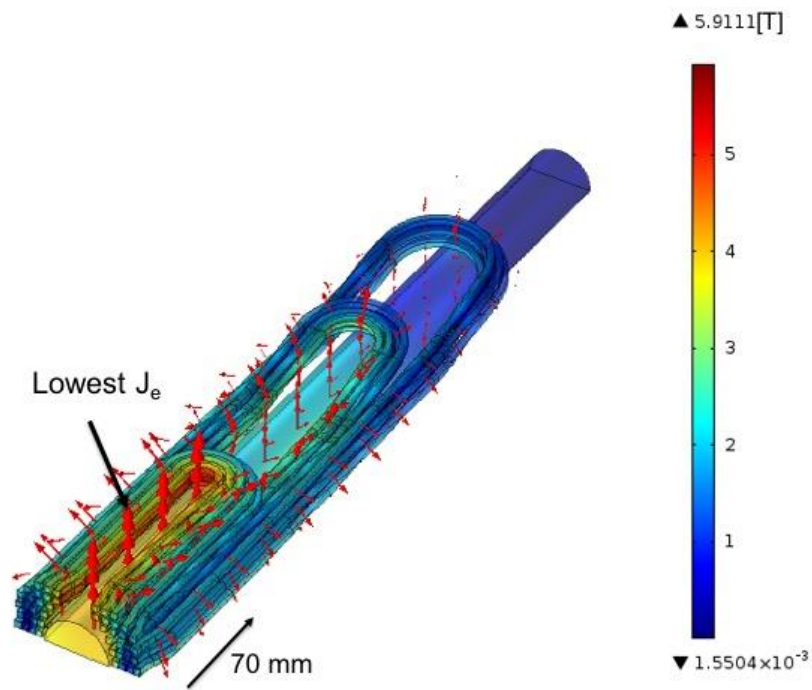


Figure 2.30 3D distribution of field amplitude at transposition side.

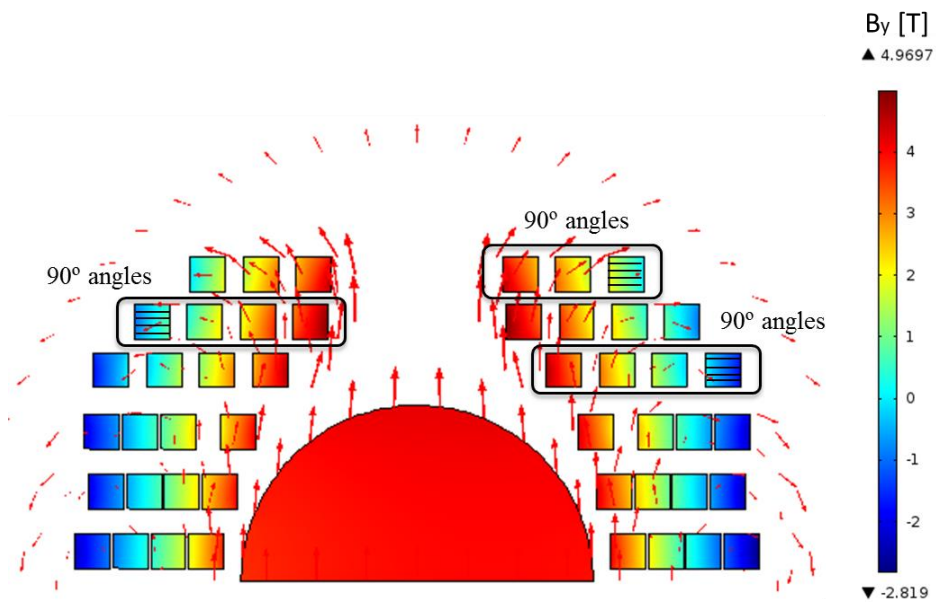


Figure 2.31 Distribution of vertical field B_y in 2D cross-section at transposition side where three top racetrack coils are twisted for 90° angles.

Turn-to-turn transition side

In principle, the turn-to-turn transition side has the same distribution of field amplitude as that of transposition side except it has only two twisted parts located in layer jump (Figure 2.32). Therefore, the weakest zone, in other words, the lowest J_e occurs when the stacked cable is twisted for 90° in the layer jump between 1st and 2nd layers, which is a 4.9 T of transverse field.

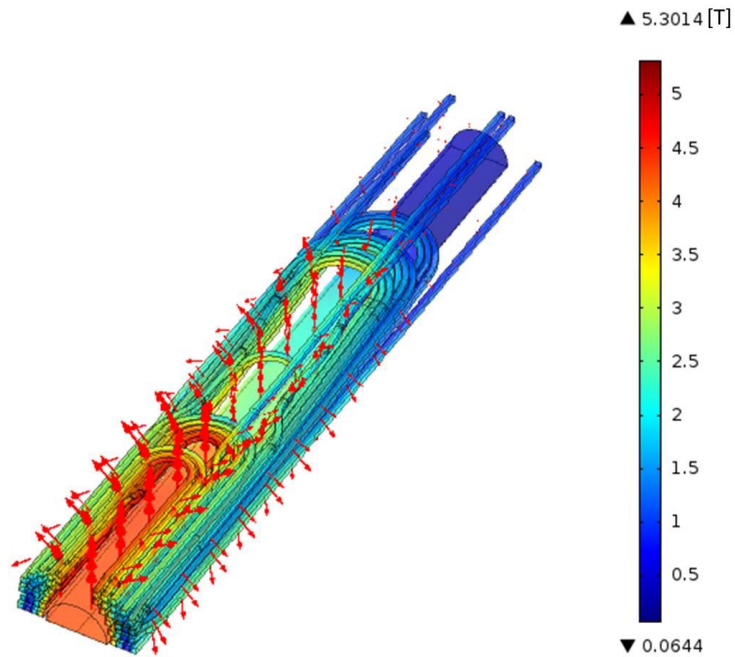


Figure 2.32 3D distribution of field amplitude at turn-to-turn transition side.

2.3. Operational margins of HTS insert

2.3.1. Relative magnet ends position of HTS insert and LTS outsert

A well-uniform magnetic field in the beam aperture is the contribution of the 2D cross-section of both HTS insert and FRESKA2 LTS outsert at straight part. On the contrary, the magnet ends are designed to be as short as possible because the field quality is anyhow not good. For this reason, it is preferred to locate the magnet ends of HTS insert inside those of LTS outsert. However, the analysis of magnet ends in 46-turn HTS insert in a standalone mode already has a 5 T of maximum transverse field at the twisted part. Furthermore, the field of LTS outsert can even lower the J_e . Thus, it is important to adjust the relative position of magnet ends between insert and outsert to keep enough operational margins (high J_e).

The FRESKA2 LTS outsert has about 1.7 m magnet ends in total, 0.85 m at both sides, whereas that of 46-turn HTS insert is 0.8 m in total, 0.4 m at both sides. The magnetic field of LTS outsert decreases as it goes farther from straight part (13 T) to the end of the magnet ends (-0.2 T). Figure 2.33 shows the variation of vertical field of outsert's magnet ends along its longitudinal direction at the innermost turn of 2nd layer in 46-turn HTS insert, where the lowest J_e is foreseen in a standalone mode. The magnetic field of outsert remains over 10 T between 0 - 0.5 m, and 5 - 10 T between 0.5 - 0.67m. To keep the enough operational margin to J_e , a 150 mm of magnet ends of insert is located outside of magnet ends of outsert according to the I_C measurement of 4 mm SuperOX ReBCO tape in Grenoble [63]. Hence, the highest transverse field penetration becomes 10 T leading $J_e = 1770\text{MA/m}^2$ that is 42% lower from original J_e .

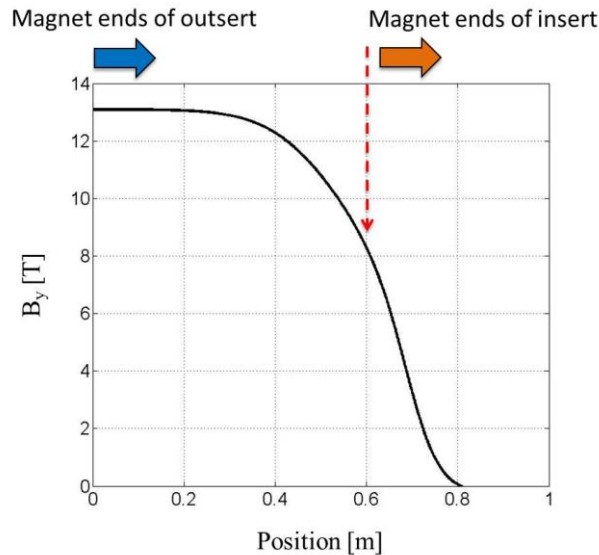


Figure 2.33 Variation of vertical field B_y of FRESKA 2 outsert's ends along its longitudinal direction at the innermost turn of 2nd layer in 46-turn HTS insert, where the lowest J_e is foreseen in a standalone mode.

2.4. Conclusions

In the framework of EuCARD2 project, first Twisted Stacked/ Block-type HTS insert is presented in regard to the 2D design at straight part and the 3D twisted magnet ends. The straight part and the magnet ends are strongly linked together in terms of the reproducible manufacturability. Therefore, the unique constraints are taken into account at first design stage. The 46-turn HTS insert using 4x4 mm block provides a 5 T quality of the magnetic field in a standalone mode with the operating current density smaller than the target engineering current density ($< 700 \text{ MA/m}^2$). In the 17 T hybrid magnets with the FRESCA2 LTS outsert, the HTS insert is almost aligned to the background field to make the best use of the J_e and favorably to reduce the transverse field on the insert. In addition, it also helps to direct the mechanical forces onto the flat surface of the ReBCO tape.

In the magnet ends, it is composed of six double pancake coils separated into the transposition side with one twist per turn and the turn-to-turn transition side. It profits the sharp winding head using two 90° twists and easyway bending in-between for the flared-end coil. It ends up an 800 mm in total length. As there is a twist in magnet ends, even a small field amplitude drastically reduces its J_e because of the transverse direction. In addition, the non-uniform distribution of J_e inside the stacked cable causes inhomogeneous current distribution, which has a harmful impact on the field quality. On top of that, the asymmetric magnet ends anyhow result in bad field quality. From a point of view of the operational margin, the relative position of magnet ends of HTS insert and LTS outsert is important to keep high J_e from original value. Hence, some magnet ends of HTS insert is located outside of magnet ends of LTS outsert.

The twisted stacked/ block-type HTS insert is designed to severely fulfill the 5 T magnetic field using present available superconducting properties. For this reason, 46-turn of the stacked cable is used, which caused complicated long magnet ends. The number of turn can be reduced if the performances of the ReBCO tape improve or the required magnetic field is reduced. For example, the magnet ends will drastically get simpler and shorter if more than six turns are removed.

Chapter 3

Current distribution in HTS stacked cable

The 46-turn HTS insert using a 4x4 mm twisted stacked cable is designed based on the assumption of uniform operating current density J_{op} . However, the twisted stacked cable may cause inhomogeneous current distribution due to the partial transposition and long twist transposition pitch in our design. In addition, the magnetization, which is unique feature in a superconductor, must be taken into account. Therefore, we study the electromagnetic behavior of twisted stacked cable using a numerical approach.

3.1. Numerical analysis of twisted stacked cable

3.1.1. Electromagnetic behavior of twisted stacked cable

We remind that a cable and then a stacked cable used in HTS inserts must meet the following requirements for the purpose of high performance accelerator magnets:

1. Uniform current distribution
2. Low magnetization
3. Possible to redistribute the current for stability

The first two items are during normal operation. These are to assure the good field quality. On the other hand, last item is about mitigating the consequences of the tape defect. To answer these expectations, we use a twisted stacked cable in HTS insert. The concept is to make the stacked cable partially transposed by applying the twist in magnet ends, and thus it is expected to bring the same electromagnetic conditions to the tapes in the cable (see § 2.2).

In our 46-turn twisted stacked/ block-type HTS insert, only one twist per turn is applied in 15 m long magnet. This very long twist transposition pitch may increase the magnetization and lead to non-uniform current distribution in most cases, which acts like a non-twisted stacked cable. As a preliminary step, we study the electromagnetic behavior in terms of magnetization and current distribution using a finite element method for various stacked cable structures:

- Non-insulated stacked cable (NI-SC)
- Non-insulated twisted stacked cable (NI-TSC)
- Insulated twisted stacked cable (I-TSC)

Qualitatively these three configurations have following behaviors:

- NI-SC: Possible current redistribution between the tapes but the coupling of the tapes
- NI-TSC: Possible current redistribution but the decoupling of the tapes through twisting
- I-TSC: No more possible current redistribution between the tapes but priori strong decoupling

The first objective of this chapter is to study qualitatively these configurations in 46-turn HTS insert. Then, we see quantitatively its field quality including magnetization-

induced harmonics. We thus use a numerical software ‘FLUX[®]’[94]. The simulation list is shown in Table 3.1. In 2D analysis, we design the upper-half of 46-turn HTS insert using twenty tapes of NI-SC and I-TSC. On the other hand, due to long computational time in 3D analysis, we build the simplified model using four tapes of NI-TSC, which is impossible to implement in 2D due to the capability of FLUX[®]. This allows to determine qualitatively its behavior.

Table 3.1 Simulation List

| Type of simulation | NI-SC | NI-TSC | I-TCS |
|--------------------|-------|--------|-------|
| 2D analysis | ○ | × | ○ |
| 3D analysis | ○ | ○ | × |

3.1.2. Numerical setup in FLUX[®]

FLUX[®] is a numerical software developed by Cedrat collaborated with Grenoble INP. It is dedicated to the static and transient electromagnetic simulation with advanced electrical circuit coupling. It can solve the non-linear problem such as a superconductor. Now, we present the numerical setup of non-twisted and twisted stacked cables including the operating condition by using various environment in FLUX[®] (geometry, mesh, electric circuit coupling etc.).

Operating condition

The main features of the HTS stacked cable in the accelerator magnets during normal operation are:

- A) Magnetization due to the external field
- B) Current distribution during the ramp current mode
- C) Current distribution under the DC mode

To correctly evaluate these behaviors in numerical software, we propose the operating condition depicted in Figure 3.1, which may not be the same in reality. We first apply gradually the magnetic field B_{ext} and then ramp up the transport current I_a . We maintain the B_{ext} and I_a for certain duration to see the current exchange between the tapes in the cable.

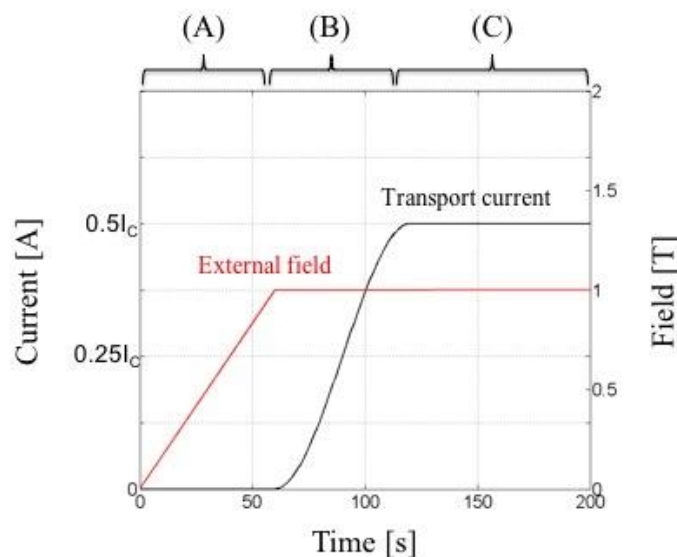


Figure 3.1. Example of operating condition for HTS stacked cable. (External field B_{ext} : 0 – 1T, Ramp current I_a : 0 – $0.5I_C$ A)

The B_{ext} is increased up to 1 T instead of 13 T, which is the amplitude of background field of the FRESKA2 LTS outsert. This is because 1 T of external field is enough to fully penetrate the stacked cable. Therefore, it shows qualitatively the same behavior of magnetization as that of 13 T. This makes it possible to shorten considerably computational time. The transport current I_a fills the cable up to 50 – 70% of its critical current, which brings the same J_{op} , i.e. load factor $I_a / I_{C-cable}$, as that of 46-turn HTS insert.

Specification of ReBCO tape

The 46-turn HTS insert is made of 4x4 mm HTS twisted stacked cable with $J_{op} = 650 \text{ MA/m}^2$. In our simulation model, we divide this cable into twenty ReBCO tapes. This brings 4 mm width and 0.2 mm thickness. The tape is made of 0.02 mm thick superconducting layer interposed by 0.15 mm and 0.03 mm thick resistive layers, which is similar to actual tape structure (Figure 3.2). However, the superconducting layer is ten times thicker than actual one ($= 2 \text{ }\mu\text{m}$) due to complicated meshing structure in FLUX[®], particularly in 3D. To take enough operational margin to J_{op} , the overall engineering current density J_e is set to be $1,000 \text{ MA/m}^2$. Therefore, the critical current I_C and critical current density at superconducting layer J_C becomes 800 A and $10,000 \text{ MA/m}^2$, respectively. Besides, n -value is 20.

The ReBCO tape follows the superconducting E - J power law. It is considered independent to the strength and angular of the magnetic field. This is because the tapes in the stacked cable in 46-turn HTS insert are aligned to the background field. Furthermore, there is small variation in field amplitude between the tapes in the stacked cable.

Table 3.2
Specification of ReBCO tape

| Parameter | Value |
|-----------------------------------|-------------------------|
| Width/ Thickness of tape | 4/ 0.2 mm |
| Thickness of SC layer | 0.02 mm |
| Thickness of resistive layers | 0.15/ 0.03 mm |
| Critical current I_C | 800 A |
| Engineering current density J_e | $1,000 \text{ MA/m}^2$ |
| Critical current density J_C | $10,000 \text{ MA/m}^2$ |
| n -value | 20 |

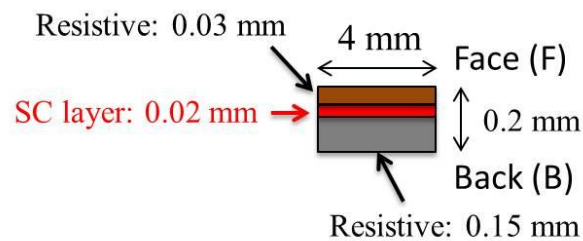


Figure 3.2 Cross-section of ReBCO tape.

Cross-section of stacked cable

The ReBCO tapes are often bundled into a face-to-back configuration, whose 0.03 mm and 0.15 mm thick resistive layers are facing each other (Figure 3.3). However, a half twist of this stacked cable causes the asymmetric design due to the asymmetric cross-section of ReBCO tape. For this reason, we propose a F^2 -to- B^2 -to- F^2 configuration. For example, in case of four-tape stacked cable, two sets of a face-to-face configuration (F^2) is bundled into a back-to-back configuration (B^2). Thus, the HTS insert can keep the symmetric design even after a half twist. This configuration is also expected to help the current exchange of two superconducting layers through face-to-face contact, whose adjacent resistance is smaller than that of back-to-back and even face-to-back contacts.

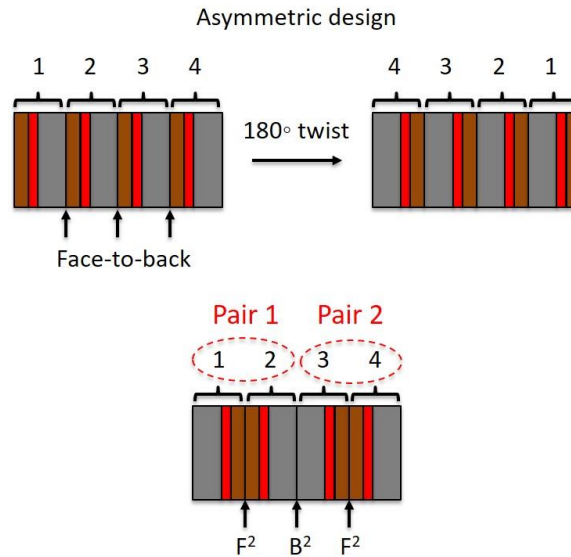


Figure 3.3 Cross-section of four-tape stacked cable with a face-to-back configuration (top) and with a F^2 -to- B^2 -to- F^2 configuration (bottom).

3D geometry

As we mentioned, a simplified model is needed for 3D analysis due to long computational time. Its structure must meet the requirements of:

- Long twist transposition pitch
- Capability of FLUX[®] in meshing

We thus modeled a straight conductor with a 100 mm of half twist ($T_P = 1.8$ °/mm) interposed by two long straight part instead of a U-turn coil, which has complicated mesh structure. In FLUX[®], it is possible to extrude the original face being straight forced, bended or twisted. Figure 3.4 shows the four-tape twisted stacked cable whose original face is made of a F^2 -to- B^2 -to- F^2 configuration.

Meshing

A mesh for such a thin and wide superconducting layer is extremely difficult. Its aspect ratio can be as high as 10^4 . Therefore, a mapped mesh is usually applied instead of a triangular mesh. It can drastically decrease the total number of mesh elements. As we mentioned the actual thickness of superconducting layer (2 μm) is ten times thinner than that of our model in FLUX[®] (20 μm). This difference will affect the behavior of magnetization quantitatively, which can bring harmful impact

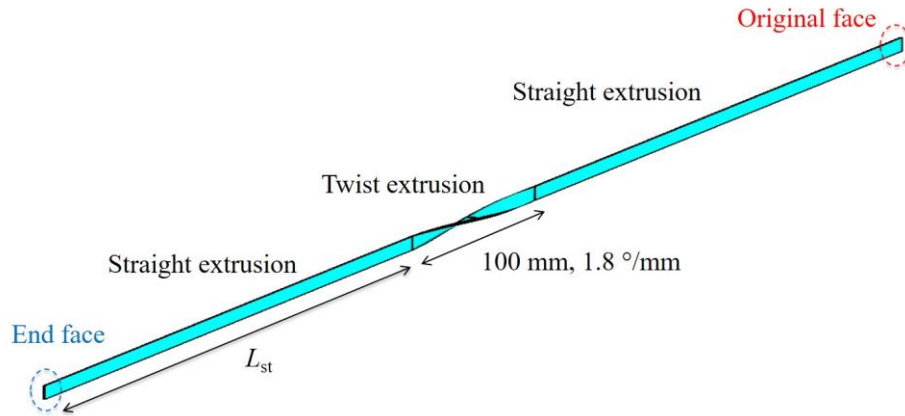


Figure 3.4 Four-tape twisted stacked cable with a 100 mm of half twist interposed by two straight part, whose original face is a F^2 -to- B^2 -to- F^2 configuration.

on field quality study. Therefore, we placed only one single line of mesh element on its $20\ \mu\text{m}$ thickness (see Figure 3.5). This will evaluate the behavior of $20\ \mu\text{m}$ thickness as if it is $2\ \mu\text{m}$ thickness.

In case of a meshing of 3D geometry, we can simply sweep the mesh pattern of original face along cable's length direction. This helps to mesh even very long twisted stacked cable with very thin cross-section (see Figure 3.6)

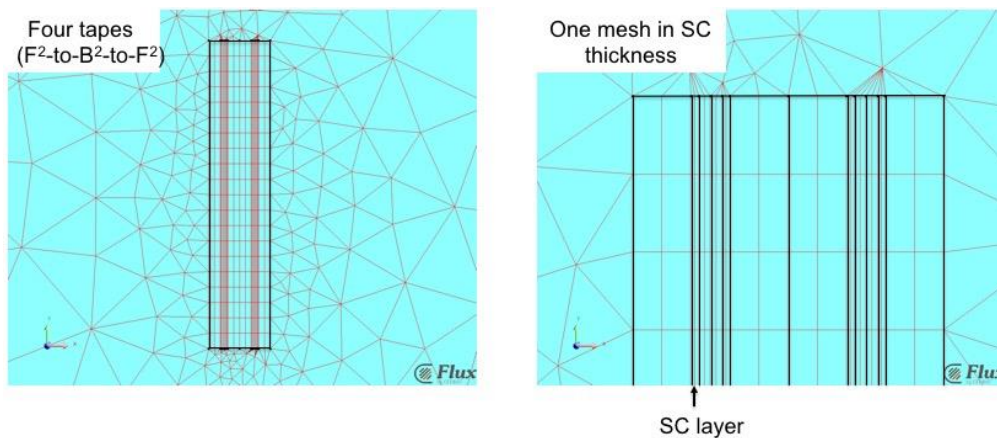


Figure 3.5 Mapped mesh for four tapes with a F^2 -to- B^2 -to- F^2 configuration (left) and its large-scale view focused on SC layer (right).

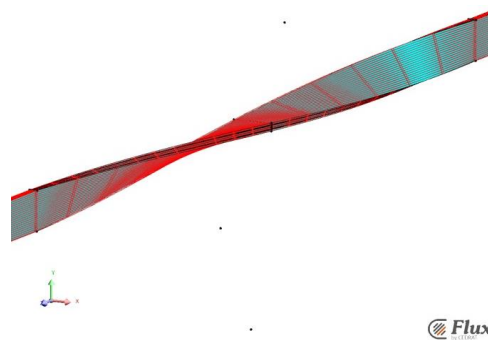


Figure 3.6 Sweep mesh of four-tape twisted stacked cable at twisted part whose original face has mapped mesh.

Electrical circuit coupling

An electrical circuit coupling can easily create an electrical loop between the geometric elements. The circuit can be composed of the large variety of circuit components (e.g. current source, resistance, inductance etc.). This saves a computational time instead of adding its equivalent geometrical element.

Figure 3.7 shows the example of electrical circuit coupling for four-tape stacked cable, which is composed of current source I_a , equivalent self-inductance L of 46-turn HTS insert, resistance R_i equivalent to joint termination and conductor with start (S) and end points (E), which is assigned to geometric element.

As we have seen in Table 3.1, the non-insulated stacked cable (NI-SC) and insulated twisted stacked cable (I-TSC) are capable to represent in 2D analysis with *circuit A* and *circuit B*, respectively. For NI-SC, the start point of conductor I at *circuit A* is assigned to all faces (tape 1 - 4) at right side of 2D geometry, while that of end point is assigned to those of left side (tape 1' to 4'). On the other hand, four-tape I-TSC requires four conductors I- IV. These start and end points at *circuit B* are assigned;

- Conductor I: Start point → tape 1, End point → tape 4'
- Conductor II: Start point → tape 2, End point → tape 3'
- Conductor III: Start point → tape 3, End point → tape 2'
- Conductor IV: Start point → tape 4, End point → tape 1'

Thus, the innermost tape 1 at right side is electrically connected with the outermost tape 4' at left side, which represent a twist. In addition, FLUX automatically generates an insulation when the faces next to each other assigned to different conductors. We can assign the conductors to original and end faces in Figure 3.4 in the same manner as 2D geometry.

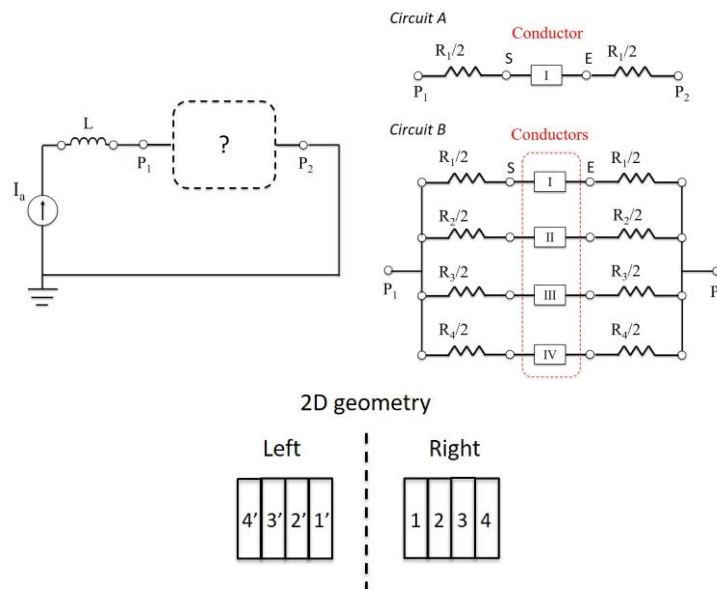


Figure 3.7 Electrical circuit coupling with *circuit A* (1 conductor) and *circuit B* (four conductors) for four-tape stacked cable (top). The conductors are assigned to proper face of tape 1 – 4 and 1' – 4' (bottom).

3.1.3. Non-insulated non-twisted stacked cable

The magnetization and current distribution in a single superconducting tape can be well expressed with the Bean's model. The current distribution inside the tape is related to its magnetic field distribution. Two behaviors of magnetization are known for the stacked cable under parallel field: non-coupled and coupled behaviors. For the non-coupled behavior, every tape in the stacked cable acts as a single tape, which means half part of the tape has $+J_C$ and the other half part has $-J_C$. Thus, the current is confined in each individual tape. We refer this current as a screening current. On the other hand, the entire stacked cable acts as large single-tape in case of coupled behavior. The coupling current circulates through the whole cable passing the adjacent resistive layer as well. It results in more magnetization, and it is thus expected to have more harmful impact on the field quality.

The behavior of magnetization is determined by three parameters: total length of the conductor l , the adjacent resistivity between superconducting layers ρ_{ad} and the sweep rate of the magnetic field \dot{B} . We set $1 \text{ m} < l < 200 \text{ m}$ and $\dot{B} = 1 \text{ T/min}$ based on the practical accelerator magnet. In such a long and slow sweep rate always results in the coupled behavior at $1 \text{ n}\Omega\cdot\text{m} < \rho_{ad} < 300 \text{ n}\Omega\cdot\text{m}$. Figure 3.8 shows the current density distribution and current waveform of four-tape stacked cable in 2D analysis (B_{ext} : 0 – 1 T and I_a : 0 – 1.6 kA). When the external fields are exposed, the coupling current first flows into the outer tapes. It then flows into the inner tapes when the outer tapes are fully penetrated and carrying critical current. The left half side of the cable has positive current while that of right half side has negative current. It makes big current loop all along the cable or even the magnet. During the ramp current mode, the transport current only fills up the tapes at right half side of the cable where the current is negative. Besides, their current distribution is related to the field distribution. This is because the other tapes at left half side of the cable possessing positive current already have the high load factor $I/I_C (>0.8)$. At the end of the ramp current mode, the tapes can exchange the current through the adjacent resistance. Figure 3.8 is in case all joint resistances at termination are same. For this reason, all tapes are homogenizing to carry 400 A. However, in case of long length dipole magnets, the current tends to flow into the innermost tape whose impedance is smallest.

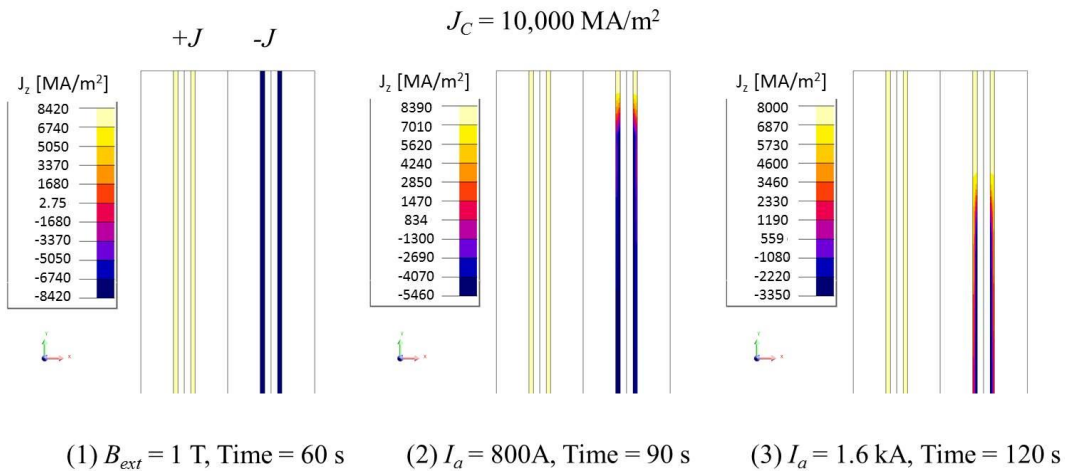


Figure 3.8 (a) Distribution of current density of four-tape NI-SC at one third of its upper part.

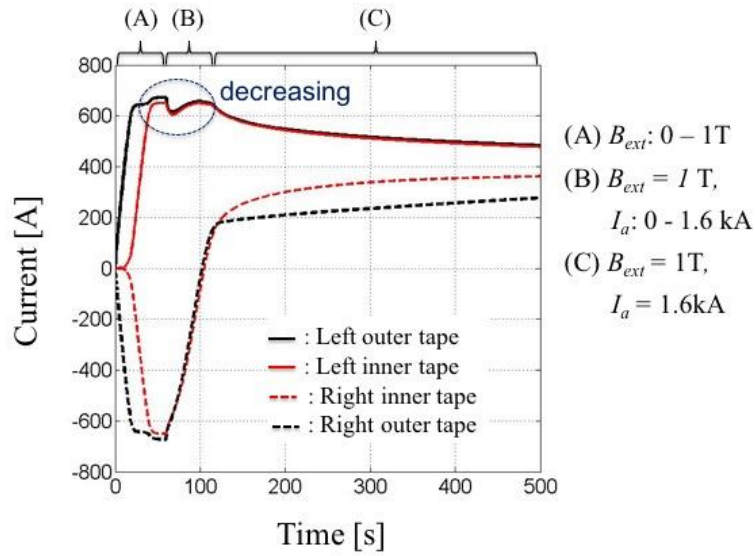


Figure 3.8 (b) Current waveform of four-tape NI-SC during $B_{ext}: 0 - 1\text{T}$, $I_a: 0 - 1.6\text{kA}$.

In Figure 3.8 (b), one can observe the current at left half side possessing positive current are slightly decreasing at the very beginning of the ramp current mode. This is because of the decay of coupling currents. Figure 3.9 shows the variation of coupling current in case there is no transport current. When the external field gets constant ($B_{ext} = 1\text{T}$), the coupling current decreases up to certain level and then is saturated. Thus, the superconducting accelerator magnets must consider for the magnetization-induced harmonics.

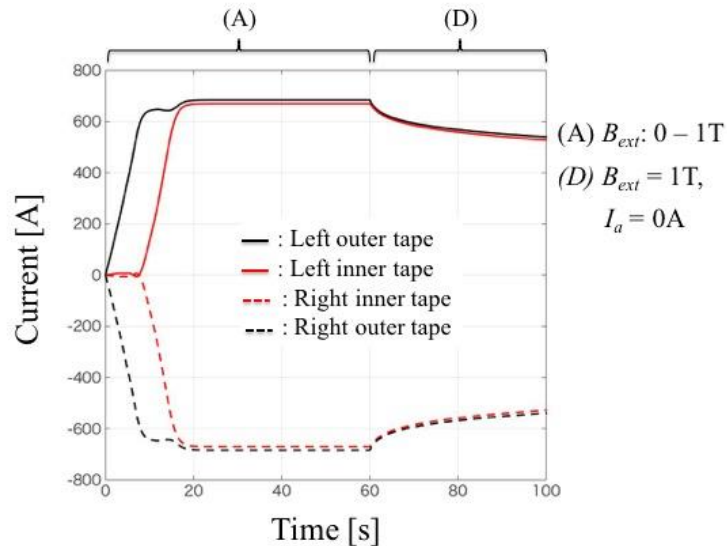


Figure 3.9 Current waveform of four-tape NI-SC during $B_{ext}: 0 - 1\text{T}$.

3.1.4. Non-insulated twisted stacked cable

One of the objectives of the twisted stacked cable is to obtain non-coupled behavior, which is expected to generate less magnetization-induced harmonics. The non-insulated twisted stacked cable allows the current exchange through the adjacent contact R_{ad} between the tapes (Figure 3.10). This assists to homogenize the current distribution even when the joint resistances R_i are not the same. However, it may still cause the coupled behavior depending on the length of non-twisted part (straight part) L_{st} , sweep rate of field \dot{B} and adjacent resistivity ρ_{ad} [95 - 97].

$$l_c^2 = \left(\frac{16J_e \rho_{ad} t_{sc}}{\dot{B}} \right) \left(\frac{t_{ad}}{t_{sc} + t_{ad}} \right) \quad (3.1)$$

Eq. (3.1) shows the critical length l_c , which determines the behavior of magnetization: non-coupled or coupled behavior.

In 46-turn HTS insert has only one twist per turn ($1.8^\circ/\text{mm}$) in 15 m long, in other words, a very long twist transposition pitch. Therefore, we can assume as $L_{st} \gg l_c$, which brings the coupled behavior. However, we also study the other cases in order to see the general impact of twist transposition pitch of non-insulated twisted stacked cable on the behavior of magnetization. The analysis is done in 3D based on the model in Figure 3.4.

1. $L_{st} \gg l_c$ (long transposition pitch)
2. $L_{st} \ll l_c$ (short transposition pitch)
3. $L_{st} \approx l_c$ (intermediate transposition pitch)

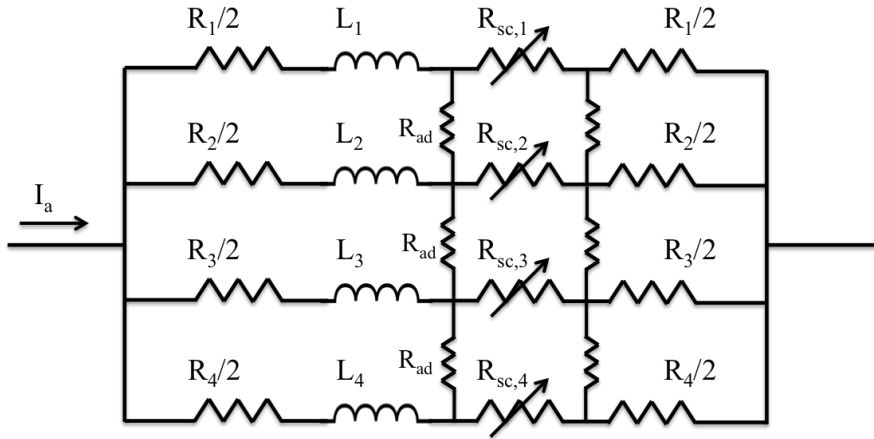


Figure 3.10 Equivalent electrical circuit of non-insulated twisted stacked cable.

$L_{st} \gg l_c$ (long transposition pitch foreseen in 46-turn HTS insert)

The non-insulated twisted stacked cable with very long straight part acts as the coupled behavior (large single-tape). It is the same behavior as previous model of non-insulated non-twisted stacked cable.

$L_{st} \ll l_c$ (short transposition pitch)

This case is expected when the transposition pitch is short enough, in other words, there is enough number of twist. In case of $\rho_{ad} = 300 \text{ n}\Omega \cdot \text{m}$, it derives $l_c = 1.6\text{m}$. We thus apply $L_{st} = 200 \text{ mm}$ ($\ll l_c$) to straight part in Figure 3.4. This

transposition pitch is equivalent to 30 twists per turn in 15 m long insert. Owing to its short transposition pitch, the cable acts as the non-coupled behavior shown in Figure 3.11 and Figure 3.12 when the vertical external field is uniformly applied all along the cable's length direction. Each tape carries the positive and negative currents and it shows net current equals to zero during the external field ramping. As the uniform vertical field is applied along the cable, the stacked cable experiences the parallel field at straight part and transverse field at 90° angles of twisted part. Thus, the boundary of $+J$ and $-J$ are changing at twisted part. The lowest J_e of the cable is at 90° angles where the transverse field is penetrated. During the ramp current mode, the transport current tends to flow into the outer tapes until they reach high load factor. This is because the field shielding to the inner tapes. Two outer tapes and two inner tapes have the same current owing to the partial transposition. From the end of the ramp current mode, the tapes start to exchange the current. Figure 3.12 is the case all joint resistances are the same. Thus, the current is equalizing to be 400 A. In case of a long dipole magnet, the homogeneous current distribution can be expected owing to sufficient twist transposition pitch (more than 30 twists per turn in 15 m long), even though the joint resistances are different. This will be an ideal behavior of twisted stacked cable for the HTS insert.

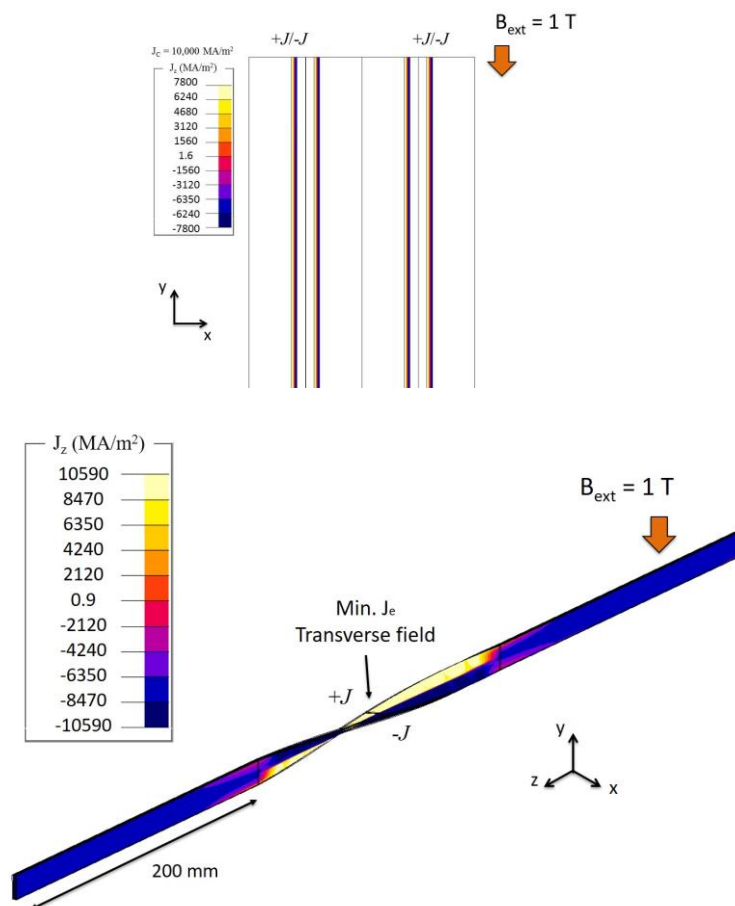


Figure 3.11 Distribution of current density of four-tape NI-TSC with short transposition pitch at one third of upper part (top) and its overall view at $B_{ext} = 1$ T and $I_a = 0$ A (bottom).

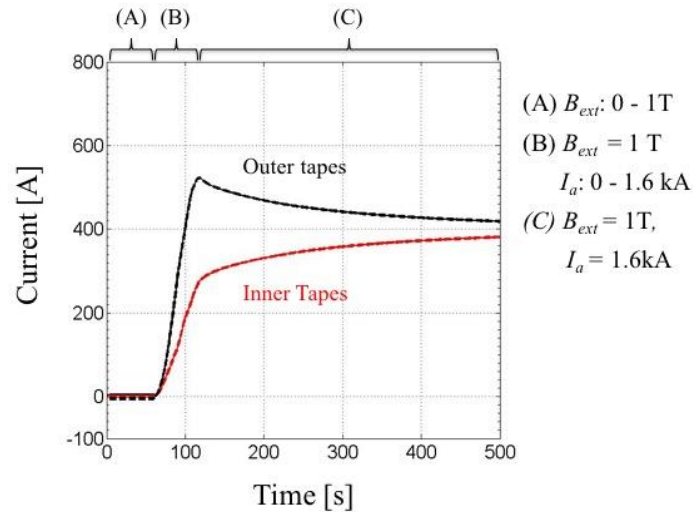


Figure 3.12 Current waveform of four-tape NI-TSC with short transposition pitch ($L_{st} \ll l_c$) B_{ext} : 0 – 1 T and I_a : 0 – 1.6 kA.

$L_{st} \approx l_c$ (intermediate transposition pitch)

When the transposition pitch is not short enough, the electromagnetic behavior takes place between two previous cases. We refer this as partially coupled behavior. We study with $L_{st} = 1$ m ($l_c = 1.6$ m) at $\rho_{ad} = 300$ n Ω ·m with the model in Figure 3.4. This transposition pitch is equivalent to 15 twists per turn in 15 m long insert. Figure 3.13 shows the current waveforms of non-insulated twisted stacked cable with intermediate transposition pitch at straight part, which is the furthest cut-plane from twisted part. During the external field ramping, the outer tapes act as partially coupled behavior, whose amount of coupling current is one third of its coupled behavior in Figure 3.8. On the other hand, the inner tapes show the non-coupled behavior, although their net currents are not zero. Thereafter, the current waveform during ramp current mode is similar to previous behavior as that of short transposition pitch except the very beginning of the ramp current mode.

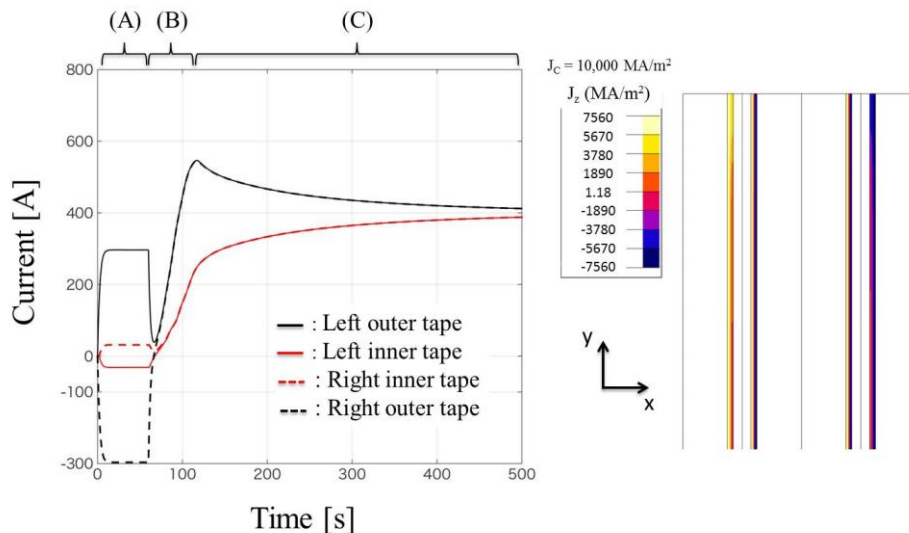


Figure 3.13 Current waveform of four-tape NI-TSC with intermediate transposition pitch (left) and distribution of current density at $B_{ext} = 1$ T and $I_a = 0$ A whose cross-section is furthest from twist (right).

Now, we explain the reason why the inner tapes do not have zero current during the external field ramping, although their distribution of current density shows the non-coupled behavior.

I. Coupled behavior in case for entire four-tape cable

As we have seen the behavior of non-insulated stacked cable in Figure 3.8, the coupling current starts to be induced from outer and then to inner tapes when the external field increases. But, the inner tapes have intermediate behavior before the external field penetrates. Despite the field penetration only into outer tapes, a very small current is induced in inner tapes caused by the coupling current of outer tapes. On top of that, this very small current in inner tapes has opposite polarity to coupling current of adjoining outer tape. This disappears when the external field penetrates inner tapes. Thus, the adjoining outer and inner tapes possess the same polarity of the coupling current at full penetration.

II. Non-coupled behavior in case for entire four-tape cable

As we have seen the behavior of non-insulated twisted stacked cable with short transposition pitch, all tapes in the stacked cable react the same during the external field ramping. Every tape carries no current but it possesses positive and negative current density, whose screening current circulates all along the tape.

III. Coupled behavior in case for outer tapes and non-coupled behavior in case for inner tapes

We consider when two former cases of coupled and non-coupled behaviors are intermixed in four-tape stacked cable. When the external field is exposed, the current principally increases in outer tapes, which is typical coupled behavior, while that of inner tapes remains zero, which is typical non-coupled behavior. However, one must know the large coupling current of outer tapes induces the currents in the inner tapes, which will not disappear because the inner tapes have the non-coupled behavior.

Thus, the coupling current of outer tapes during the external field ramping in Figure 3.13 induces the current in inner tapes, which act as the non-coupled behavior. At the beginning of the ramp current mode, the current of outer tapes has a sudden drop. This is because the coupling current substitutes to the screening current, which is the behavior of non-coupled case. In the end, only a few hundred amperes of the coupling current circulate the entire twisted stacked cable. One has to know the behavior of magnetization in outer tapes varies along the cable's length direction (Figure 3.14). Closer the cross-section to the twisted part, the smaller the coupling current in outer tapes is. For example, the coupling current decreases from 296 A at furthest part to 28A at nearest part from twisted part.

Short summary

The results of these analyses were in case of $\rho_{ad} = 300 \text{ n}\Omega \cdot \text{m}$, which is actual contact resistance between ReBCO tapes. When the ρ_{ad} gets smaller, the l_c gets shorter. This means the shorter transposition pitch, in other words, more number of transposition is required. However, the twist at straight part of dipole magnet is not practical due to the transverse field at twisted part and harmful impact on the field quality. Therefore, the non-insulated twisted stacked cable is not adequate for 46-turn HTS insert.

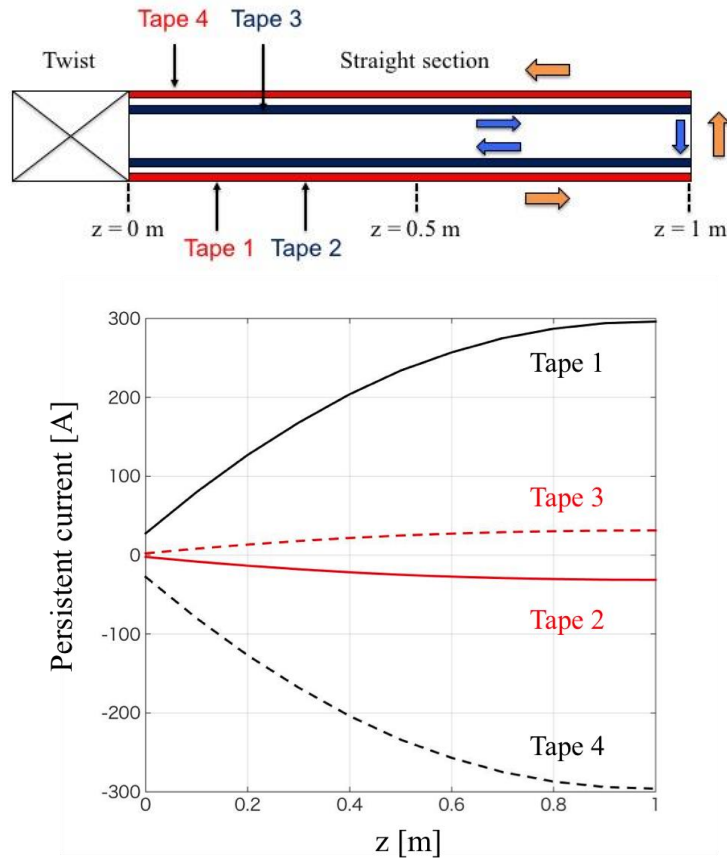


Figure 3.14 Distribution of coupling current in outer tapes and induced current in inner tapes along the cable's length direction at straight part starting from twisted part (L_{st} : 0 - 1 m).

3.1.5. Insulated twisted stacked cable

The insulated twisted stacked cable is impossible to exchange the current between the tapes in stacked cable; thereby all tapes act as the non-coupled behavior, which has already been seen in case of the non-insulated twisted stacked cable with short transposition pitch. All tapes thus carry zero net current during the field increases whose cross-section possesses $+J_C$ and $-J_C$. On the other hand, the current distribution strongly depends on the joint resistance R_i at the termination of dipole magnet (Figure 3.15).

$$R_{sc,i} = \frac{E_c}{I_c} \left(\frac{I_i}{I_c} \right)^{n-1} \cdot l \quad (3.2a)$$

$$I_a = \sum_{i=1}^{N_{tape}} I_i \quad (3.2b)$$

$$V_i = L_i \frac{dI_i}{dt} + \sum_{j \neq i}^{N_{tape}} M_{ij} \frac{dI_j}{dt} + (R_{sc,i} + R_i) I_i \quad (3.2c)$$

Where M_{ij} is the mutual inductance between the tapes. In general, the joint resistance is rather higher than the resistance of the superconductor R_{sc} . However, the cable unit length l in 15 m long 46-turn HTS insert is very long, e.g. $l = 200$ m in 1st double pancake, which brings high R_{sc} and may influence the current distribution.

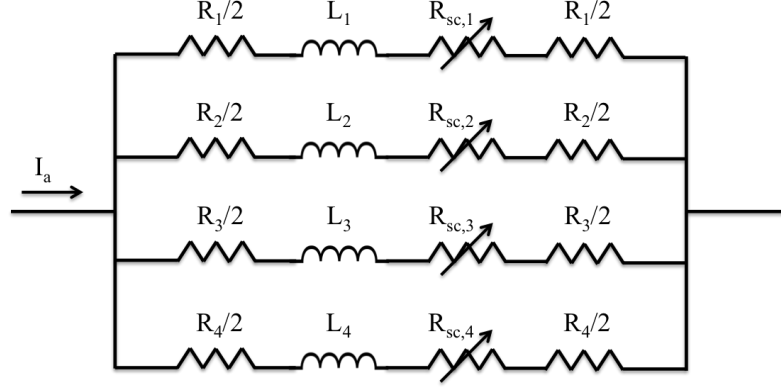


Figure 3.15 Equivalent electrical circuit of insulated twisted stacked cable.

The 3D analysis of over 200 m long stacked cable is impractical in terms of computational time. Therefore, we simulate the insulated twisted stacked cable in 2D analysis with the electrical circuit coupling. We model the upper half of 15 m long 46-turn HTS insert and the FRESKA2 LTS outsert (Figure 3.16). To save the computational time, only the innermost turn at 3rd layer is divided into twenty tapes. The tape only contains the superconducting layer whose size and characteristic are same as those of previous 3D models ($t_{sc} = 20 \mu\text{m}$, $w_{sc} = 4 \text{ mm}$, $J_C = 10,000 \text{ MA/m}^2$ and n -value = 20). We place the air region between the superconducting layers, which acts as the insulation.

Now, all tapes are assigned to the circuit components to represent the twisted stacked cable as the same way in § 3.1.2 ‘Electrical circuit coupling’. As the cable is twisted for half turn in magnet ends, the innermost tape 1 at right side of the magnet in Figure 3.16 is transposed to the outermost tape 1’ at left side, whereas the outermost tape 20 at right is transposed to the innermost tape 20’ at left. We assign the conductors $R_{sc,i}$ in electrical circuit coupling to proper tapes:

| Left | Right |
|---|---|
| $R'_{sc,1} \leftrightarrow \text{tape } 1'$ | $R_{sc,1} \leftrightarrow \text{tape } 1$ |
| $R'_{sc,2} \leftrightarrow \text{tape } 2'$ | $R_{sc,2} \leftrightarrow \text{tape } 2$ |
| $R'_{sc,19} \leftrightarrow \text{tape } 19'$ | $R_{sc,19} \leftrightarrow \text{tape } 19$ |
| $R'_{sc,20} \leftrightarrow \text{tape } 20'$ | $R_{sc,20} \leftrightarrow \text{tape } 20$ |

In addition, we add the different joint resistance R_i to each tape:

$$R_i = R + \alpha_i R \quad (3.3)$$

Where R is the common resistance and α is the variation of the joint resistance chosen randomly in the range of 0 – 0.5. According to the Eq. (3.2c), the current distribution of the cable is determined by the interrelationship between joint resistance R_i and resistance of superconductor $R_{sc,i}$. For example, when R_i is rather higher than $R_{sc,i}$, the current of each tape will strongly depend on the joint resistance.

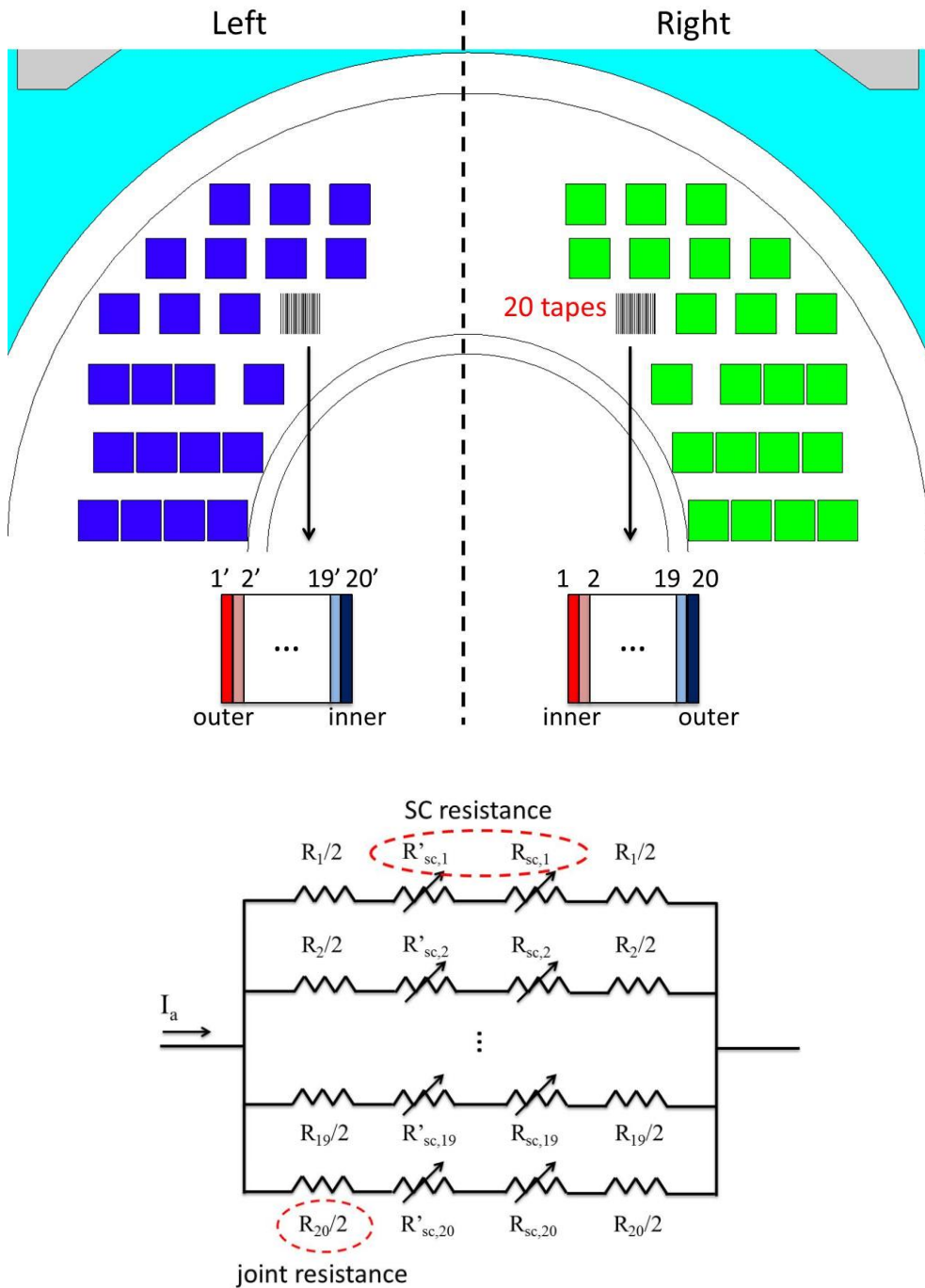


Figure 3.16 Upper half of 15 m long 46-turn HTS insert whose innermost block at 3rd layer is divided into twenty tapes (top). Every tape is assigned to component of electrical circuit coupling $R_{sc,i}$ and $R'_{sc,i}$ (bottom).

As we have seen in Figure 3.1, a 1 T of background field of LTS outsert is first applied and then a 10.4 kA of transport current is injected to all turns. The 44-turns except the innermost turn at 3rd layer will have homogeneous current distribution. In case of an ideal current distribution, every tape possesses 540 A, which is 65% load factor of the tape I/I_C . This derives $R_{sc,i} = 1 \text{ n}\Omega$ in 30 m cable length. We simulate two different common resistances $R = 10$, and $1000 \text{ n}\Omega$.

When the joint resistance R is close to $R_{sc,i}$ of ideal case, the current of the cable gets more homogenized (Figure 3.17). In case of $R = 10 \text{ n}\Omega$, every two tapes in the cable that are transposed have the same current waveform during the ramp current mode. The current starts to depend on the joint resistance during DC mode resulting maximum current difference about 40 A. When $R = 1000 \text{ n}\Omega$, the current is simply determined by the joint resistance even during the ramp current mode. It brings the current difference about 160 A. In reality, the joint resistance in 15m long HTS insert is rather bigger than that of superconductor ($R \gg R_{sc}$). Moreover, the n -value can be over 30, which makes R_{sc} smaller. Therefore, the current distribution becomes as in case of $R \gg R_{sc}$, which means it is simply determined by the joint resistance. Hence, to achieve uniform current distribution, almost perfect soldering is required at the joint termination of dipole magnet, which is not feasible.

(A) $B_{ext}: 0 - 1\text{T}$, (B) $B_{ext} = 1\text{T}$ and $I_a: 0 - 10.4 \text{ kA}$, (C) $B_{ext} = 1\text{T}$ and $I_a = 10.4 \text{ kA}$

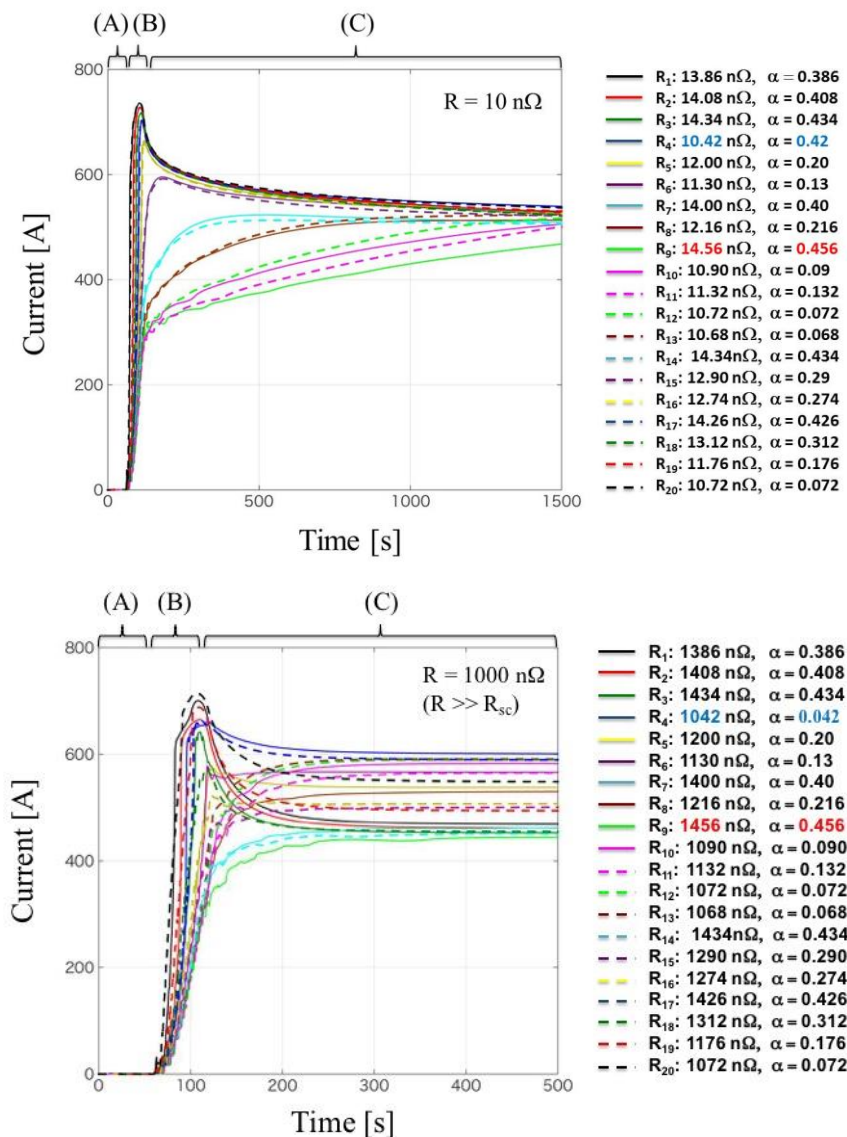


Figure 3.17 Current waveform of insulated twisted stacked cable at innermost turn of 3rd layer in 46-turn HTS insert. $R = 10 \text{ n}\Omega$ (top) and $1000 \text{ n}\Omega$ (bottom).

3.1.6. Influence of magnetization on field quality

A field quality including the magnetization-induced harmonics ($\leq 50 \cdot 10^{-4} B_1$) is a significant problem for the superconducting accelerator magnets especially the HTS insert using a ReBCO stacked cable. It is important to study the impact in case the stacked cable acts as the non-coupled and coupled behaviors. The numerical setup is the same as that of insulated twisted stacked cable in Figure 3.16 except all 46-turn are divided into twenty tapes. As we have mentioned in §3.1.2 ‘Meshing’, only one single mesh element is applied on the 20 μm thickness of superconducting layer, which is ten times thicker than actual thickness. This is expected to bring similar behavior as actual case.

Due to huge computational time (about three weeks), we could only apply up to a 1T of external field instead of a 13 T, which is the operating field of the FRESCA2 LTS outsert. This will influence the results of the field quality including the magnetization-induced harmonics, whose values are divided by central field B_1 .

$$b_n = \frac{10^4 B_n(r_0)}{B_1} \quad (3.4)$$

Therefore, the field harmonics listed in Table 3.3 will be different.

Table 3.3
Field quality including magnetization-induced harmonics in case of coupled and non-coupled behaviors under 1T background field of FRESCA2 LTS outsert

| Parameter | Coupled behavior | Non-coupled behavior |
|-----------------------|------------------|----------------------|
| Total field harmonics | 77.3 unit | 31.9 unit |
| Hexapole B_3 | -76.3 unit | 31.7 unit |
| Decapole B_5 | 9.62 unit | -4.03 unit |
| Tetradecapole B_7 | -7.79 unit | -0.33 unit |
| Octadeca B_9 | 0.94 unit | -0.01 unit |

Coupled behavior (non-insulated twisted stacked cable with long transposition pitch)

A 1 T of background field is not sufficient to fully penetrate twenty-tape stacked cable. Therefore, the central field generated by the coupling current in HTS insert is only about a few tens of milli-Tesla, which should increase up to more than hundreds of milli-Tesla. This will also increase the field harmonics of $B_3 = -76.3$ units, $B_5 = 9.62$ units and $B_7 = -7.79$ units more and more, which is already higher than the required value ($\leq 50 \cdot 10^{-4} B_1$). Therefore, the coupled behavior seen in non-insulated twisted stacked cable with long transposition pitch is not appropriate for 46-turn HTS insert.

Non-coupled behavior (insulated twisted stacked cable)

A 1 T of background field is enough to fully penetrate the insulated twisted stacked cable, which acts as the non-coupled behavior. The HTS insert generates a few hundreds of milli-Tesla of additional central field inside the beam aperture. It also causes undesired field harmonics of $B_3 = 31.7$ units, $B_5 = -4.03$ units and $B_7 = -0.33$ units, which are below than the required value ($\leq 50 \cdot 10^{-4} B_1$). These values are expected to reduce if the background field gets $B_1 = 13$ T according to the Eq. (3.4).

3.1.7. Summary of non-insulated and insulated twisted stacked cable

The non-insulated and insulated twisted stacked cables forming a straight conductor have been studied with regard to the magnetization and current distribution (Table 3.4). However, the current distribution can be different if the stacked cable is formed into a U-turn coil. For example, the current tends to flow into the inner tapes of the non-twisted stacked cable whose impedances are smaller.

Yet the non-insulated twisted stacked cable with short transposition pitch is the best solution for the HTS insert, a very long transposition pitch is foreseen in 46-turn HTS insert. Therefore, both non-insulated and insulated twisted stacked cables cannot meet the cable's requirements: low magnetization (non-coupled behavior) and homogeneous current distribution. Therefore, new solution is necessity for the twisted stacked cable with a very long twist transposition pitch.

Table 3.4
Summary of non-insulated and insulated twisted stacked cable (NI-TSC/ I-TSC)

| Phenomenon | NI-TSC | | I-TSC |
|---------------------------|-------------|-----------------------------|-----------------------------|
| | Short T_P | Long T_P | |
| Straight conductor | | | |
| Magnetization | Non-coupled | Fully-Coupled | Non-coupled |
| Local current exchange | Yes | Yes | None |
| HTS insert coil | | | |
| Magnetization | Non-Coupled | Coupled | Non-coupled |
| Local current exchange | Yes | Yes | None |
| Current distribution | Ideal case | More current in inner tapes | Depends on joint resistance |

T_P : transposition pitch

3.1.8. Partially-insulated twisted stacked cable

The non-insulated and insulated twisted stacked cables with long transposition pitch foreseen in 15 m long 46-turn HTS insert are impossible to achieve both low magnetization and uniform current distribution. However, these cables still bring positive aspect:

- Non-insulated twisted stacked cable: Local current exchange
- Insulated twisted stacked cable: Low magnetization (non-coupled behavior)

We thus propose a partially-insulated twisted stacked cable. Its concept is to take both advantages of non-insulated and insulated solutions. To adapt this concept into 46-turn HTS insert with very long transposition pitch, one must carefully choose where to locate the non-insulated and insulated parts based on the electromagnetic behaviors studied in previous sections. At first, the straight part of HTS insert must possess a good field quality. Hence, it is insulated, which brings a non-coupled behavior. Secondly, the twisted part needs to be insulated. This is because the non-insulated HTS insert with long transposition pitch results in the whole magnet behaving as coupled behavior, which gets opposed to first item. At last, the other parts of HTS insert become non-insulated to allow the current exchange. Hence, the partially-insulated HTS insert is designed as shown in Figure 3.18. The cable is insulated at straight part and transposition side of magnet ends where the twists are applied. On the other hand, the turn-to-turn transition side of magnet end is non-insulated, which is farthest from twisted part.

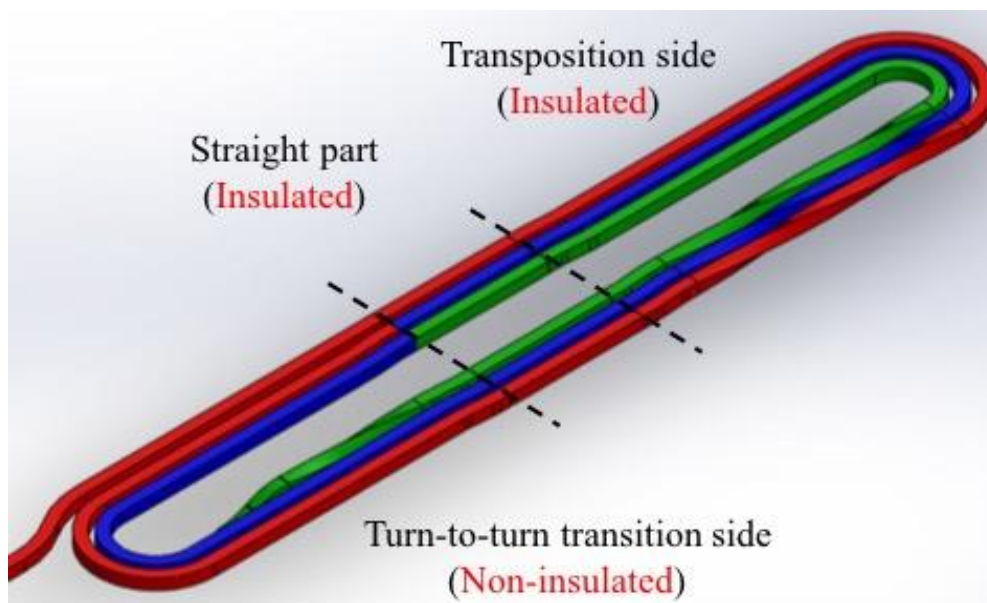


Figure 3.18 Twisted stacked/ block-type HTS insert (3-turn 1st racetrack coil in 46-turn HTS insert) using the partially-insulated solution.

We study the electromagnetic behavior of partially-insulated HTS insert using 2D and 3D FLUX[®]. At first, due to an asymmetric structure along cable's length direction of partially-insulated twisted stacked cable, the magnetization behavior is inevitable to analyze in 3D. Then, when once its behavior at straight part is verified, we implement this partially-insulated solution in 2D analysis with an equivalent electrical circuit coupling to study the field quality of 46-turn HTS insert.

As we have mentioned, in 3D analysis, it requires a simplified model of partially-insulated solution, which is formed in a straight conductor instead of a U-turn-coil due to complicated meshing structure and huge computational time. We thus study via two simplified models shown in Figure 3.19 by unfolding the 3-turn racetrack coil in Figure 3.18.

1. One non-insulated part interposed by two insulated straight + twisted parts
2. Two non-insulated parts interposing insulated straight + twisted parts

The objective is to see qualitatively the behavior of magnetization at the straight part. The first preliminary model is to check the capability of FLUX[®] for partially-insulated solution. Qualitatively, this model is expected to bring the non-coupled behavior at insulated part and the coupled behavior at non-insulated part. On the other hand, the second model has two non-insulated straight parts at both ends of straight conductor interposing the insulated straight and twisted parts. This may cause the entire straight conductor acting as the coupled behavior (large single-tape).

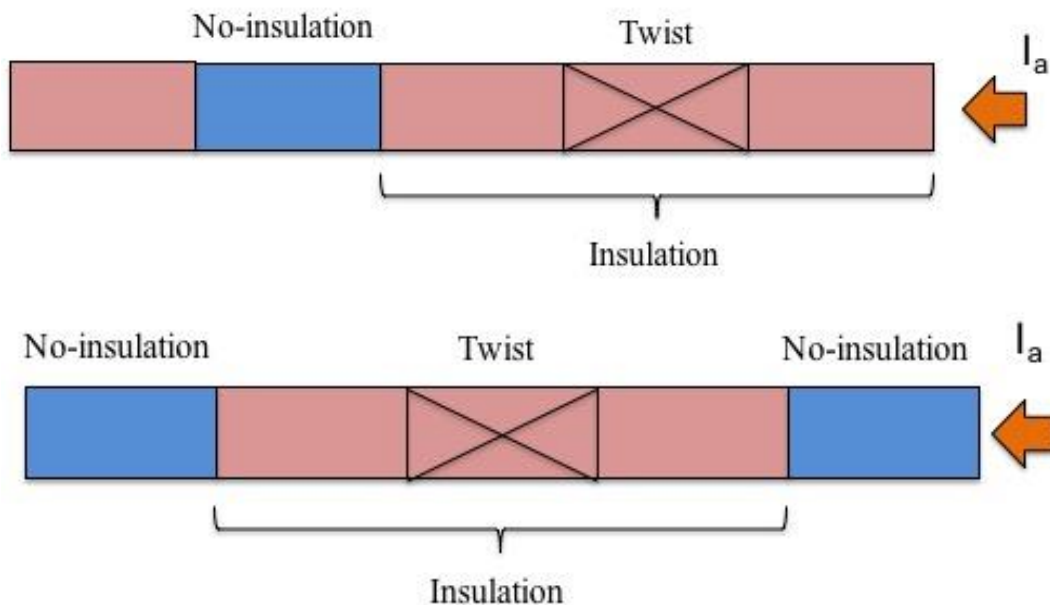


Figure 3.19 Simplified model for 3D partially-insulated twisted stacked cable based on Figure 3.18: One non-insulated part interposed by two insulated straight + twisted parts (top) and Two non-insulated parts interposing insulated straight + twisted parts (bottom).

Preliminarily analysis: One non-insulated part interposed by two insulated straight + twisted parts

Figure 3.20 shows the four-tape partially-insulated twisted stacked cable, which is composed of one non-insulated part interposed by two insulated parts. Besides, we add the joint resistance R_j at both ends of conductor. The length of non-insulated part L_{non} is between 0.2 – 1 m, which is the total cable unit length per turn at turn-to-turn transition side in 46-turn HTS insert. In this analysis, we only expose a 1T of external magnetic field uniformly all along the cable's length direction.

During the external field ramping, entire insulated parts act as the non-coupled behavior in all conditions ($L_{non} = 0.2 - 1$ m and $\rho_{ad} < 300$ n $\Omega \cdot$ m). On the other hand, the behavior of the magnetization at non-insulated part depends on the L_{non} and ρ_{ad} , which is the same behavior as § 3.1.4 ‘Non-insulated twisted stacked cable with different transposition pitch’. The smaller the ρ_{ad} is and the longer the L_{non} is; it tends to act as the coupled behavior. For example, the $\rho_{ad} = 2$ n $\Omega \cdot$ m at $L_{non} = 1$ m is small enough to make entire non-insulated part to behave as the coupled behavior (large single-tape) shown in Figure 3.21. Thus, the coupling current only circulate at the non-insulated part shown as arrow in figure.

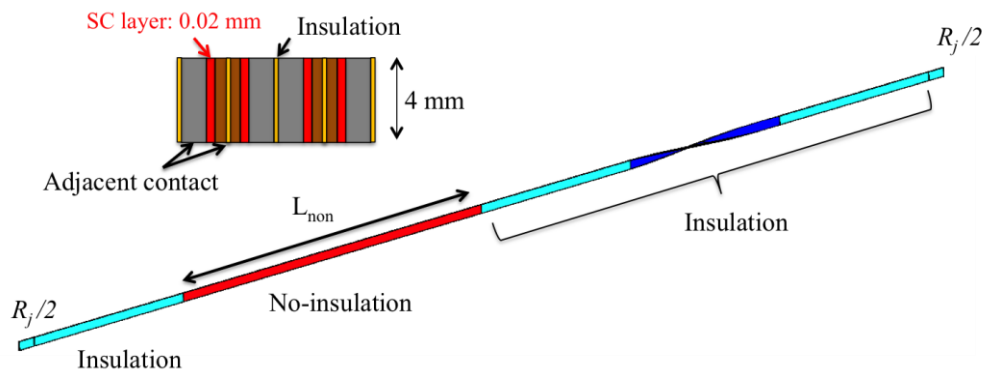


Figure 3.20 3D four-tape partially-insulated twisted stacked cable: One non-insulated part interposed by two insulated straight + twisted parts.

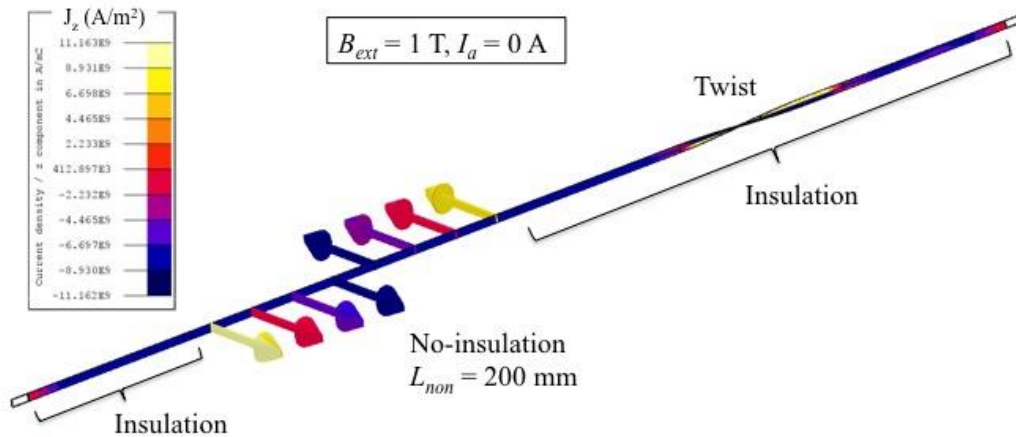


Figure 3.21 Distribution of current density of four-tape partially-insulated twisted stacked cable under uniform $B_{ext} = 1$ T. The arrows show the flow of coupling current at non-insulated part.

Two non-insulated parts interposing insulated straight + twisted parts

Figure 3.22 shows the four-tape partially-insulated twisted stacked cable, which is composed of two non-insulated straight parts L_{non} interposing long insulated straight and twisted parts. Besides, we add the joint resistance R_j at both ends of conductor. In this analysis, we selected $L_{insu} = 1$ m, although the L_{insu} becomes about 15 m in reality. This is because to save a computational time. On the other hand, the other parameters are set to be $L_{non} = 1$ m and $\rho_{ad} < 2$ n Ω ·m, which is expected to bring the coupled behavior at non-insulated part. The operating condition is exactly same as the previous model.

During the external field ramping, the non-insulated part acts as the coupled behavior, while the insulated part acts as the non-coupled behavior (Figure 3.23). One can see the coupling current shown as arrow in figure is only circulating the non-insulated parts. In addition, only a few hundreds milli-ampere of coupling current passes the insulated straight and twisted parts. This means the straight part of the partially insulated HTS dipole insert will have the non-coupled behavior, which gives low magnetization.

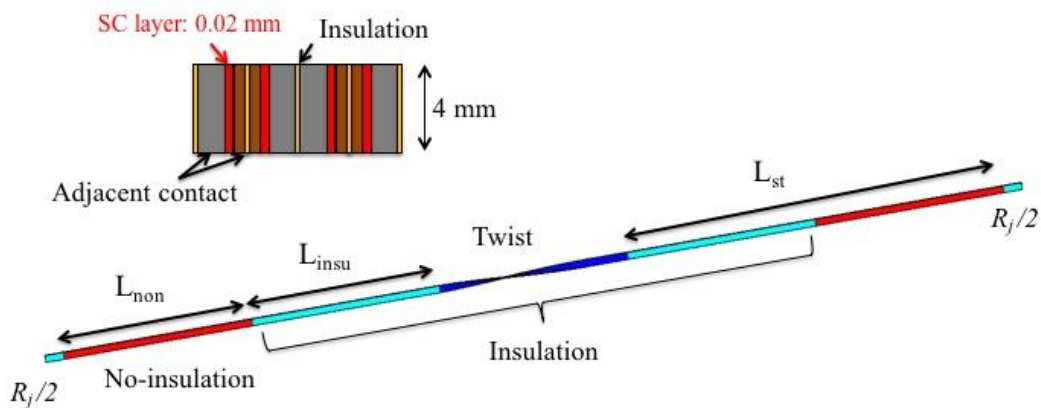


Figure 3.22 3D four-tape partially-insulated twisted stacked cable: Two non-insulated parts interposing insulated straight + twisted parts.

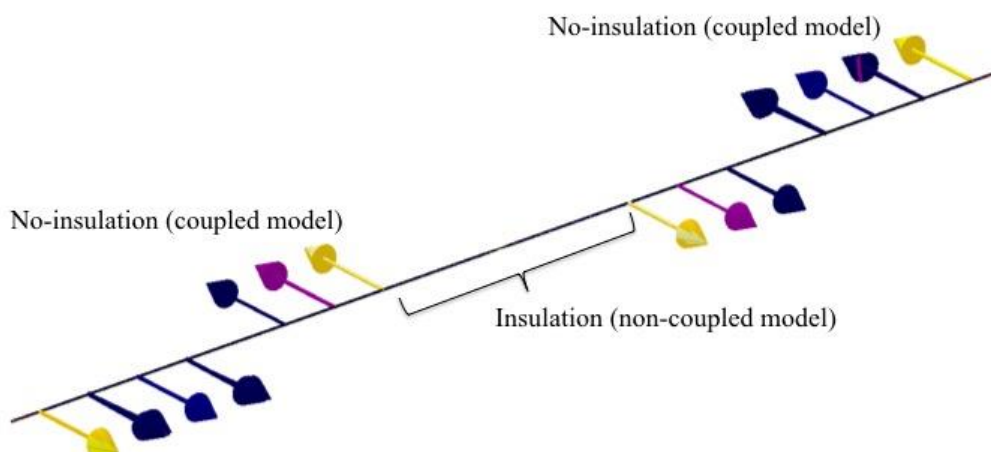


Figure 3.23 Distribution of current density of four-tape partially-insulated twisted stacked cable under uniform $B_{ext} = 1$ T. The arrows show the flow of coupling current at non-insulated part.

Current distribution of partially-insulated solution

The current distribution of partially-insulated solution is studied in 2D due to enormous computational time in 3D. We model the upper half of 15 m long 46-turn HTS insert, which is same as Figure 3.16 of ‘Insulated twisted stacked cable’ except the resistance R_{ad} equivalent to adjacent contact between the tapes at the non-insulated part is added to the electrical circuit coupling (Figure 3.24).

$$R_{ad} = \rho_{ad} \frac{t_{sc}}{w_{sc} L_{non}} \quad (3.5)$$

Where $t_{sc} = 20 \mu\text{m}$ and $w_{sc} = 4 \text{ mm}$. This will allow studying the current exchange of partially-insulated solution at the non-insulated part, which is at turn-to-turn transition side of magnet ends of 46-turn HTS insert.

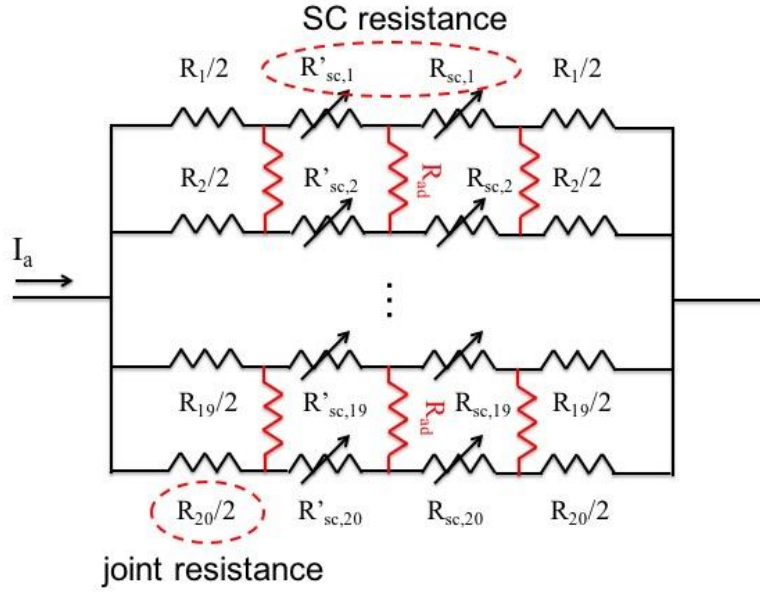


Figure 3.24 Equivalent circuit of twenty-tape partially insulated twisted stacked cable with adjacent resistance R_{ad} .

In case of the insulated twisted stacked cable, the current distribution at normal operation is simply determined by the joint resistance R_i . The maximum difference of the current between the tapes in stacked cable can become over 100 A. So, the objective is to see how much it can minimize this difference by the local current exchange across R_{ad} . We thus examine three cases:

1. $\rho_{ad} = 2 \text{ n}\Omega \cdot \text{m}$ and $L_{non} = 1 \text{ m}$
2. $\rho_{ad} = 300 \text{ n}\Omega \cdot \text{m}$ and $L_{non} = 1 \text{ m}$
3. $\rho_{ad} = 300 \text{ n}\Omega \cdot \text{m}$ and $L_{non} = 200 \text{ mm}$

When the resistivity of adjacent contact ρ_{ad} is small enough as well as the length of non-insulated part L_{non} is long enough, the homogeneous current distribution is achieved. And, all tapes carry 520 A of ideal case in 46-turn HTS insert. The first case fits the above condition, which brings almost 520 A in all tapes (Table 3.5 and Figure 3.25). However, the other two cases are not able to provide enough current exchange

Table 3.5
Current of twenty tapes in stacked cable at the end of 2D analysis

| Tape | R_i [n Ω] | Insulated cable | $\rho_{ad} = 2 \text{ n}\Omega \cdot \text{m}$ | | $\rho_{ad} = 300 \text{ n}\Omega \cdot \text{m}$ | |
|------|------------------------|--------------------|--|-------------------------|--|----------------------------|
| | | | $L_{non} = 1 \text{ m}$ | $L_{non} = 1 \text{ m}$ | $L_{non} = 200 \text{ mm}$ | $L_{non} = 200 \text{ mm}$ |
| 1 | 1386 | 468.8 A | 522.5 A | 503.1 A | 473.1 A | |
| 2 | 1408 | 461.3 A | 521.9 A | 507.5 A | 482.7 A | |
| 3 | 1434 | 452.6 A | 521.5 A | 517.2 A | 508 A | |
| 4 | 1042 | 600.9 A | 520.8 A | 533.3 A | 558 A | |
| 5 | 1200 | 537.7 A | 520.1 A | 526.2 A | 535.9 A | |
| 6 | 1130 | 566.6 A | 519.4 A | 521.9 A | 527.5 A | |
| 7 | 1400 | 461.9 A | 518.9 A | 515.6 A | 504.8 A | |
| 8 | 1216 | 530.2 A | 518.5 A | 515.7 A | 506.1 A | |
| 9 | 1456 | 444.5 A | 518.3 A | 518.5 A | 508.8 A | |
| 10 | 1090 | 582.6 A | 518.3 A | 528.2 A | 540.6 A | |
| 11 | 1132 | 565.6 A | 518.3 A | 532.3 A | 546.5 A | |
| 12 | 1072 | 589.6 A | 518.4 A | 536.8 A | 557.7 A | |
| 13 | 1068 | 591.1 A | 518.7 A | 534 A | 552.4 A | |
| 14 | 1434 | 450.5 A | 518.9 A | 522 A | 515.2 A | |
| 15 | 1290 | 500.9 A | 519.3 A | 517.1 A | 507.6 A | |
| 16 | 1274 | 507.4 A | 519.9 A | 517 A | 515.1 A | |
| 17 | 1426 | 589.9 A | 520.6 A | 521.2 A | 537.9 A | |
| 18 | 1312 | 454.9 A | 521.3 A | 512.3 A | 507.4 A | |
| 19 | 1176 | 494.3 A | 521.8 A | 509.5 A | 502.7 A | |
| 20 | 1072 | 548.3 A | 522.3 A | 510.7 A | 512.2 A | |

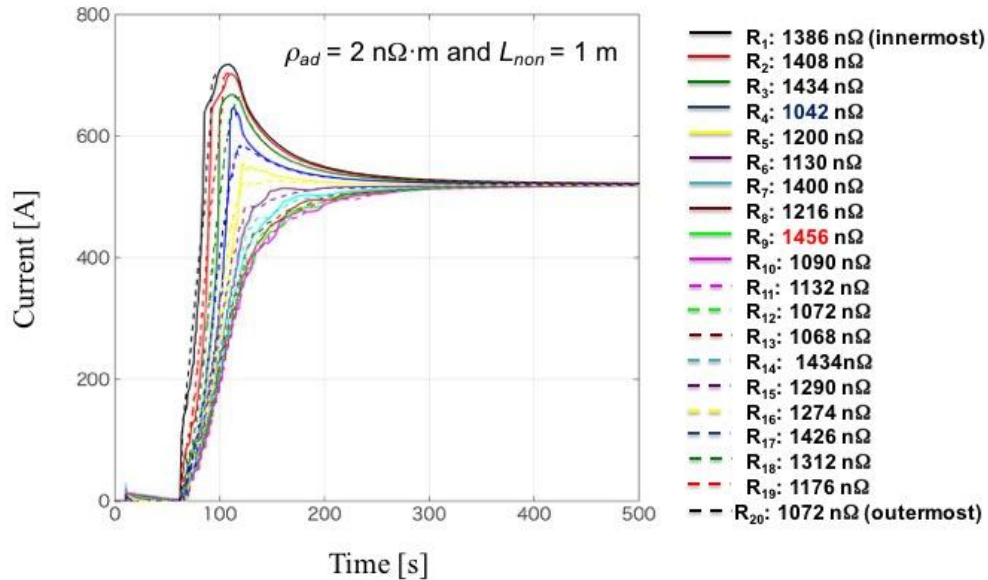


Figure 3.25 (a) Current waveform of twenty-tape partially-insulated twisted stacked cable at innermost block of 3rd layer in 46-turn HTS insert at $\rho_{ad} = 2 \text{ n}\Omega \cdot \text{m}$ and $L_{non} = 1 \text{ m}$

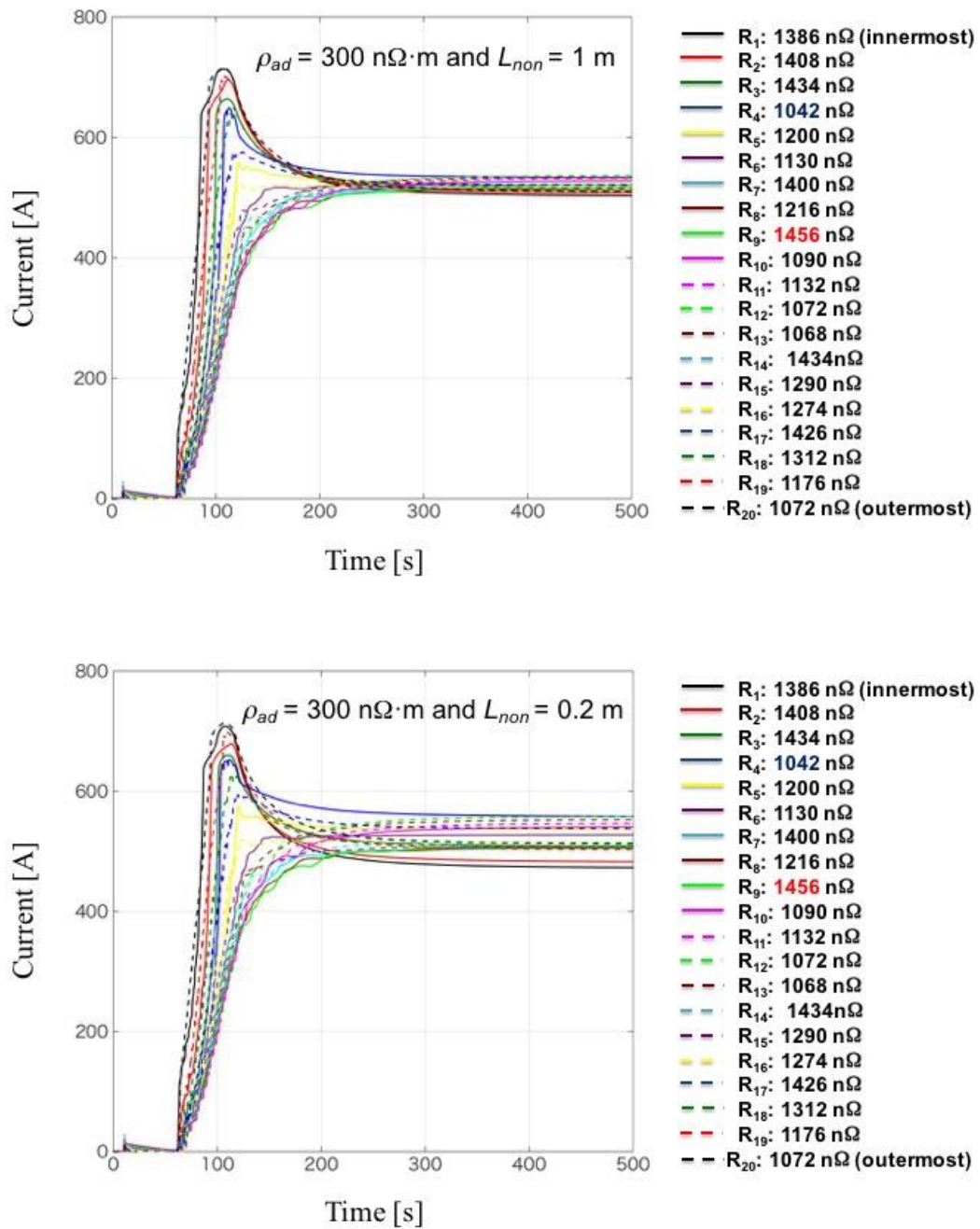


Figure 3.25 (b) Current waveform of twenty-tape partially-insulated twisted stacked cable at innermost block of 3rd layer in 46-turn HTS insert at $\rho_{ad} = 300 \text{ n}\Omega \cdot \text{m}$ and $L_{non} = 1 \text{ m}$ (top) and $\rho_{ad} = 300 \text{ n}\Omega \cdot \text{m}$ and $L_{non} = 200 \text{ mm}$ (bottom).

Summary: Partially-insulated twisted stacked cable

The partially-insulated twisted stacked cable is numerically analyzed in certain condition, which experiences a 1 T of uniform vertical magnetic field along the cable's length direction. It is the best solution for high performance accelerator magnets, which has the low magnetization and possible to exchange the current between the tapes. It takes both advantages of non-insulated and insulated cable, which are non-coupled behavior at straight part of dipole magnet and homogeneous current distribution at transposition side in magnet ends. One has to know there is a problem to make the partially-insulated cable. It will be a challenging to non-insulate only the magnet ends at turn-to-turn transition side in magnet ends. One of the solutions is to interpose high resistive layer between superconducting tapes instead of the insulation, which remains the non-coupled behavior at straight part. Moreover, to ensure the good current distribution, the resistive layer is only added between the face-to-face boundary of $F^2-B^2-F^2$ configuration.

3.2. Experiment of current distribution

We simulated the behavior of magnetization and the current distribution for various twisted stacked cable. It proved that the partially-insulated twisted stacked cable is the most appropriate solution to achieve high performance in twisted stacked/block-type HTS insert. However, most of the numerical analysis especially in 3D has been done in a straight conductor instead of a 1-turn coil due to the complexity in meshing. Moreover, it is impossible to see its long-term behavior. Therefore, we use an experimental approach to see the current distribution of a half U-turn coils of four-tape twisted stacked cable in long-term.

3.2.1. Experimental setup

Fabrication of the twisted stacked cable with conductor terminations

In our experiment, we use the 2.1 m long four-tape non-insulated stacked cable using a YBCO tape from SuperPower®, whose width and thickness are 4 and 0.1 mm. Its critical current and n -value at 77 K in self-field are 110 A and 35, respectively. The tapes are stacked one directly on top of the others with a face-to-back configuration. They are then tied up using heat shrinkable tube and kapton tape to make a good contact between the YBCO tapes. Each 5 cm at both ends of conductor is used for the termination, which gives 2 m available cable length. In termination, we use the copper block in which all tapes are soldered. It is expected to bring similar joint resistance in all tapes compared to solder the tape individually or to pressure mechanically the stacked cable from both sides. In the copper block, there is an 8 mm aperture hole with 5 cm depth. It is to insert four tapes and a 6 mm aperture copper rod (Figure 3.26). At first, the stacked tapes are fixed to the copper rod; each two tapes at both sides. This allows every tape to have a contact with the copper part. It will help to conduct the transport current into the tapes. While the soldering process, the hole in the copper block is filled up with the tin solder, which is heated up to 180 C°. Then, the stacked cable and copper rod are put inside the hole where the tin is already melted. In the end, the copper block is quickly cooled down in order not to damage the YBCO tape.

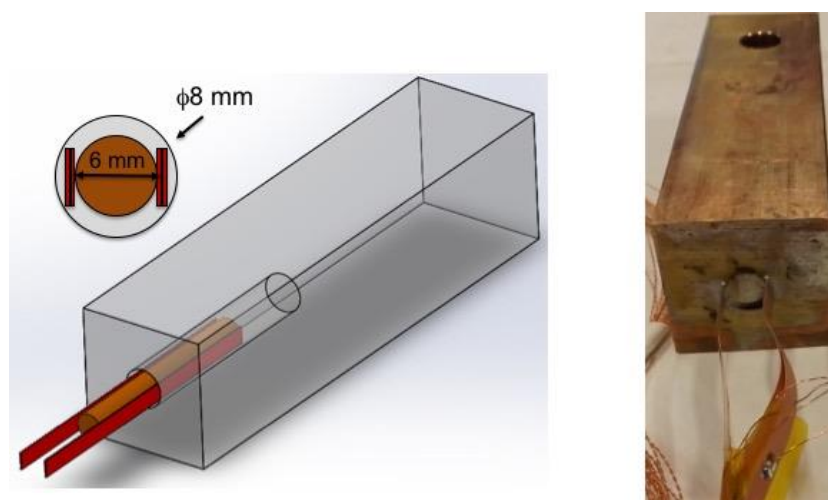


Figure 3.26 Schematic illustration (left) and actual model (right) of copper block termination with four YBCO tapes and copper rod.

U-turn coil structure

The four-tape stacked cable is wound onto the winding support, which is formed into a half U-turn coil (Figure 3.27). The winding support is made up of four main parts: straight, twist, winding head and measurement. The winding of half U-turn coil starts with a 150 mm or 300 mm half twist. It then continues to the straight part and winding head. In the end, the stacked cable is separated into four tapes at measurement part, which is 1.8 m far from the twisted part. At measurement part, the hall sensor ‘TOSHIBA: THS188’ and the pick-up coil are placed on top of each tape to measure the current in each tape. The hall sensor captures the flux density B and then extracts the voltage V based on its B - V curve. On the other hand, the pick-up coil shows the electromotive force derived from the rate of change of flux density passing the cross-area S of pick-up coil.

$$E_i = \frac{d\phi_i}{dt} = \frac{dB_i}{dt} S \quad (3.6)$$

Then one can calculate the current in each tape by knowing the precise location of four tapes, hall sensor and pick-up coil.

$$B_i \propto f(I_1, I_2, I_3, I_4) \quad (3.7)$$

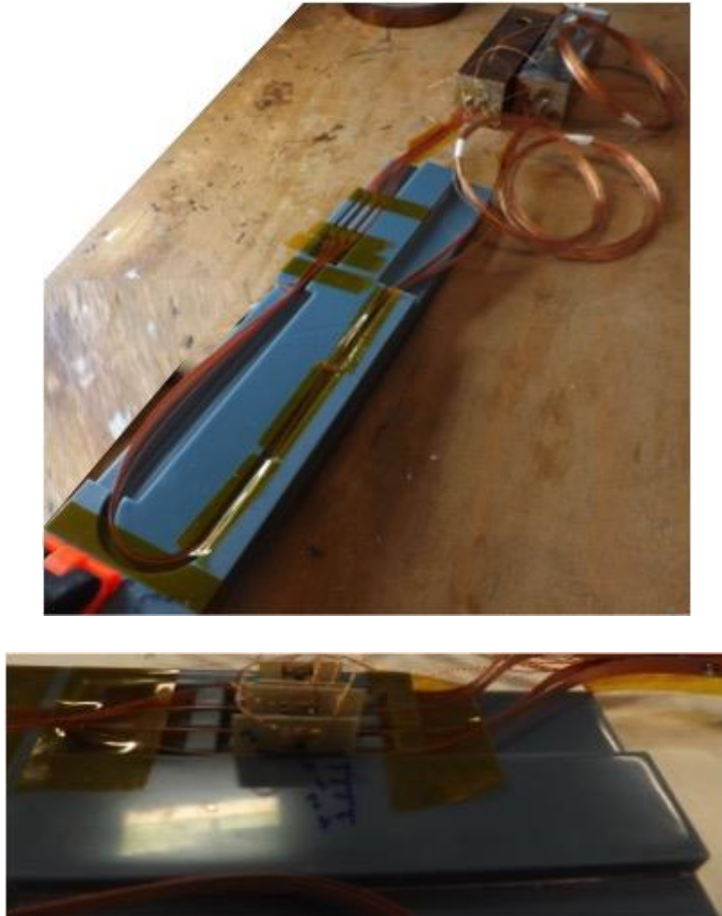


Figure 3.27 Half U-turn coil using 2 m long twisted stacked cable (top) and measurement section with the hall sensor and the pick-up coil (bottom).

Operating condition and measurement setup

The objective of this measurement is to see the current distribution of four-tape in long-term, which takes a huge computational time in FLUX[®]. The twisted stacked cable with the winding support is operated at 77 K in liquid nitrogen bath without any external field. We inject a 250 A of maximum transport current from the current source, which is around 55% load factor of the cable. The transport current profiles are qualified into a very steep ramp-up and ramp-down current mode and the long-term DC stable mode (Figure 3.28). It is controlled by the arbitrary waveform generator.

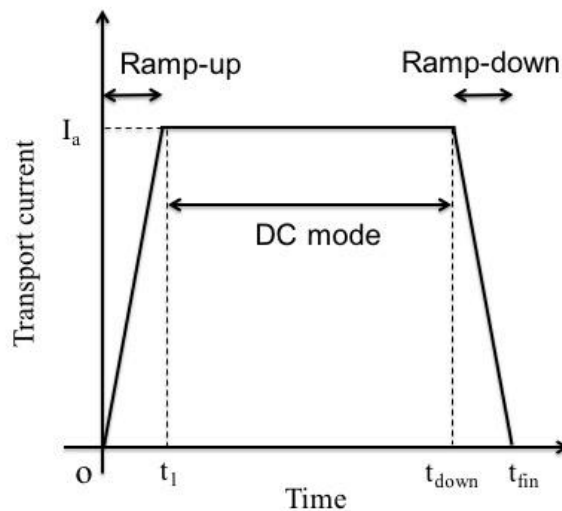


Figure 3.28 Transport current profiles.

The hall sensor 'TOSHIBA: THS188' is calibrated at 77 K with a conventional tape. The voltage of hall sensor well recreates the original current in the tape in short-term test. However, some of them causes significant error in long-term test in case that more than a minute. This is because this sensor is not expected to use in low temperature condition such as 77 K. For this reason, we measure the current only by the pick-up coil.

Due to the small cross-area and a few numbers of turn in the pick-up coil, its voltage is measurable when the rate of change of magnetic flux is fast enough. Therefore, it is not able to detect anything during the DC mode, whose current exchange between the tapes is small. On the contrary, it can measure during ramp-up and ramp-down current modes. Hence, the measurement of pick-up coil takes several steps to accomplish the data of long-term test. Figure 3.29 shows the example of the current waveform in one of the four-tape during time duration t , whose profiles are the current I_1 at t_1 etc. To measure the current change of ΔI_{12} and ΔI_{23} , we ramp down a transport current after the duration of t_2 and t_3 , respectively. This allows the pick-up coil to measure the current I_2 and I_3 . In the same manner, we obtain the whole current profile of four-tape stacked cable.

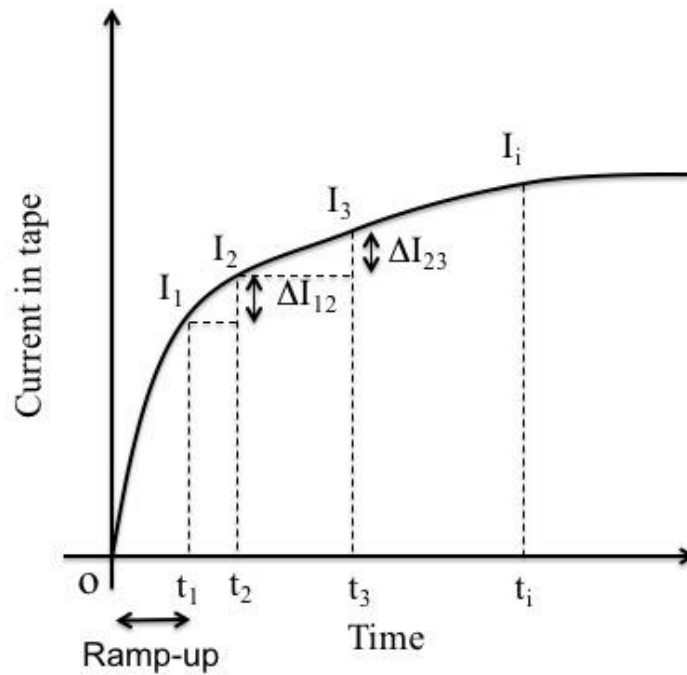


Figure 3.29 Example of the current waveform in one of the tapes.

3.2.2. Current distribution at 77 K in self-field

A transport current with 25 or 2.5 A/ms of the ramp rate is injected into the non-insulated twisted stacked cable. This allows the pick-up coil to detect the current. Figure 3.30 shows the current waveform of the transport current at 25 A/ms of the ramp rate and the four tapes, which is 1.8 m far from the twisted part. The innermost and outermost tapes (tape 1 and 4) as well as the two middle tapes (tape 2 and 3) have the same current during ramp-up current mode owing to the twist transposition. Then, the current saturates at the end of the ramp-up current mode depending on the joint resistance at the copper block termination. We tested the same ramp-up current for several times to see the reproducibility, which has showed the same current behavior. For non-insulated cable, the current can be exchanged between the tapes during DC current mode, which is unobservable by the pick-up coil. Therefore, we applied the ramp-down current mode at 30 seconds, 1, 3, 5, 8, 10, 15 and 20 minutes after DC mode. The current in the cable indeed varies during the DC mode and it is slightly increasing at the inner tapes 1 and 2 (Figure 3.31). This behavior can be seen when the transposition pitch is not enough (see § 3.1.4 ‘Non-insulated twisted stacked cable’). Thus, the non-insulated twisted stacked cable with a very long transposition pitch is not adequate for our 46-turn HTS insert.

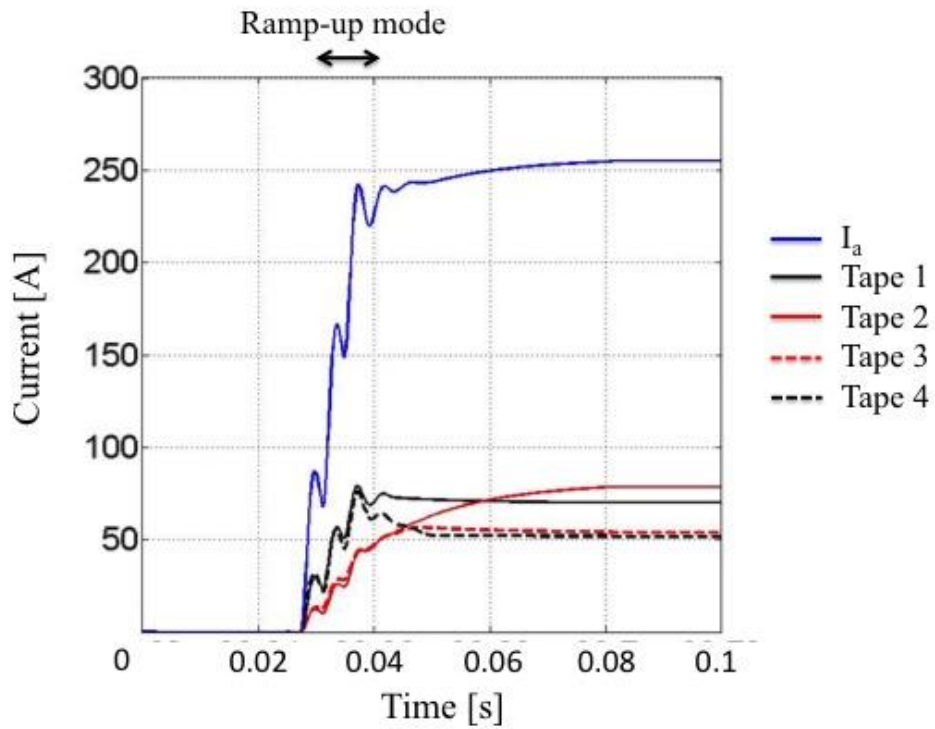


Figure 3.30 Current waveform of four-tape non-insulated twisted stacked cable at 25 A/ms of the ramp rate.

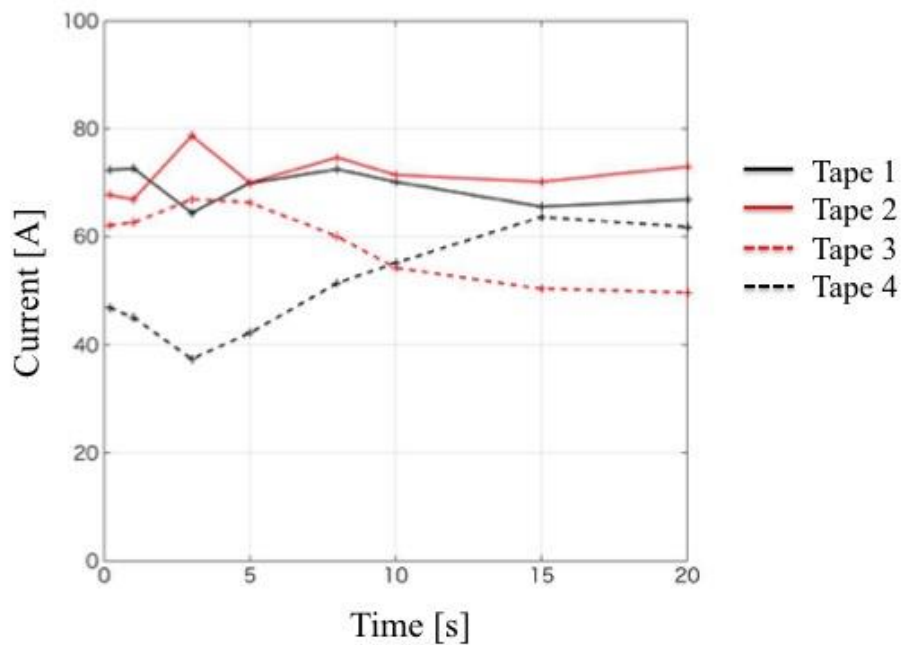


Figure 3.31 Current waveform of four-tape non-insulated twisted stacked cable in long term test. The current in inner tapes 1 and 2 is slightly increasing.

3.3. Conclusions

The partially-insulated twisted stacked cable appears as the best solution for the Twisted Stacked/ Block-type HTS insert, operated under high background fields and with 10 kA-class operating currents. The interests of this concept are to take both the advantages of non-insulated and insulated types. The 46-turn HTS is insulated at straight part of dipole magnet and transposition side of magnet ends to obtain the non-coupled behavior, while it is non-insulated at turn-to-turn transition side to allow the local current exchange. In consequence, the partially-insulated twisted stacked cable obtains homogeneous current distribution, which achieves a good field quality at straight part. It can also make it possible for the current to redistribute in case of localized dissipation in one of the tapes in the stacked cable, improving the overall behavior of the coil with regards to quench. To obtain the best current distribution, the resistivity of adjacent contact between the superconducting layers at the non-insulated part is needed to be smaller than $20 \text{ n}\Omega\cdot\text{m}$ in case of $L_{\text{non}} = 1 \text{ m}$.

Chapter 4

Mechanical challenges of the twisted stacked/ block-type HTS insert

The mechanical design must withstand the thermal stress during cool-down and Lorentz forces during normal operation under background field. The twisted stacked/ block-type HTS insert can be divided into two parts with different mechanical architecture: the straight part and the magnet ends. Owing to the field alignment at the straight part, we adapt the same topology as the general block-type. On the contrary, the twist in the magnet ends has to deal with shear stress, which can cause the delamination of the ReBCO conductor. Therefore, we study with preliminary model based on the 46-turn HTS insert in Chapter 2.

4.1. Baseline for mechanical architecture

4.1.1. Mechanical forces under operation

The superconducting magnets experience two types of mechanical forces during the normal operation: thermal stress and Lorentz forces. The objective of the mechanical structure is to counteract these forces. In addition, it has to minimize the displacement to keep the designed geometric field quality. Figure 4.1 shows the distribution of Lorentz forces with homogeneous current distribution and under 13 T background + self-fields. The inner turns cause more forces due to higher field. All forces are directed outwards where the external mechanical tube is employed. On the contrary, the thermal stress will be directed inwards where the internal mechanical tube is employed.

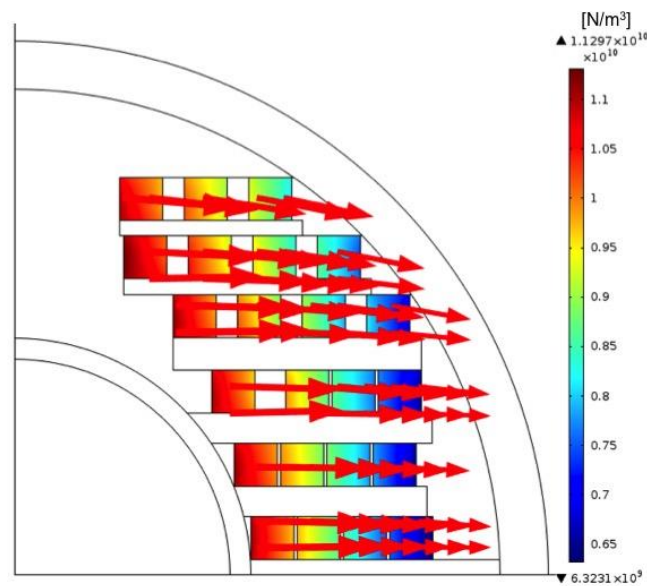


Figure 4.1 Distribution of Lorentz force under background + self-fields in 46-turn HTS insert.

4.1.2. Mechanical reinforcement

Straight part

The main mechanical properties during normal operation are the allowable stress and the thermal expansion coefficient integrated from 4.2 K to 300 K. The allowable stress is defined as equal to two-third of the yield stress, which is the threshold for the plastic deformation. Therefore, it is preferred to use a material possessing high yield stress. But, one has to also pay attention to the thermal expansion coefficient. It has strong influence on the displacement, i.e. the thermal contraction, during cool-down. Moreover, the differences in thermal expansion coefficient induce high thermal stress. Figure 4.2 shows the mechanical design at straight part, which is based on the CERN's mechanical design [89, 90]. It is constituted of:

- Stainless Steel 304: HTS conductor
- Stainless Steel 316: Mechanical tube and plate
- Titanium: Between HTS conductor and internal mechanical tube
- Copper alloy: Between HTS conductor and external mechanical tube

The properties of these materials are listed in Table 4.1 [98]. The entire HTS conductors are represented as a single stainless steel block, although actual conductor is composed of the other materials such as copper and kapton. Therefore, it will influence the results. However, it is still feasible to see the range of the mechanical pressure. The HTS conductors are laid on the flat plate. The 2 mm internal and 4 mm external mechanical tubes are to counteract all thermal stresses and Lorentz forces. We put the 0.2 mm gap between internal tube and beam aperture, and the 0.5 mm gap between external tube and 100 mm aperture LTS outsert. It is to ensure not to overlap HTS insert into LTS outsert region. The titanium has small thermal expansion coefficient. It is expected to exhibit less thermal contraction than the other materials during cool-down. To keep the original position of HTS conductor, the titanium is thus located between the HTS conductor and internal tube. The copper is put between the HTS conductors and the external mechanical tube. This is for both mechanical and electrical reasons. It is also expected to act as the stabilizer during fault-mode condition, which is to protect the magnet.

The mechanical analysis satisfies the boundary conditions and the displacement constrains. The mechanical structure is assumed to assemble tight and stiff. Therefore, all boundaries are glued together. The mechanical architecture is free to move towards the beam aperture and the LTS outsert. On the other hands, the symmetrical design limits the displacement at horizontal and vertical axes.

Table 4.1
Material properties of mechanical reinforcement

| Material | Young Modulus [GPa] | Poisson's ratio | Thermal expansion coefficient (K⁻¹) 4.2 K – 300K |
|---------------------|--------------------------------|------------------------|--|
| Stainless Steel 304 | 210 | 0.279 | 1.02×10^{-5} |
| Stainless Steel 316 | 208 | 0.282 | 1.02×10^{-5} |
| Copper alloy | 138.6 | 0.338 | 1.1211×10^{-5} |
| Titanium | 130.6 | 0.302 | 0.5225×10^{-5} |

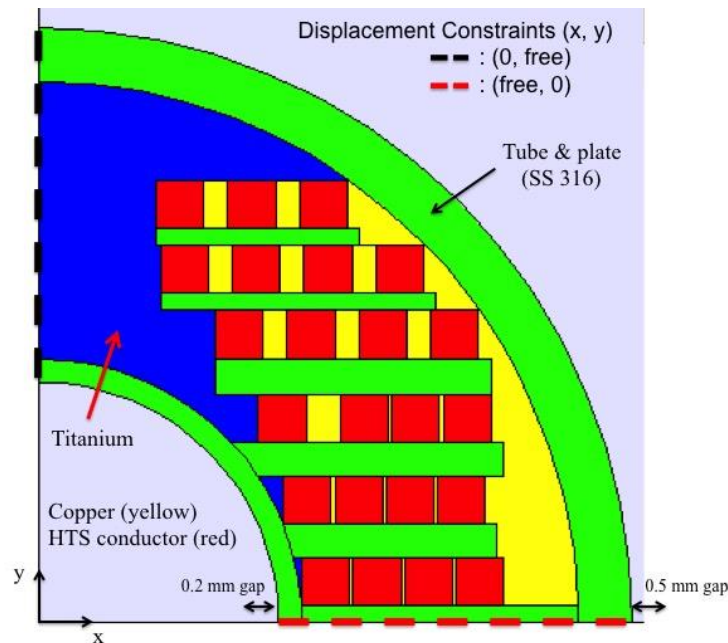


Figure 4.2 Mechanical design of 46-turn HTS insert at straight part.

Magnet ends

In the magnet ends at transposition side, high transverse fields penetrate the ReBCO tape when three top racetrack coils are twisted (see Chapter 2). This means the forces are oriented towards the delamination. The objective is to see the intensity of the shear stress whether it is below than 50 MPa [64, 65]. Figure 4.3 shows one of the 2D cut-planes in magnet ends where the 1st and 3rd racetrack coils are twisted for 45° angles. In principle, it has similar design as that of straight part. The HTS conductor ‘A’ of outermost turn at 1st layer is divided into four tapes. The tape is 4mm wide and 1 mm thick. In our twisted stacked cable, every tape can slide on each other. It means the boundary condition between the tapes becomes a sliding contact. On the other hands, two boundary conditions can be assumed at the perimeter of conductor ‘A’:

- Glued on the copper
- Sliding contact with the copper

The first condition is when the magnet is tightly assembled, which is expected to be in reality. We compare the impact on shear stress of these two conditions.

This mechanical analysis of magnet ends is done in the numerical software ‘Cast3M’ in CEA Saclay.

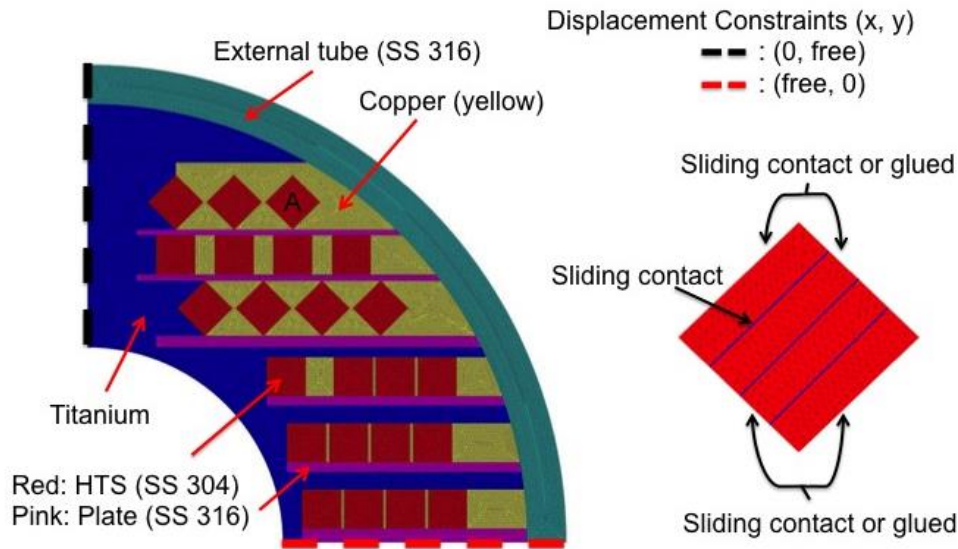


Figure 4.3 Mechanical designs of 46-turn HTS insert in the magnet ends at transposition side whose 1st and 3rd racetrack coils are twisted for 45° angles. HTS conductor 'A' is divided into four tapes.

4.2. Mechanical analysis

The HTS insert undergoes cool-down and powering steps. At first, it is cooled down from 293 K to 4.2 K using the thermal stress analysis. Then, the combined stress due to the thermal contraction and Lorentz forces under 13 T background + self- fields calculated from the electromagnetic analysis is loaded on the model by using the mechanical analysis. In the end, we compare total Von Mises (V.M.) stress with the allowable stress of each material.

4.2.1. Straight part

During the cool-down, the mechanical structure contracts towards center for 0.13mm at the external tube and for 0.08 mm at the internal tube near the vertical axis. This develops the highly-stressed zone in the internal mechanical tube (Figure 4.4). Moreover, there are several high local stresses at sharp edges of the HTS conductor and the plate. It is induced by the differences in a thermal expansion coefficient where the stainless steel contracts more than the titanium. The maximum V.M. stress in HTS conductor is 362 MPa, although most of the parts are below 50 MPa.

The Lorentz forces push the mechanical structure outwards (lower right diagonal). It displaces 0.035 mm in vertical and 0.05 mm in horizontal at maximum (Figure 4.5). Since the internal mechanical tube near the vertical axis is pressed from the top and stretched to right, it results in high stress. The inner turns are also subjected to high stress that is 185 MPa at maximum. It decreases as it goes to outer turns. Most of the HTS conductors experience the forces normal to the flat surface of the ReBCO tape owing to the field alignment. This can be more improved when the entire 46-turn HTS insert is perfectly aligned.

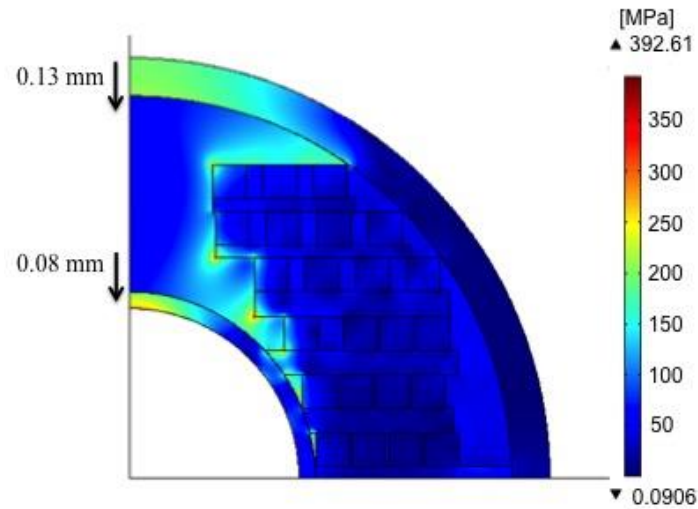


Figure 4.4 Von Mises distributions after cool-down. Maximum V.M. occurs at sharp edges of HTS conductor and plate.

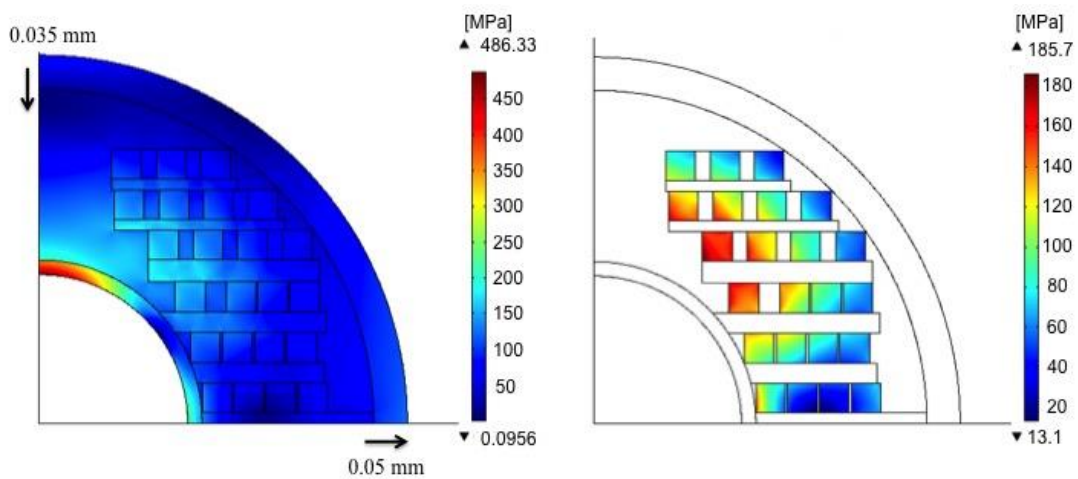


Figure 4.5 Von Mises distributions under only Lorentz forces. Maximum V.M. occurs in internal tube near vertical axis.

In consequence, the total stresses (thermal + Lorentz loads) are compared with the allowable stress listed in Table 4.2. Most of the HTS conductors are subjected to stresses less than 200 MPa (Figure 4.6). However, the sharp edges of innermost turns at 1st – 4th layers cause the stress over 500 MPa. These values are indeed below than the allowable stress of stainless steel 304. However, the critical current of the ReBCO can be degraded for about 10% at 400 – 500 MPa range [64, 65]. Moreover, it is sensitive to the direction of forces. Therefore, the V.M. stress in HTS conductor, which is over 500 MPa, must be reduced. For example, the stress can be relieved by two different ways:

- Smoothing the sharp edges
- Add thin layer between innermost HTS conductor and titanium

The highly-stressed zones are basically caused by thermal stresses. Thus, adding another thin material such as copper, which has similar thermal contraction as HTS conductor, can avoid facing directly between innermost HTS conductor and titanium. The 4 mm thick external tube is able to withstand the forces, while the 2 mm thick internal tube exceeds the limit. We may add extra segment to the internal tube near the vertical axis where the HTS conductor does not exist (dot line in Figure 4.6). The mechanical architecture is displaced inwards, which is kept smaller than 0.2 mm. Hence, the HTS insert does not overlap into either beam tube or LTS outsert.

Table 4.2
Maximum Van Mises Stress during cool down and under normal operation

| Material | Yield/ allowable strength [MPa] | Thermal Load [MPa] | Lorentz load [MPa] | Total [MPa] |
|---------------|---------------------------------|--------------------|--------------------|-------------|
| HTS | 890/ 594 | 360 | 190 | 500 |
| Internal tube | | 280 | 490 | 760 |
| External tube | 980/ 653 | 210 | 120 | 260 |
| Plate | | 390 | 210 | 590 |
| Titanium | 1077/ 718 | 360 | 210 | 490 |
| Copper alloy | 1200/ 800 | 160 | 130 | 200 |

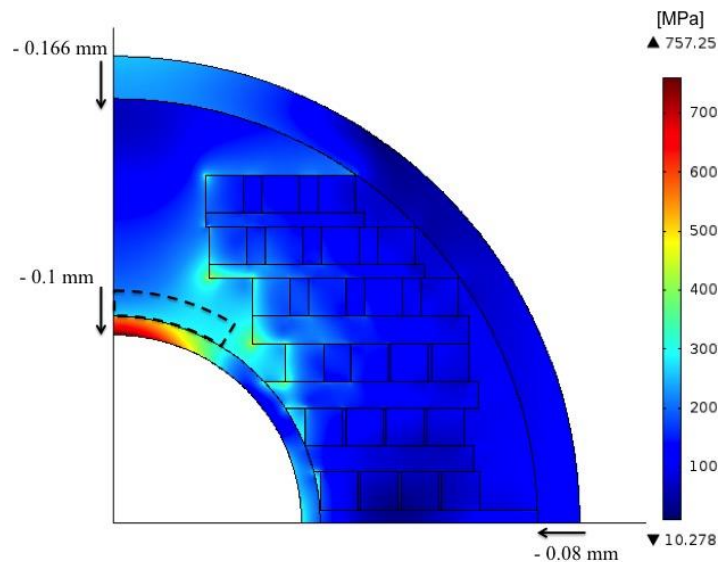


Figure 4.6 Von Mises distributions under combined action. The additional segment can be placed above 2 mm internal mechanical tube.

4.2.2. Magnet ends

Since the magnet ends have similar mechanical architecture and are analyzed under the same operating conditions, it basically shows the same V.M. distribution (Figure 4.7). Moreover, the difference in the boundary condition of HTS conductor ‘A’, which is in sliding contact or glued, has negligible influence on entire design but strong impact near the conductor ‘A’. The highly-stressed zone always occurs at the sharp edges. Besides, the sharp edge appears at corners of 45°-angled conductors. For this reason, the maximum V.M. stress in most materials is higher than the straight part. One can expect to put the thin layer of wax or resin on the 45° twisted part to relieve the stress; even though the stacked cable is twisted along the length. This means that each 2D cut-plane in the magnet ends is different. Figure 4.8 shows the mechanical design at twisted part. The reinforcement has symmetric structure along the length. It has the segment cut-shape where the wax is added after the magnet is assembled. This will facilitate the reinforcement design instead of having the twisted cut-shape all along the length.

Table 4.3
Maximum Van Mises Stress in the magnet ends

| Material | Yield/ allowable strength [MPa] | Thermal Load [MPa] | Lorentz load [MPa] | Total [MPa] |
|---------------|---------------------------------|--------------------|--------------------|-------------|
| HTS | 890/ 594 | 340 | 300 | 510 |
| External tube | 980/ 653 | 310 | 170 | 430 |
| Plate | | 440 | 380 | 700 |
| Titanium | 1077/ 718 | 330 | 430 | 460 |
| Copper | 1200/ 800 | 290 | 350 | 590 |

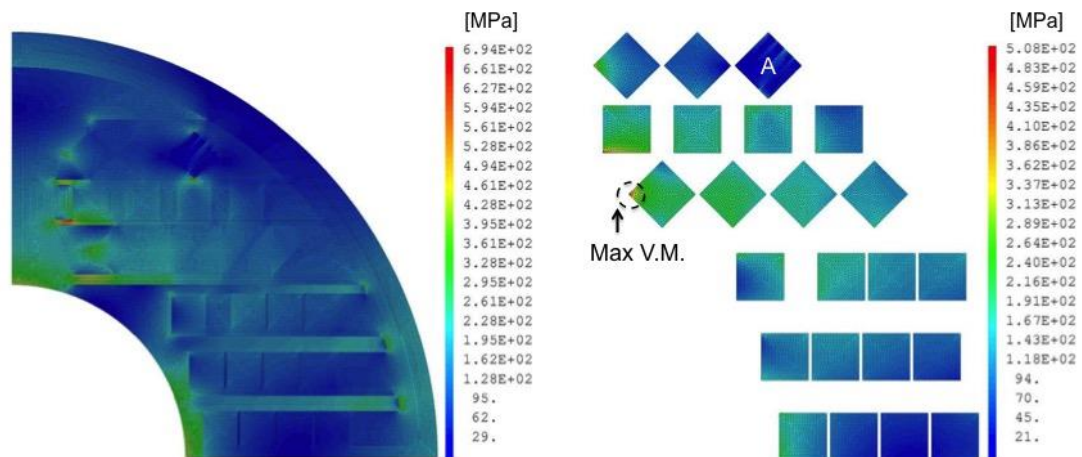


Figure 4.7 Von Mises distribution in magnet ends under combined action. Maximum V.M. stress in HTS conductor occurs at sharp edges of innermost turn at 3rd layer.

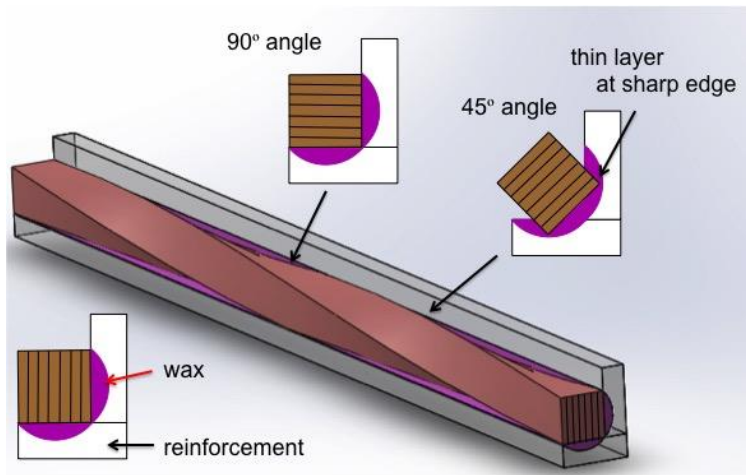


Figure 4.8 Mechanical designs at twisted part of stacked cable. The reinforcement has symmetric segment cut-shape along the length.

The shear force becomes bigger when the frictional coefficient gets closer to 1. Therefore, the boundary condition at the perimeter of conductor 'A' being glued on copper subjects to more shear stress than in sliding contact (Figure 4.9). Most of parts are 15 – 50 MPa range in glued condition. The local shear stress occurs at the corner of 1 mm thick tape. In particular, the lower part of conductor 'A' suffers from the thermal and Lorentz loads, which brings highly stressed zone about 80 MPa range. The maximum shear stress is 188 MPa in glued condition while it is only 49 MPa in sliding contact.

In reality, the boundary condition is similar to the glued condition. It results in high shear stress over 50 MPa. This can easily cause the delamination of ReBCO tape. Thus, even from a mechanical point of view, it is necessary to locate the magnet ends of insert outside of the straight part of outsert.

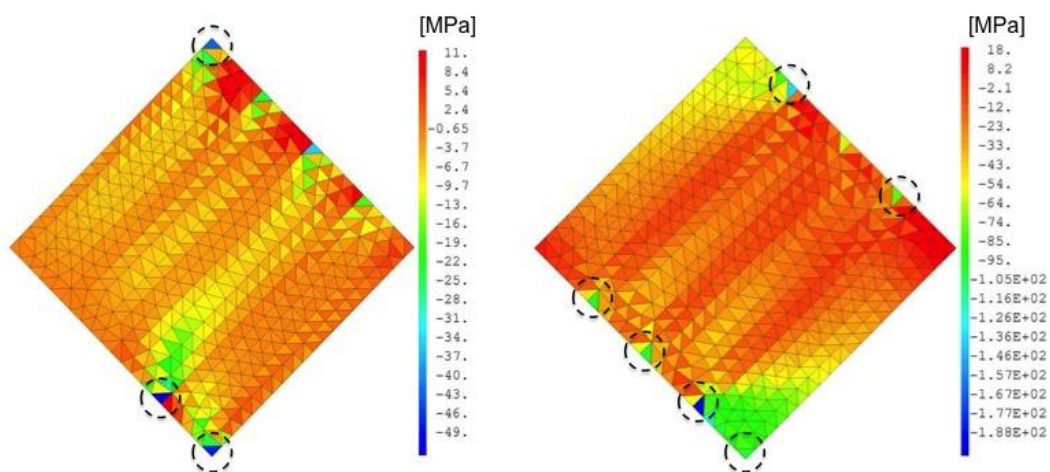


Figure 4.9 Shear stress distributions in conductor 'A' in case its perimeter is in sliding contact (left) and glued on copper (right).

4.3. Conclusions

The mechanical structures at straight part and in the magnet ends are analyzed under thermal and Lorentz loads. It assumes that the magnet is assembled tight and stiff. At the straight part, most of the reinforcements are kept below their allowable strength except the internal mechanical tube. Therefore, it is still needed to add extra segment on top of the weak zone. The sharp edges in the HTS conductor create extremely high local stress, while the other parts are below 200 MPa. We propose to interpose the thin plate such as copper, whose thermal contraction is similar to HTS conductor. This may relieve the highly-stressed zone caused by thermal loads.

One of the 2D cut-planes in the magnet ends, whose cables at 1st and 3rd layers are twisted for 45°, is studied under 13 T background + self- fields. The shear stress turns out to be crucial problem where the cable is twisted. The HTS conductor 'A' of outermost turn at 1st layer, which is divided into four tapes, shows the shear stress over 50 MPa. This is enough to cause the delamination of the ReBCO tape. For this reason, the magnet ends of HTS insert is preferred to locate outside of the magnet ends of LTS outsert, which basically reduce the magnetic field more than 50%.

Conclusions

A first attempt at designing of high temperature superconducting (HTS) dipole insert using a twisted stacked cable for a particle accelerator is presented in this work. It is called 'Twisted Stacked/ Block-type HTS insert'. In the framework of EuCARD2 project, the objective is to achieve a 5 T HTS insert operated inside a low temperature superconducting (LTS) dipole outsert. It requires a 10 kA-class HTS transposed cable to provide a good field quality inside a 40 mm beam tube. We thus use a ReBCO twisted stacked cable proposed by M. Takayasu in MIT. The twisted stacked cable has a simple structure and is partially transposed. This will enable to increase the flux density over 15 T.

A dedicated homemade 2D analytic code has optimized the electromagnetic behavior of HTS insert at straight part cross-section considering the twist of the stacked cable in magnet ends. It also considers the mechanical architecture at first design stage. This brings a 46-turn HTS insert using a 4x4 mm block carrying a 10.4 kA of operating current. In addition, the field quality requirements are filled and a 650MA/m² of operating current density is rather low, which is also lower compared to other alternative designs. The 46-turn HTS insert is composed of twelve pancake coils, which gives six double pancake coils in total. All blocks are almost aligned to the background magnetic field in order to make best use of the engineering current density J_e . This also helps to direct the Lorentz forces onto the wide face of the ReBCO tapes.

The magnet ends of twisted stacked/ block-type HTS insert are different between both sides: transposition and turn-to-turn transition side. A twist is only applied at transposition side in order to achieve the transposed magnet: whereas there is layer jump, inlet and outlet at turn-to-turn transition side. Twelve pancake coils are wound either racetrack flat or flared-end coil with one twist per turn in 15 m long, which results in a very long transposition pitch. Besides, some magnet ends of HTS insert is located outside of the magnet ends of LTS outsert in order to keep high J_e .

Extensive numerical simulation and calculation has been implemented in FLUX software. It is to study the electromagnetic behavior of the HTS twisted stacked cable with a very long transposition pitch. The objective is to fulfill the cable's requirements: low magnetization (non-coupled behavior) and homogeneous current distribution. However, both non-insulated and insulated twisted stacked cables are not able to meet these expectations due to a very long twist transposition pitch. Therefore, we have proposed the partially insulated twisted stacked cable. This innovative concept takes both advantages of non-insulated and insulated cables. It is possible to have the non-coupled behavior at straight part of dipole magnet and the local current exchange at non-insulated turn-to-turn transition side in magnet. In the end, this gives uniform current distribution in the cable and achieve required field quality.

Long term experiment of a half U-turn coil using the non-insulated twisted stacked with a 20 m long transposition pitch at 77 K in self-field validated the numerical simulation in FLUX. Now, we need to test the partially-insulated solution in form of a half U-turn coil to validate its behavior in terms of magnetization and current distribution.

Winding of the twisted stacked/ block-type HTS insert is required to build a dedicated winding machine, which has to twist the stacked cable in magnet ends. In addition, the partially insulated solution makes more complicate. For example, non-insulating the stacked cable only at turn-to-turn transition side in magnet ends. Therefore, one can put the additional resistive layer between the ReBCO tapes at back-to-back (B^2) configuration (Figure I). The resistivity of additional resistive layer must be high enough to have the non-coupled behavior at straight part of dipole magnet. This will dramatically facilitate the winding of partially insulated cable.

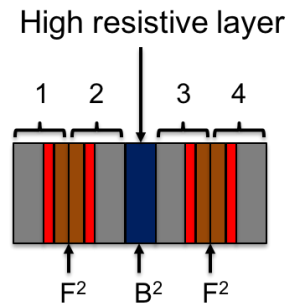


Figure I Cross-section of four-tape stacked cable with high resistive layer at back-to-back (B^2) configuration.

Bibliography

- [1] CERN Accelerating science ‘<http://home.cern/>’
- [2] G. Aad et al, 2012, Observation of a new particle in the search for the Standard Model Higgs boson with the ATLAS detector at the LHC, Physics Letters B Vol. 716 No.1
- [3] O. Bruning et al, 2004, LHC Design Report Volume 1: The LHC Main Ring, CERN Document Server
- [4] P. Lefèvre and T. Petterson, THE LARGE HADRON COLLIDER, CERN Desktop Publishing Service, October 1995
- [5] L. Evans and P. Bryant, 2008, LHC Machine, Supercond. Sci. Technol. Vol. 3
- [6] L. Rossi and L. Bottura, 2012, Superconducting Magnets for Particle Accelerators, Reviews of Accelerator Science and Technology
- [7] L. Rossi, 2003, The LHC main Dipoles and Quadrupoles Toward Series Production, IEEE Trans. Appl. Supercond. Vol. 13, No. 2, 1221
- [8] J. Ahlback et al, 1996, Construction of a 56 mm aperture high-field twin-aperture superconducting dipole magnet, IEEE Trans. Magn. Vol. 32, No. 4, 2097
- [9] Martin N. Wilson, 1983, Superconducting Magnets, Clarendon Press
- [10] Y. Iwasa, 2009, Case Studies in Superconducting Magnets: Design and Operational Issues, 2nd ed. Springer
- [11] C. P. Bean, 1962, Magnetization of Hard Superconductors, Phys. Rev. Lett. Vol. 8 250
- [12] M. A. R. LeBlanc, 1963, Influence of transport current on the magnetization of a hard superconductor, Phys. Rev. Lett. Vol. 11 149
- [13] L. Bottura, 2013, Magnet Quench 101, WAMSDO 2013
- [14] E. Todesco, 2013, Quench in the next generation of magnets, WAMSDO 2013
- [15] T. Ariyama et al, 2016, Quench Protection of YBCO Coils: Co-Winding Detection Method and Limits to Hot-Spot Temperature, IEEE Trans. Appl. Supercond. Vol. 26, No. 3, 4702205
- [16] Y. Iwasa, 2005, Stability and Protection of Superconducting Magnets: A Discussion, IEEE Trans. Appl. Supercond. Vol. 15, No. 2, 1615

- [17] P. Seidel, 2015, Applied Superconductivity: Handbook on Devices and Applications, Wiley-VCH
- [18] National High Magnetic Field Laboratory '<https://nationalmaglab.org>'
- [19] A. Devred et al, 2005, Future Accelerator Magnet Needs, IEEE Trans. Appl. Supercond. Vol. 15, No. 2, 1192
- [20] L. Bottura et al, 2012, Advanced Accelerator Magnets for Upgrading the LHC, IEEE Trans. Appl. Supercond. Vol. 22, No. 3, 4002008
- [21] E. Todesco et al, 2014, Dipoles for High-Energy LHC, IEEE Trans. Appl. Supercond. Vol. 24, No. 3, 4004306
- [22] Martin N. Wilson, 1996, Superconducting materials for magnets, CERN Accelerator School on Superconductivity in Particle Accelerator
- [23] E. Gregory, 1989, Conventional wire and cable technology, IEEE Trans. Appl. Supercond. Vol. 77, No. 8, 1110
- [24] D. Leroy, 2006, Reviews of the R&D and supply of the LHC Superconducting Cables, IEEE Trans. Appl. Supercond. Vol. 16, No. 2, 1152
- [25] C. Spencer et al, 2003, The temperature and magnetic field dependence of superconducting critical current densities of multifilamentary Nb₃Sn and NbTi composite wires, IEEE Trans. Magn. Vol. 15, No. 1, 76
- [26] H. Boschman et al, 2002, The influence of transverse, compressive stress on the critical current of multifilamentary Nb₃Sn and NbTi wires, IEEE Trans. Magn. Vol. 25, No. 2, 1976
- [27] E. Barzi et al, 2004, Development and study Rutherford-type cables for high-field accelerator magnets at Fermilab, Supercond. Sci. Technol. Vol.17 No. 9
- [28] K. Saito and K. Zaitsev, 2016, Nb₃Sn wire Technology for High-field Superconducting Magnet, Kobelco Tech. Review No.34, 72
- [29] E. Buehler and H. J. Levinstein, 1965, Effect of tensile stress on the transition temperature and current-carrying capacity of Nb₃Sn, J. Appl. Phys. Vol. 36, No.12, 3856
- [30] J. W. Ekin, 1984, Strain effects in superconducting compounds, Adv. Cryog. Eng. Materials Vol. 30, 823
- [31] Xu Wang and Yuanwen Gao, 2016, Tensile Behavior Analysis of the Nb₃Sn Superconducting Strand With Damage of the Filaments, IEEE Trans. Appl. Supercond. Vol. 26, No. 4, 6000304

- [32] A. R. Hafalia et al, 2005, HD1: Design and Fabrication of a 16 Tesla Nb₃Sn Dipole Magnet, Physical Review Vol. 91 No. 9
- [33] S. Caspi et al, 2007, Design, Fabrication, and Test of a Superconducting Dipole Magnet Based on Tilted Solenoids, IEEE Trans. Appl. Supercond. Vol. 17, No. 2, 2266
- [34] M. Karppinen et al, 2012, Design for 11 T Twin-Aperture Nb₃Sn Dipole Demonstrator Magnet for LHC Upgrades, IEEE Trans. Appl. Supercond. Vol. 22, No. 3, 4901504
- [35] J. C. Perez et al, 2015, Performance of the Short Model Coils Wound With the CERN 11-T Nb₃Sn Conductor, IEEE Trans. Appl. Supercond. Vol. 25, No. 3, 4002805
- [36] EuCARD project: '<http://eucard-old.web.cern.ch>'
- [37] P. Fazilleau, 2013, Protection of the 13 T Nb₃Sn Fresca II dipole, WAMSDO 2013
- [38] P. Ferracin et al, 2013, Development of the EuCARD Nb₃Sn Dipole Magnet FRESCA2, IEEE Trans. Appl. Supercond. Vol. 23, No. 3, 4002005
- [39] E. Ravaioli et al, 2016, Advanced Quench Protection for the Nb₃Sn Quadrupoles for the High Luminosity LHC, IEEE Trans. Appl. Supercond. Vol. 26, No. 3, 4002006
- [40] T. Salmi et al, 2013, Modeling heat transfer from quench protection heaters to superconducting cables in Nb₃Sn magnets, WAMSDO 2013
- [41] G. Ambrosio et al, Maximum allowable temperature during quench in Nb₃Sn accelerator magnets, WAMSDO 2013
- [42] J. R. Hull, 2003, Applications of high-temperature superconductors in power technology, Rep. Prog. Phys. Vol. 66 1865
- [43] K. R. Marken et al, 2003, BSCCO-2212 conductor development at Oxford Superconducting Technology, IEEE Trans. Appl. Supercond. Vol. 13, No. 2, 3335
- [44] SUMITOMO ELECTRIC. Di-BSCCO 'http://global-sei.com/super/hts_e/'
- [45] SuperPower '<http://www.superpower-inc.com/>'
- [46] AMSC, '<http://www.amsc.com/>'
- [47] Bruker, '<http://www.bruker-est.com/>'
- [48] SuperOX, '<http://www.superox.ru>'

- [49] E. Haro et al, 2013, Quench Considerations and Protection Scheme of a High Field HTS Dipole Insert Coil, *IEEE Trans. Appl. Supercond.* Vol. 23, No. 3, 4600104
- [50] V. E. Keilin and D. I. Shutova, 2013, Model of Quench Development Inside HTS Coils Including Quench-to-Critical Current Ratio Evaluation, , *IEEE Trans. Appl. Supercond.* Vol. 23, No. 3, 4701904
- [51] E. Barzi et al, 2011, BSCCO-2212 Wire and Cable Studies, *IEEE Trans. Appl. Supercond.* Vol. 21, No. 3, 2235
- [52] Y. Aoki et al, 2000, Development of a large current capacity conductor using Bi-system superconductors, *Physica C* 355
- [53] P. Tixador et al, 2015, Mechanically reinforced Bi-2212 strand, *IEEE Trans. Appl. Supercond.* Vol. 25, No. 3, 6400404
- [54] B. Ten Herman and H. J. Ten Kate, 1995, Compressive and Tensile Axial Strain reduced Critical Currents in Bi-2212 Conductors, *IEEE Trans. Appl. Supercond.* Vol. 5, No. 2, 1298
- [55] A. Malagoli et al, 2011, Evidence for long range movement of Bi-2212 within the filament bundle on melting and its significant effect on J_c , *Supercond. Sci. Technol.* Vol. 24 075016
- [56] D. I. Meyer and R. Flasck, 1970, A New Configuration for a Dipole Magnet for use in High Energy Physics Applications, *Nuclear Instrum. Methods*, No. 80, 339
- [57] L. Brouwer et al, 2014, Structural Design and Analysis of Canted-Cosine-Theta Dipoles, *IEEE Trans. Appl. Supercond.* Vol. 24, No. 3, 4001506
- [58] A. Godeke et al, 2015, Bi-2212 Canted-Cosine-Theta Coils for High-Field Accelerator Magnets, *IEEE Trans. Appl. Supercond.* Vol. 25, No. 3, 4002404
- [59] C. H. Rosner et al, 1992, Status of HTS superconductors: Progress in improving transport critical current densities in HTS Bi-2223 tapes and coils, *Cryogenics* Vol. 32, No.11, 940
- [60] K. Osamura et al, 2008, Mechanical behavior and strain dependence of the critical current of DI-BSCCO tapes, *Supercond. Sci. Technol.* Vol.21
- [61] S. Mukoyama et al, 2007, Experimental Results of a 500 m HTS Power Cable Field Test, *IEEE Trans. Appl. Supercond.* Vol. 17, No. 2, 1680
- [62] THEVA, '<http://theva.com/>'

- [63] T. Benkel et al, 2016, REBCO Performance at High Field With Low Incident Angle and Preliminary Tests for a 10-T Insert, *IEEE Trans. Appl. Supercond.* Vol. 26, No. 3, 4302705
- [64] M. Sugano et al, 2005, Tensile fracture behavior of RE-123 coated conductors induced by discontinuous yielding in Hastelloy C-276 substrate, *Supercond. Sci. Technol.* Vol. 18
- [65] C. Pes et al, 2014, Three-Dimensional Magnetic and Mechanical Finite-Element Analysis of the HTS Insert Coil, *IEEE Trans. Appl. Supercond.* Vol. 24, No. 3, 4001105
- [66] J. M. Rey et al, 2013, HTS Dipole Insert Developments, *IEEE Trans. Appl. Supercond.* Vol. 23, No. 3, 4601004
- [67] Christian Barth, 2013, High Temperature Superconductor Cable Concepts for Fusion Magnets, KIT Scientific Publishing
- [68] W. H. Fietz et al, 2016, High-Current HTS Cables: Status and Actual Development, *IEEE Trans. Appl. Supercond.* Vol. 26, No. 4, 4800705
- [69] W. Goldacker et al, 2014, Roebel cables from REBCO coated conductors: a one-century-old concept for the superconductivity of the future, *Supercond. Sci. Technol.* Vol. 27 093001
- [70] S. Terzieva et al, 2010, Transport and magnetization ac losses of ROEBEL assembled coated conductor cables: measurement and calculations, *Supercond. Sci. Technol.* Vol. 23 014023
- [71] M. Vojenciak et al, 2011, Effect of self-field on the current distribution in Roebel-assembled coated conductor cable, *Supercond. Sci. Technol.* Vol. 24 095002
- [72] J. Fleiter et al, 2013, Electrical characterization of REBCO Roebel cables, *Supercond. Sci. Technol.* Vol. 26, 065014
- [73] R. A. Badcock et al, 2009, Progress in the Manufacturing of Long Length YBCO Roebel Cables, *IEEE Trans. Appl. Supercond.* Vol. 19, No. 3, 3244
- [74] T. Tsukamoto et al, 2015, Influence of Geometrical Configurations of HTS Roebel Cables on Their AC Losses, *IEEE Trans. Appl. Supercond.* Vol. 25 4802005
- [75] C. Barth et al, 2012, Electro-mechanical analysis of Roebel cables with different geometries, *Supercond. Sci. Technol.* Vol. 25 025007

- [76] C. W. Bumby et al, 2013, Critical Current Behavior of HTS Roebel Cable under Tensile Stress, *IEEE Trans. Appl. Supercond.* Vol. 23 No. 3 4801805
- [77] Advanced Conductor Technologies LLC '<http://advancedconductor.com/>'
- [78] T. Mulder et al, 2016, Performance Test of an 8 kA at 10-T 4.2-K ReBCO-CORC Cable, *IEEE Trans. Appl. Supercond.* Vol. 26, No. 4, 4803705
- [79] T. Mulder et al, 2016, Design and Manufacturing of a 45 kA at 10 T REBCO-CORC Cable-in-Conduit Conductor for Large-Scale Magnets, *IEEE Trans. Appl. Supercond.* Vol. 26, No. 4, 4803605
- [80] M. J. Wolf et al, 2016, HTS CroCo: A stacked HTS Conductor Optimized for High Currents and Long-Length Production, *IEEE Trans. Appl. Supercond.* Vol. 26, No. 2, 6400106
- [81] M. Takayasu et al, 2011, Cabling Method for High Current Conductors Made of HTS Tapes, *IEEE Trans. Appl. Supercond.* Vol. 21, No. 3, 2340
- [82] M. Takayasu et al, 2012, HTS twisted stacked-tape cable conductor, *Supercond. Sci. Technol.* Vol. 25, 014011
- [83] M. Takayasu, 2013, Conductor Characterization of YBCO Twisted Stacked-tape Cable, *IEEE Trans. Appl. Supercond.* Vol. 23, No. 3, 4800104
- [84] N. Bykovsky, 2016, Design Optimization of Round Strands Made by Twisted Stacks of HTS Tapes, *IEEE Trans. Appl. Supercond.* Vol. 26, No. 2, 4201207
- [85] M. Takayasu et al, 2016, Electrical and Mechanical Characteristics of HTS Twisted Stacked-Tape Cable (TSTC) Conductor, ASC2016 Conference in Denver, U.S. 2LPo2D-3
- [86] N. Bykovsky et al, 2015, Strain Management in HTS Current Cables, *IEEE Trans. Appl. Supercond.* Vol. 25, No. 3, 4800304
- [87] M. Takayasu et al, 2010, Torsion Strain Effects on Critical Currents of HTS Superconducting Tapes, *Advances in Cryogenics Engineering* Vol. 56, 337
- [88] L. Rossi et al, 2015, The EuCARD-2 Future Magnets European Collaboration for Accelerator-Quality HTS Magnets, *IEEE Trans. Appl. Supercond.* Vol. 25, No. 3, 4001007
- [89] J. V. Nugteren et al, 2015, Study of a 5T Research Dipole Inert-Magnet Using an Anisotropic ReBCO Roebel Cable, *IEEE Trans. Appl. Supercond.* Vol. 25, No. 3, 4000705

- [90] G. Kirby et al, 2016, Status of the Demonstrator Magnets for the EuCARD-2 Future Magnets Project, IEEE Trans. Appl. Supercond. Vol. 26, No. 3, 4003307
- [91] C. Lorin et al, 2015, Cos- θ Design of Dipole Inserts Made of REBCO-Roebel or BSCCO-Rutherford Cables, IEEE Trans. Appl. Supercond. Vol. 25, No. 3, 4000305
- [92] C. Lorin et al, 2016, Development of a Roebel-Cable-Based $\cos\theta$ Dipole: Design and Windability of Magnet ends, IEEE Trans. Appl. Supercond. Vol. 26, No. 3, 4003105
- [93] E. Rochepault et al, 2012, 2D Analytical Magnetic Optimizations for Accelerator Dipole Block designs, IEEE Trans. Appl. Supercond. Vol. 22, No. 3, 4900804
- [94] FLUX[®], '<http://www.cedrat.com/>'
- [95] P. Tixador, 1995, Les supraconducteur, Hermes
- [96] P. Seidel, 2015, Applied Superconductivity: Handbook on Devices and Applications, Wiley
- [97] R. G. Sharma, 2015, Superconductivity: Basics and Applications to Magnets, Springer Series in Materials Science
- [98] R. P. Reed and A. F. Clark, 1983, Materials at low temperatures, Asm Intl